Progress Towards a Redetermination of the Neutron Lifetime Through the Absolute Determination of Neutron Flux

A Dissertation

Presented for the

Doctor of Philosophy

Degree

The University of Tennessee, Knoxville

Andrew T. Yue

December 2011

© by Andrew T. Yue, 2011
All Rights Reserved.

For Janet and Cheung,

Helen and Robert,

Yung and Siang.

Acknowledgements

For as long as I have been writing this dissertation, I have been thinking about what I would write here. Yet here I am, beginning it in the closing hours of this work. I think it is because, more than anything, I wanted to make sure that my acknowledgement of the innumerable contributions of others was as well thought out as possible. Even with this preparation, it is inevitable that I will leave someone deserving out, and for that I apologize.

I have led a charmed existence as a graduate student. This project has been an absolute joy to work on, and I am very proud of our accomplishments. I attribute my success to having received more than my fair share of good fortune and to the limitless patience I have been afforded by others. Patience is truly the most valuable currency a student in my position could ask for. Thus it is no surprise that I first acknowledge the contributions of my advisor Geoff Greene. He has had to correct countless silly mistakes and poor decisions that I have made, yet his guidance was always measured, educational, and mindful of my sometimes fragile ego. His approachability and accessibility have made this an easy and productive relationship. He has seen and participated in nearly everything this field has produced and has willingly shared the most valuable lessons learned. I am greatly encouraged by his continued enjoyment in the minutiae of the work. His is a very contageous mentality. I am proud to call him a colleague and a friend.

I think it is only fair to (unofficially) appoint Scott Dewey as my co-advisor. His fingerprints are on every part of this work. Every important decision that I made

came only after seeking his valuable input first. He, more than anyone, was subject to my daily pestering for advice and never failed to deliver a good answer. I thank him for what can only be described as superlative patience. I am also grateful for our entertaining conversations outside of physics, namely discussions on technological diversions and where to get a great meal in the DC area. I am excited to continue working with him in the next phase of my career.

I am grateful for the considerable efforts of my collaborators. Jeff Nico provided important guidance at every step of the project. His ability to find humor in our darkest hours preserved my sanity on a number of occasions. I am encouraged by his continued enthusiasm for science despite the presence of so many unnecessary obstacles. His workmanlike approach is undoubtedly appreciated by his colleagues, and is worth mentioning here as well. I am especially grateful for the considerable time he spent proofreading this dissertation. David Gilliam was precisely the right person for me to work with at the beginning of this project. It was immediately apparent to me that I should strive to emulate his temperament and attention to detail. They are are absolutely vital for work in this field. Sasha Laptev was instrumental in getting this project out of storage and onto the guide hall floor. No task was too small for his attention. Much like Scott, he was steadfast, reassuring, and patient when subjected to my mercurial tendencies. I wish him the best of luck in his future endeavors and hope that our paths cross again soon.

My experience with the entirety of the Neutron Interactions and Dosimetry group (and the NIST Center for Neutron Research as a whole) has been overwhelmingly positive. Muhammad Arif must be thanked for his advice on the wavelength measurement and especially for his patience. I have no doubt that he is largely responsible for the insulated environment I was afforded. I also thank Mike Huber and David Jacobson for their help with the wavelength measurement. I thank Pieter Mumm and Alan Thompson for valuable advice that I feel has set my scientific career off on the right path. Our conversations, scientific or otherwise, have always been entertaining and useful. The inevitable spicy condiment brinkmanship that

accompanies Alan always makes for entertaining, if not good meals. The past and present postdocs and graduate students in the NI&D group (Robert Cooper, Mike Huber, Brian Fisher, Dima Pushin, Chris O'Shaughnessy, Karl Schelhammer, Craig Huffer, Patrick Hughes, George Noid, and Guillaume Darius) and friends from elsewhere in the building (Richard Bindel, Danny Phelan, Shannon Watson, and Russell Watson) made the NCNR an exciting and entertaining place to be. I am deeply grateful for their camaraderie. I thank Rob Shankle, Eli Baltic, and Doug Johnson for their work on machining the many (and sometimes superfluous) parts that I requested. I thank Jamie Reardon and Sean Mullendore for saving our filter cryostat vacuum (and thus, weeks of data) on at least two occasions. I thank Jeff Lynn and Sung Chang for performing the thick target neutron scattering measurement with the SPINS apparatus. I also thank Fred Wietfeldt and Mike Snow for useful and thought-provoking discussions about Alpha-Gamma, the neutron radiometer, and the lifetime experiment.

My time at the University of Tennessee has been enjoyable. This is in no small part due to the very competent and always pleasant staff in the department office. I especially thank Joyce Satterfield and Judy Hutchins for their assistance all these years - I would have been lost without them. I thank Rob and Ellen Mahurin for their friendship when I needed it most. Rob deserves additional thanks for his willingness to mentor and his contageous enthusiasm for critical thinking, be it physics or otherwise. Thanks go to Nadia Fomin for her friendship and for being the ringleader for us FNP group underlings. I recall fun (and sometimes educational) times with my friends from the entering class of 2004 - Shaun Ard, Johnny Dadras, Adam Krause, Brian Moazen, Dan Parshall, Elizabeth Shroyer, Scott Thornton, Nick Vence, Tony Wald, Zac Ward, Josh Whitney, and Brad Wogsland.

My feelings for Hamilton College are mixed, but I have always thought the world of the physics department and my fellow physics majors. I especially thank Frank Pickard, Dan Allen, Stephanie Bealing (née Higgins), Kosta Popović, Freddie Dias, and Bea Dias for their camaraderie. The department's commitment to undergraduate

research is, without a doubt, the reason that I have purused a career in physics. I thank David Craig and Ann Silversmith for the advisory role they played. I thank Gordon Jones for sending me off on this crazy path by asking if I would like to spend a summer at Los Alamos.

Speaking of Los Alamos, I thank Gil Peralta, Seppo Penttila, Scott Wilburn, David Bowman, and Greg Mitchell for the enjoyable and educational work environment I had that summer. It was there that I developed a real taste for this line of work. Thanks also go to Richard Mah and Gil Peralta for their friendship, especially the countless hours we spent ~~golfing~~ working. Los Alamos (and all of New Mexico) will always feel like home to me.

I have been fortunate that my oldest friends still remain my closest. The support of John Bartholomew, Jeremy Fondran, Josiah Miller, Brenna Finn, Derek Mong, Joe Prerost, and John Blayne has been so important in the twenty years I have known them.

I cannot thank family enough for their support. I am deeply grateful for the sacrifices my grandparents and parents have made to allow me to be where I am today. My mother, my father, and my brother Alex have never questioned my (admittedly crazy) desire to work in physics. Finally, I especially thank Jacqueline Walsh, who has put up with me for nearly three years and continues to show me what is important in life.

Do I dare

Disturb the universe?

In a minute there is time

For decisions and revisions which a minute will reverse.

-T. S. Eliot

Abstract

The reported lifetime in an in-beam neutron lifetime experiment performed at NIST was $\tau_n = (886.3 \pm 3.4)$ s [Nico et al., 2005b]. The largest source of uncertainty was the efficiency of the neutron flux monitor (0.3 % relative uncertainty). The flux monitor operates by counting charged particles produced when neutrons impinge on a ^{6}Li foil. Its efficiency was calculated from the ^{6}Li thermal neutron cross section, the solid angle subtended by the charged particle detectors, and the amount of neutron-absorbing material present on the foil. An absolute black neutron detector for cold neutron beams has been developed to measure the efficiency without the need to know these quantities. The flux monitor efficiency is measured to a precision of 0.052 % using this direct calibration technique. This calibration removes the largest barrier to a 1 s neutron lifetime measurement with the beam technique. It is hoped that this data can also be used to re-evaluate the current NIST neutron lifetime value, reduce its uncertainty, and remove the dependence on evaluated nuclear data files. There is also the possibility for a direct measurement of the ^{6}Li thermal neutron cross section.

Contents

List of Tables **xiii**

List of Figures **xv**

1 Theory of Neutron Beta Decay **1**

1.1 Discovery of the Neutron 1

1.2 Neutron β^--Decay in the Standard Model 2

1.3 Neutron β^--Decay and Big Bang Nucleosynthesis 4

1.4 Neutron Lifetime Measurements 5

2 The NIST In-Beam Neutron Lifetime Measurement **15**

2.1 Measuring Neutron Decays 16

2.2 Measuring Neutron Flux 17

2.3 Determining the Neutron Lifetime 19

2.4 Assessment of Uncertainties 25

3 Direct Measurement of the Flux Monitor Efficiency **27**

3.1 The Neutron Calorimeter 28

3.1.1 First Run of the Neutron Calorimeter 30

3.1.2 Second Run of the Neutron Calorimeter 31

3.1.3 Third Run of the Neutron Calorimeter 32

3.2 The Alpha-Gamma Technique 32

3.2.1 Alpha-Gamma Prototype 38

3.2.2 First Run of the Alpha-Gamma Device 38
3.2.3 Second Run of the Alpha-Gamma 39

4 Characterizing the Beamline **41**
4.1 The NIST Center for Neutron Research 41
4.2 NG6m 45
4.3 Aligning and Imaging the Beam 47
4.4 Measuring the Beam Wavelength 57

5 The Alpha-Gamma Device **74**
5.1 Device Construction 74
5.2 Device Electronics 81
5.3 Plutonium Source Calibration 90
5.4 Internal Calibration of the Alpha-Gamma Device 92
5.5 Calibration of the Neutron Flux Monitor 95
5.6 Accounting for Gamma Rate Drifts 95

6 Assessment of Systematic Effects **98**
6.1 Corrections to the Plutonium Source 98
6.2 Corrections to Thin Target Data 101
6.3 Corrections to Thick Target Data 104
6.4 Corrections to the Flux Monitor Data 109

7 Results **119**
7.1 Neutron Flux Monitor Efficiency Result 119

8 Conclusion **126**
8.1 The Future of the Alpha-Gamma Device 126
8.2 Prospects for Re-evaluating the Neutron Lifetime and ^{6}Li Cross Section 128

Bibliography **133**

A Summary of Neutron Lifetime Measurements **145**

B Statistical Combination of Source Activity Measurements **147**

B.1 Determining Source Activity for Each Stack 147

B.2 Combining $R_{38}^{4\pi}$ and $R_{76}^{4\pi}$ 149

Vita **152**

List of Tables

2.1 Westcott g-factors for ^{6}Li and ^{10}B at $T = 20.44$ °C [Chowdhuri, 2000; Lamaze et al., 1988]. 19

2.2 The beam lifetime experiment uncertainty budget [Nico et al., 2005b]. Items 1-3, 5, and 6 are uncertainties associated with the neutron flux determination. 26

4.1 Collimations used in the Alpha-Gamma experiment. 53

4.2 Measured halo for each running configuration. 54

5.1 Isotopic composition of batch 455A Plutonium [Richardson, 1993]. . . 91

6.1 Alpha-Gamma α-detector solid angle (Ω) for the three beam sizes used in the calibration. 102

6.2 Silicon γ as a fraction of the total measured 478 keV signal for each running configuration. 103

6.3 Incoherent scattering and absorption cross sections for isotopes of boron and carbon. 107

6.4 Lost 478 keV γ due to scattering in B_4C target. 109

6.5 Gamma detector dead time corrections for the thick target with each collimation scheme. 110

6.6 Flux monitor solid angle corrections for the three calibration configurations. 110

6.7 A summary of the corrections from neutron backscattering in the flux monitor target. 117

7.1 Run schedule for statistical accumulation. 121
7.2 $\frac{1}{\gamma/\mathrm{FM}}\frac{1}{\alpha/\gamma}$ values for each detector-collimation pair. 121
7.3 Table of corrections for ϵ_0^{AG} data. 123
7.4 ϵ_0^{AG} values for each collimation. 124
7.5 Final uncertainties from the Alpha-Gamma experiment listed largest to smallest. 125

8.1 Information about additional ^{6}Li foils calibrated with the Alpha-Gamma device. 129
8.2 Foil density-dependent correction values for Li930118-H6 and Li930119-H5. 129
8.3 Efficiency results for Li930118-H6 and Li930119-H5. 130
8.4 Projected uncertainty budget for a new run of the beam lifetime experiment. 132

A.1 The results of the two magnetic trap neutron lifetime experiments. The result of [Ezhov, 2009] comes from conference presentations, but a final result has not been published. 145
A.2 A compilation of published beam lifetime experiments. 146
A.3 A compilation of published UCN bottle lifetime experiments. 146

List of Figures

1.1 A plot of all published neutron lifetime measurements to-date. See appendix A for further information. 8

1.2 The measurements used for the 2004 PDG world average (see appendix A). The shaded band is a weighted fit to the data. 13

1.3 The measurements used for the 2011 PDG average (see appendix A). The shaded band is a weighted fit to the data, inflated by $\sqrt{\chi^2/\nu} = 2.68$. 13

2.1 Proton trap and neutron flux monitor [Wietfeldt, 2007]. 16

2.2 Lithium-6 neutron absorption cross section [Carlson et al., 1993]. . . . 18

2.3 The evaporation rig used for the lifetime ^{6}Li deposit [Pauwels et al., 1995]. 23

2.4 Measured (points) and calculated (line) deposit profile for the ^{6}LiF foils [Pauwels et al., 1995]. 24

2.5 Lithium-6 thermal neutron cross section from the last three ENDF evaluations [Carlson and Bhat, 1982; Carlson et al., 1993, 2009]. . . . 26

3.1 Schematic of the neutron calorimeter [Chowdhuri, 2000]. 29

3.2 Detection geometry for the Alpha-Gamma device (not to scale) . . . 34

4.1 Schematic of the reactor core. Neutrons are produced in ^{235}U fuel rods (A) and cadmium shim-arms (B) serve as control rods. A vessel filled with 20 K liquid hydrogen (C) is the source for cold and thermal neutrons for the guide hall [Williams, 2007]. 43

4.2 A neutron incident on a material boundary. 44
4.3 The NIST Center for Neutron Research confinement building and guide hall [Dimeo, 2009]. 44
4.4 Reflectivity and rocking curves for the two candidate monochromators [Mumm, 2005]. 46
4.5 A simulation of the beam spot on the Alpha-Gamma target foil with a 15mm upstream collimator and an 8.38mm downstream collimator. The black circle represents the active area of the thin target. 48
4.6 FujiBAS neutron imaging plate image of the NG6m beam at the shutter exit and approximate sighted center. 49
4.7 Measurement of the beam tilt on NG6m using a neutron-sensitive FujiBAS image plate. 52
4.8 The "galaxy" effect - imaging artifacts appear as the plate reader scans through areas of high intensity. A red box shows the approximate extent of the "galaxy." The image is displayed in a small PSL-range greyscale to better display the effect. 54
4.9 Beam images at the Alpha-Gamma foil location with C1 = 15 mm and C2 = 7.2, 8.38, and 10.5 mm. The grid spacing is 4 mm. The white circle corresponds to the edge of the active area of the thin ^{10}B foil. Image orientation is arbitrary, but the 15/8 image is representative of the image that would be seen looking from the Alpha-Gamma alpha detector towards the target foil. 55
4.10 Radial profile of a 15/8 beam image. The red dots represent the PSL value of each pixel within the region of interest. The vertical line at 19 mm marks the edge of the active radius of the thin ^{10}B deposit and the line at 25 mm marks the edge of the steel mask of the foil holder. 56
4.11 A hypothetical 1 % beam halo. 58
4.12 Neutron scattering cross section for beryllium [Wahba, 2002]. 59
4.13 The 2007 wavelength test setup. 63

4.14 Wavelength measurements from the 2007 wavelength setup. The shaded band is a weighted constant fit to the data. 64
4.15 A schematic of the new wavelength measuring apparatus installed on NG6m. 64
4.16 Detail of crystal housing and positioning device. 65
4.17 An aluminum frame ensures the encoder and rotation stage are parallel to each other. 67
4.18 The aluminum alignment block inside the crystal housing. 68
4.19 A typical rocking curve pair from the new wavelength setup. 69
4.20 A tilt curve pair from the new wavelength setup. The dashed line represents the tilt that best minimizes the parallel centroid and maximizes the antiparallel centroid. 70
4.21 An aluminum block scanned over a wide angle range demonstrates the sinusoidal neutron background from incoherent scattering. 70
4.22 Measured Bragg angles from the new wavelength setup. The centroid of the shaded band comes from a weighted constant fit ($\chi^2/\nu = 23.2$) and the uncertainty is given by the standard deviation of the data set. 71
4.23 The $\lambda/2$ rocking curve for the unfiltered beam. 72
4.24 The $\lambda/2$ rocking curve for the filtered beam. Detectors were moved to the close position to increase count rate. 73

5.1 Alpha-Gamma detection geometry. 75
5.2 A rendering of the Alpha-Gamma vacuum can, surrounding support frame, and the neutron flux monitor. 76
5.3 A photograph of the Alpha-Gamma device connected to the neutron flux monitor. The wavelength measuring frame is just upstream of the flux monitor. 77
5.4 The target foil holder used in the Alpha-Gamma device. Three kinematic features on the flange mate with the vacuum can flange. . . 77

5.5 A rendering of the Alpha-Gamma vacuum can. 79
5.6 A side-view of the experiment layout. 81
5.7 Block diagram of a detector's counting and spectroscopy electronics. . 82
5.8 Cartoon of SCA operation. 83
5.9 Alpha-Gamma device electronics diagram. FMA - FMD are the four neutron flux monitor PIPS detectors, AGA is the Alpha-Gamma PIPS detector, FC is an upstream fission chamber and TG and BG are the top and bottom HPGe detectors. 84
5.10 Gamma-ray spectrum from the thin ^{10}B target 88
5.11 Gamma-ray spectrum from the thick ^{10}B target 88
5.12 Charged particle spectrum from the ^{239}Pu source. 89
5.13 Charged particle spectrum from the thin ^{10}B target. 89
5.14 ^{239}Pu low-solid angle counting stack. 92
5.15 Activity of 49Si-3-3 measured with the Alpha-Gamma PIPS detector. 93
5.16 A plot of α/FM for our calibration runs. 94
5.17 A typical measurement of α/Tγ from our calibration runs. 94
5.18 A typical measurement of Tγ/FM from our calibration runs. 95
5.19 Data showing the long-term gamma rate drift in the bottom gamma detector due to drift in detector efficiency. 96
5.20 An example of the triplet correction method on data from the top gamma detector. 97

6.1 A plot of the ratio Tγ/FM versus number of silicon wafers stacked behind the ^{10}B target. The data is fit to a line to extract the slope. The residuals are shown in the upper plot. 104
6.2 A measurement of the (101) reflection in the boron carbide target. . . 105
6.3 An illustration the different path lengths through the thick target. The travel distance through the target to the bottom detector is greatly exaggerated. 108

6.4 A plot of Tγ/FM for three thicknesses of B_4C (0.321 mm, 0.571 mm, and 0.892 mm). The data is fit to a line to extract the slope. The residuals are shown in the upper plot. 108
6.5 Solid angle as a function of position on the flux monitor foil 111
6.6 Beam images at the flux monitor foil location with C1 = 15 mm and C2 = 7.2, 8.38, and 10.5 mm. The grid spacing is 4 mm. The white circle corresponds to the edge of the active area of the ^{6}Li foil. 112
6.7 An illustration of how neutron scattering affects the two orientations of the neutron flux monitor target foil 114
6.8 The measured enhancement from forward scattered neutrons in the IRMM experiment [Scott et al., 1995]. 116
6.9 A fit of α/FM to equation 6.13 is used to determine ϵ_{Si} from the data. 117

7.1 Plots of the results of the analysis for $\frac{1}{\gamma \mathrm{FM}} \frac{1}{\alpha/\gamma}$ for the six detector-collimation configurations. 120
7.2 A plot of ϵ_0^{AG} for each collimation-detector pair. Only statistical uncertainty is shown. The red line is a weighted constant fit to the data. 124

B.1 SCA window for the charged particle spectrum from the ^{239}Pu source. 148
B.2 Activity of 49Si-3-3 measured with the 76mm stack. 149
B.3 Activity of 49Si-3-3 measured with the 38mm stack. 150
B.4 Measurements of the activity of 49Si-3-3 from 1992 to 2006. 151

Chapter 1

Theory of Neutron Beta Decay

The decay of a free neutron into a proton, electron, and electron antineutrino is the simplest example of nuclear beta decay. As the fundamental semileptonic decay, the study of neutron decay is an important test of the charged-currect sector of the standard model. A precise measurement of the neutron lifetime addresses important questions in particle physics and cosmology.

1.1 Discovery of the Neutron

The idea that heavy neutral particles were present in the nucleus of atoms was first suggested by Rutherford in 1920 [Rutherford, 1920] to account for the difference between atomic mass and atomic number. It would be another twelve years before Chadwick presented his discovery of the neutron [Chadwick, 1932]. He correctly identified the penetrating neutral radiation generated by alpha-irradation of beryllium as the neutron, not a gamma ray. Two experiments performed by Chadwick and Goldhaber in 1934 and 1935 [Chadwick and Goldhaber, 1934, 1935] definitively proved that the neutron mass was greater than that of the proton and electron. As such, it put to rest Rutherford's idea that the neutron was a tightly bound state of the two. The neutron was a new, fundamental constituent of the atom. Furthermore, that it was heavier than the hydrogen atom implied that decay was possible.

1.2 Neutron β^--Decay in the Standard Model

The beta decay Hamiltonian was first postulated by Fermi, in analogy to the QED Hamiltonian, to be a four-fermion vector interaction involving the neutron, proton, electron, and electron antineutrino [Fermi, 1934]. It is now understood to be moderated by the W^- boson, but the large mass of the W^- makes the point interaction a very good approximation. The exclusively vector nature of the interaction was called into question by Gamow and Teller, who proposed that the Hamiltonian be generalized to accomodate all Lorentz-invariant interactions forms [Gamow and Teller, 1936]. This added the scalar (S), pseudoscalar (P), tensor (T), and axial vector (A) terms to the vector (V) term.

The P term is highly suppressed in beta decay in the nonrelativistic limit. The S and V interactions produce the leptons in a spin zero state (Fermi decay), and the A and T interactions produce them in a spin one state (Gamow-Teller decay). This leads to a $\Delta J = 0$ selection rule for the Fermi decays, and $\Delta J = 0, \pm 1$ for Gamow-Teller. Both cases were observed, making it clear that both Fermi and Gamow-Teller terms must be in the Hamiltonian. Through additional experiments and theory, it was determined that the weak current is $V - A$, with no evidence for S or T. The beta decay Hamiltonian is given by:

$$\mathcal{M} = \left[G_V \bar{p}\gamma_\mu n - G_A \bar{p}\gamma_5\gamma_\mu n\right]\left[\bar{e}\gamma_\mu\left(1-\gamma_5\right)\nu\right] \tag{1.1}$$

where $\bar{p}$, n, $\bar{e}$, and ν are the proton, neutron, electron, and neutrino spinors. The typical $\gamma_\mu\left(1-\gamma_5\right)$ term is used at the lepton vertex. For the $n \rightarrow p + W^-$ vertex, additional coupling constants $G_V = G_F V_{ud} C_V$ and $G_A = G_F V_{ud} C_A$ must be introduced to account for the strong forces within the nucleon that can alter the relative strengths of the vector and axial vector currents. $G_F = 1.16637(1) \times 10^{-5}$ GeV^{-2} is the Fermi weak coupling constant (measured in muon decay), V_{ud} is the first element of the Cabbibo-Kobayashi-Maskawa (CKM) matrix, and C_V and C_A are

constants as defined in the interaction Hamiltonian proposed by Jackson, Trieman, and Wyld [Jackson et al., 1957]. We know from experimental observation and from the Conserved Vector Current hypothesis that $C_V = 1$.

This Hamiltonian can be used to determine the probability for neutron decay per unit time:

$$dW = (2\pi)^{-5}\delta(E_e + E_\nu - \Delta)\frac{1}{2E_e}\frac{1}{2E_\nu}d^3\mathbf{p_e}d^3\mathbf{p}_\nu|\mathcal{M}| \tag{1.2}$$

where E_e, $\mathbf{p_e}$, E_ν, and $\mathbf{p}_\nu$ are the total energy and momentum for the electron and electron antineutrino. $\Delta = 1.29333214(43)$ MeV is the neutron-proton mass difference. We start by integrating over antineutrino momentum and electron phase space:

$$\frac{dW}{dE_e} = \frac{1}{2\pi^3}(G_A^2 + 3G_V^2)E_e|\mathbf{p_e}|(\Delta - E_e)^2 \tag{1.3}$$

and then over electron energy, to arrive at the exponential decay constant:

$$W = \frac{(G_V^2 + 3G_A^2)}{2\pi^3}f_R \tag{1.4}$$

where f_R is a calculated phase space factor that includes radiative corrections. The neutron lifetime is found by taking the inverse of W:

$$\tau_n = \frac{1}{W} = \frac{2\pi^3}{(G_V^2 + 3G_A^2)f_R} \tag{1.5}$$

Thus, measurements of the neutron lifetime are a way to measure the weak coupling constants. G_V is of principle interest because it is used to determine $|V_{ud}|$. The first row of the CKM matrix ($|V_{ud}|$, $|V_{us}|$, $|V_{ub}|$) provides the simplest experimental avenue to its unitarity.

The two most precise determinations of G_V, and thus $|V_{ud}|$, come from super-allowed $0^+ \rightarrow 0^+$ nuclear beta decays and from measurements of neutron beta decay. The constancy of G_V has been verified at the level of 1.3×10^{-4} through measurements of the $\mathcal{F}t$ ($\mathcal{F}$ is the statistical rate function after radiative corrections

and t is the decay half-life) values of superallowed $0^+ \rightarrow 0^+$ nuclear beta decays [Hardy and Towner, 2009]. These nuclei undergo pure vector decays with minimal nuclear structure uncertainties due to the maximal overlap between the initial and final states. The $\mathcal{F}t$ value is dependent on the decay energy, the beta decay lifetime of the parent nucleus, and the branching ratio for the decay.

In neutron beta decay, $G_A \neq 0$, and must be measured. This is accomplished by measurement of both the neutron lifetime and a beta decay correlation which is sensitive to $g_A \equiv G_A/G_V$ (e.g. neutron-spin electron-momentum correlation). Currently, this method is not competitive with that of superallowed beta decays [Nakamura et al., 2010], but its ultimate precision is greater due to smaller theoretical uncertainties. If the precision of neutron lifetime measurements and beta decay correlations can be improved by an order of magnitude, this method will be the best way to determine $|V_{ud}|$.

1.3 Neutron β^--Decay and Big Bang Nucleosynthesis

Big Bang nucleosynthesis (BBN) is a model that predicts the primordial abundance of the light (H, ^{2}H, ^{3}He, ^{4}He, ^{6}Li, and ^{7}Li) nuclei produced in the early universe. The early universe is characterized by the time since the Big Bang (t) and the temperature (T). The BBN model takes as its input the ratio of neutrons to protons at the moment the universe became cool enough to allow the formation of nuclei ($t \approx 100$ s). Neutron beta decay plays two roles in determining the neutron-proton ratio prior to this freeze out. For $t = 0.1$ - 1 s, the temperature is sufficiently high that the following reactions occur in equilibrium:

$$n + e^+ \leftrightarrow p + \bar{\nu}$$

$$p + e^- \leftrightarrow n + \nu$$

and the ratio of neutrons to protons is given by a Boltzman factor:

$$n/p = e^{-\left(\frac{\Delta}{T}\right)}$$

where Δ is the mass difference between the proton and neutron ($m_n - m_p = 1.293$ MeV). At $t \approx 1$ s ($T \approx 1$ MeV), the weak interaction rate (which falls as T^5) decreased to a level that these reactions fell out of equilibrium (the so-called "nucleon freeze-out"), leaving the neutron to proton ratio at roughly 1 to 6. Light element formation began at $t \approx 100$ s and essentially all neutrons were bound in nuclei by $t = 180$ s, allowing neutron beta decay to alter the neutron proton ratio for over a minute. Thus, the neutron lifetime plays a very straightforward role in determining the neutron proton ratio during this era. Additionally, the $n \leftrightarrow p$ reactions that occurred prior to the nucleon freeze-out depend on the strength of the charged weak interaction and can be accessed by measurements of the neutron lifetime. As such, the neutron lifetime plays two important roles in theoretical BBN calculations of the primordial element abundances. Our ability to test these predictions is currently limited by the precision of the experimental determination of the light element abundances. As these measurements improve, it will become important to improve the precision of the theoretical predictions. The uncertainty in the world average neutron lifetime value is the dominant source of uncertainty in theoretical predictions of the ^{4}He abundance [Lopez and Turner, 1999]. Further work towards higher precision neutron lifetime measurements is needed.

1.4 Neutron Lifetime Measurements

Neutron β-decay follows the exponential decay law:

$$N(t) = N(0)\mathrm{e}^{-t/\tau_n} \tag{1.6}$$

where $N(t)$ is the population of neutrons at time t, $N(0)$ is the initial population of neutrons, and τ_n is the mean lifetime of the neutron. An equivalent differential form of the law is:

$$\dot{N}(t) = \frac{\mathrm{d}}{\mathrm{dt}} N(t) = \frac{\mathrm{d}}{\mathrm{dt}} \left(N(0) e^{-t/\tau_n} \right) = -\tau_n^{-1} N(t) \tag{1.7}$$

where the rate of decays in a sample and the size of the sample are known. This differential form can be used with a beam of neutrons, in which each sample is observed for a very short time.

The mass difference between a neutron and its decay products is very small, so it was not unexpected that the neutron lifetime would be quite long. Observing neutron decay and measuring the neutron lifetime requires a large sample of neutrons that are present in the experiment long enough to observe decays. The first neutron sources were made by encapsulating α-sources (e.g. radium, polonium) in low-Z materials (e.g. beryllium) with an (α,n) reaction. These sources were diffuse, produced small quantities of neutrons (the [Chadwick and Goldhaber, 1935] experiment used a Po-Be source of approximately 1 s^{-1} activity) at high energy ($\sim$ MeV). Cyclotron neutron sources improved neutron intensities by $\sim 10^6$, but were still limited to fast neutrons and hence, very low detection probabilities. Observation time could be increased drastically through "thermalization" of the neutrons. Fermi discovered that neutrons can be slowed down by repeated elastic collsions with light nuclei. This thermalization effect reduced neutron velocities to $\sim 10^3$ m/s (energies of $\sim 10^{-1}$ eV). However, elastic scattering has the additional effect of randomizing neutron directions, turning even well-collimated sources into isotropic ones. The effective gain on total observed decay rate would be very small.

It was clear that a measurement of the neutron lifetime would require a high intensity source of thermal neutrons. This was made possible when the first nuclear reactor at Oak Ridge, Tennessee was put into operation in Novermber of 1943. This graphite-moderated reactor was capable of a thermal neutron flux of $\sim 10^{12}$ $\mathrm{cm}^{-2}\mathrm{s}^{-1}$ at the core, which could produce a detectable rate of decays for a reasonable length

of the beam ($\sim 10^{-1}$ m). In the Snell experiments [Snell and Miller, 1948; Snell et al., 1950], an electron-proton coincidence detector was fashioned to overcome the very large background from ionizing radiation. A decay rate of (0.67 ± 0.05) cpm was measured. Only a very conservative estimate of the lifetime (14-43 minutes) was made due to difficulties in determining detector efficiencies.

A plot of all published neutron lifetime measurements is found in figure 1.1. The first proper measurement of the neutron lifetime was performed by Robson in 1951 [Robson, 1951]. The experiment used an electron-proton coincidence system to determine the decay rate and manganese foils to determine the neutron flux. The techniques used to determine neutron flux in this experiment have been honed for use in modern-day beam lifetime experiments. By using a foil whose cross section is inversely proportional to the velocity of the incident neutron [Fermi et al., 1934], Robson determined the capture flux of the beam, which is weighted in precisely the same way as the probability of decay in the decay volume (see sections 2.2 and 2.3). In principle, this foil activation method requires knowledge of the foil mass, the manganese neutron capture cross section, and the efficiency of the offline counting system used to determine the activity. However, Robson chose to perform an absolute calibration of the foil with a second, well-calibrated detector. This technique is, in some sense, the early ancestor of the Alpha-Gamma technique described in this dissertation (section 3.2).

Significant improvements to background subtraction, neutron flux assessment, and detector efficiency determination led to a set of three measurements [Sosnovsky et al., 1959; Christensen et al., 1972; Bondarenko et al., 1978] that all claimed uncertainties of 1-3 %. Significant problems remained - only the Sosnovsky experiment was in good agreement with the ~ 10 % lifetime measurements, and all three measurements were in disagreement with each other. This represented the first "neutron lifetime problem." This problem led to a groundswell of new lifetime experiments and the development of new techniques. Two major developments led to a significant improvement in the precision of neutron lifetime measurements:

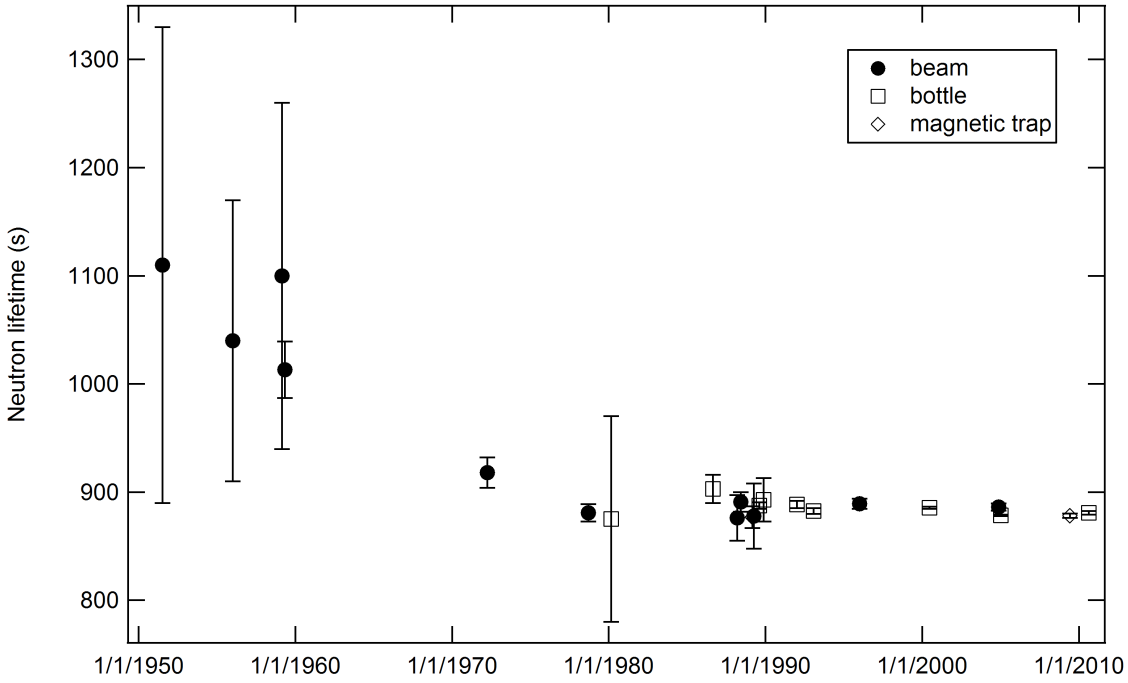


Figure 1.1: A plot of all published neutron lifetime measurements to-date. See appendix A for further information.

- The development of ultracold neutron (UCN) sources and material "bottles" to contain UCN
- The development of high-precision proton and neutron counting for beam lifetime experiments

Ultracold neutrons have kinetic energies of ~ 100 neV. The gravitational potential energy of a neutron is roughly 100 neV/m, so UCN can be confined vertically by a sufficiently deep trap. The $\mu \cdot B$ potential is approximately 60 neV/T, so UCN can be trapped in inhomogeneous magnetic fields of several Tesla. Many materials have Fermi effective potentials on the order of ~ 100 neV, so UCN can be totally reflected in carefully prepared "bottles" and observed for times approaching the neutron lifetime. Aside from the toroidal magnetic trap of [Paul et al., 1989], UCN bottles used a combination of vertical confinement with gravitational trapping and material "walls." The UCN are introduced into the bottle or are generated in-situ. After a storage time Δt, the neutrons are extracted from the bottle and counted. The neutron lifetime in the trap is determined by measuring the ratio of surviving neutron populations N_1 and N_2 for two different storage times Δt_1 and Δt_2:

$$\tau = \frac{\Delta t_2 - \Delta t_1}{\ln\left(\frac{N_1}{N_2}\right)} \tag{1.8}$$

The measured lifetime is τ, a combination of the neutron lifetime and all trap-related loss mechanisms:

$$\frac{1}{\tau} = \frac{1}{\tau_n} + \frac{1}{\tau_{\text{inel}}} + \frac{1}{\tau_{\text{cap}}} + \frac{1}{\tau_{\text{other}}} \tag{1.9}$$

where τ_n is the true beta decay lifetime, τ_{inel} is loss due to inelastic scattering off the walls, τ_{cap} is loss due to neutron capture on the walls, and τ_{other} represents losses from any additional mechanisms. The goal is to minimize and quantify these loss mechanisms. Material bottles made significant gains in storage lifetime by coating the walls of the bottle with Fomblin oil. Fomblin retains its low-viscosity at cryogenic temperatures, has a very low vapor pressure, and, most importantly, is hydrogen-free.

With its neutron reflective potential of 106.5 neV [Golub et al., 1991], Fomblin is an effective bottle surface. Using Fomblin as a coating material provides a reflective, smooth, renewable, repeatable, hydrogen-free surface to bottles that otherwise would have exposed cracks and potential hydrogen contamination on the surface. This liquid-wall strategy was first used in the MAMBO experiment [Mampe et al., 1989] to great effect, and was adopted by later bottle experiments. In parallel, it is essential to maximize UCN density in the bottle. This is done by improving UCN production at the source and improving UCN extraction methods. While useful UCN density was typically very low, the gains in observation time allowed measurements to quickly become competitive with the beam experiments.

Even though the magnetic confinement experiment of [Paul et al., 1989] could not compete with higher precision bottle measurements of the time [Mampe et al., 1989; Alfimenkov et al., 1992; Mampe et al., 1993], it represents a third class of neutron lifetime experiment with different systematic effects. Proper modeling of the interactions of UCN with a material wall is very complicated [Steyerl et al., 2010], and moving to a theoretically "cleaner" trapping system is desireable. A number of ongoing experiments [Ehzov et al., 2009; O'Shaughnessy et al., 2009] and experiments in development [Materne et al., 2009; Walstrom et al., 2009] employ magnetic trapping in some way.

Magnetic trapping has significant disadvantages as well. Half of the initial population of UCN are of the wrong spin state to be trapped and will be lost. Neutrons of the proper spin state can undergo depolarization in the trap and eventually become lost. The most pernicious effect comes from neutrons whose mechanical energy exceeds the trap potential but take significant time (on the order of τ_n) to escape the bottle due to their non-ergodic trajectories. A number of methods are employed to remove these "marginally trapped neutrons."

The success of UCN-based measurements led to increased adoption of the technique. Only the Sussex-ILL-NIST collaboration continued to develop beam based

experiments. In these experiments [Byrne et al., 1996; Nico et al., 2005b], a quasi-Penning trap composed of segmented electrodes was used to trap and count decay protons. The beginning and end electrodes were held at a voltage sufficient to trap the proton axially (+800 V), and a ~ 5 T field confined the proton radially. One end of the trap is periodically lowered to flush decay protons to a detector. Protons born in the central region were trapped with 100 % efficiency, and by clever manipulation of the decay volume proton trapping losses due to end effects were circumvented (see section 2.3). These experiments were the first to use the decay proton for neutron decay rate measurement. This required careful characterization of the proton detector efficiency due to the possibility of proton backscatter from the detector surface. The advantage of this configuration is the ability to detect the proton far away from the decay volume in a very low noise environment.

This collaboration also undertook a campaign to create thin ^{6}Li and ^{10}B foils for precision neutron counting. The ^{6}Li and ^{10}B cross sections are, to very good approximation, inversely proportional to neutron velocity ($\frac{1}{v}$) near thermal and are well-measured (see section 2.2). The foils were manufactured and characterized in collaboration with the Institute for Reference Materials and Measurements (IRMM). Particle detection is accomplished with silicon detectors masked by precision apertures whose solid angle can be determined by contacting metrology and α-source activity measurements. The efficiency of the detector is the product of the solid angle, the ^{6}Li(n,t) and ^{10}B(n,α) cross sections, and the amount of neutron absorbing material on the foil. For the final run of the experiment (using ^{6}Li foils), an uncertainty of 0.3 % was assigned to this efficiency (see section 2.4). This is a high-water mark for precision neutron flux determination, but was still the limiting systematic effect in the experiment.

This new class of sub-1 % ($\leq$ 10 s) uncertainty lifetime measurements spanned twenty years and made use of two entirely different methods. Eidelman *et al.* performed a weighted mean on the set of experiments with total uncertainty less than 10 s (shown in figure 1.2) and recommended a "world average" value of $\tau_n = 885.7 \pm 0.8$

s with a very reasonable chi-squared of 3.5 for 6 degrees of freedom [Eidelman et al., 2004]. This apparent resolution was short lived: in 2005, the Gravitrap II experiment reported $\tau_n = 878.5 \pm 0.76$ s, approximately 6.5 standard deviations from the world average [Serebrov et al., 2005]. Until recently, the Particle Data Group continued to present the 2004 recommended value and chose not to include the Serebrov result nor expand the uncertainty on their average. Instead, the average was deemed suspect, and workers within the field were asked to resolve the issue.

In recent years, the situation has become cloudier. In 2010, Pichlmaier *et al.* [Pichlmaier et al., 2010] published a new result ($\tau_n = (880.7 \pm 1.3 \pm 1.2)$ s) using the MAMBO II material bottle apparatus (a prior result from the MAMBO II apparatus remains unpublished). A magnetic-gravitational trap from Ezhov *et al.* has reported the success of their trapping methods [Ehzov et al., 2009], and a result of $\tau_n = (878.2 \pm 1.9)$ s has been presented at conferences [Ezhov, 2009]. This number includes only statistical uncertainty and as such is not yet included in averages but is still compelling. In June of 2011, the PDG world average neutron lifetime was updated [Nakamura et al., 2010]. The new evaluation took the average of the seven most precise measurements (see figure 1.3 and inflated the fit uncertainty by a scale factor given by the square root of the chi-squared per degree of freedom ($\sqrt{\chi^2/\nu}$). The new result is $\tau_n = (881.5 \pm 1.5)$. This method favors the most precise experiments, yet these experiments suffer from poor agreement. This situation is also unsatisfactory, and resolution must come from further investigation.

The source of the discrepancy amongst the most precise neutron lifetime measurements is likely an underestimation or incorrect determination of systematic effects in some experiments. As such, new higher-precision experiments will likely be necessary to definitively resolve the problem. However, some headway can be made if in-depth reassessment of systematic effects can be performed for the contributing experiments. The most likely areas of concern are determining the neutron spectrum, phase space, and loss mechanisms in UCN experiments, and assesment of the neutron density in beam experiments. Conflicting reanalyses have been performed for UCN

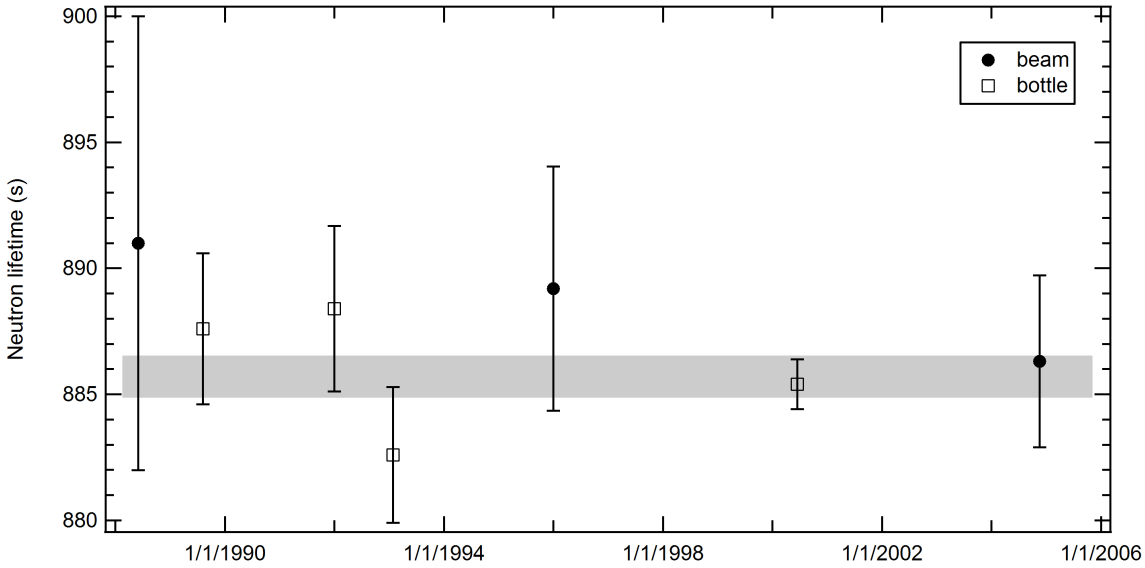


Figure 1.2: The measurements used for the 2004 PDG world average (see appendix A). The shaded band is a weighted fit to the data.

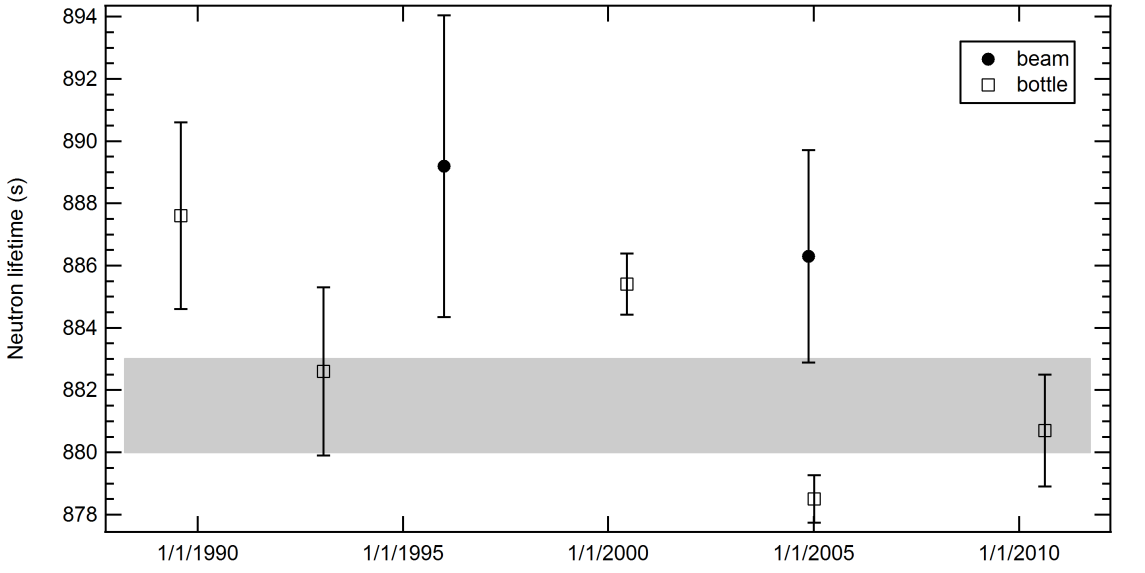


Figure 1.3: The measurements used for the 2011 PDG average (see appendix A). The shaded band is a weighted fit to the data, inflated by $\sqrt{\chi^2/\nu} = 2.68$.

experiments [Serebrov and Fomin, 2010; Steyerl et al., 2010]. The assesment of neutron density for beam experiments has been accomplished in the same way for both experiments included in the current average. As such, it is the most reasonable subject to investigate to better understand these experiments. In this dissertation, a high-precision absolute determination of the beam lifetime neutron flux monitor efficiency is performed.

Chapter 2

The NIST In-Beam Neutron Lifetime Measurement

The NIST in-beam neutron lifetime measurement [Dewey et al., 2003; Nico et al., 2005b] is the most precise determination of the lifetime measuring decays from a cold neutron beam. The experiment ran in 2000 at the NIST Center for Neutron Research (NCNR) and was stationed at NG6, where it used the broad spectrum of cold neutrons from a LH_2 moderator. A beam style experiment makes use of the differential form on the decay law:

$$\dot{N}(t) = \frac{\mathrm{d}}{\mathrm{dt}} N(t) = \frac{\mathrm{d}}{\mathrm{dt}} \left(N(0) e^{-t/\tau_n} \right) = -\tau_n^{-1} N(t) \tag{2.1}$$

where $N(t)$ is the neutron population at time t and τ_n is the mean neutron lifetime. The neutron lifetime is determined by knowing the instantaneous decay rate and number of neutrons present in a sample at time t. This is realized by measuring the neutron decay rate in a well-defined section of the neutron beam and measuring neutron density. Each neutron is observed for a short period of time, but the number of neutrons is very large.

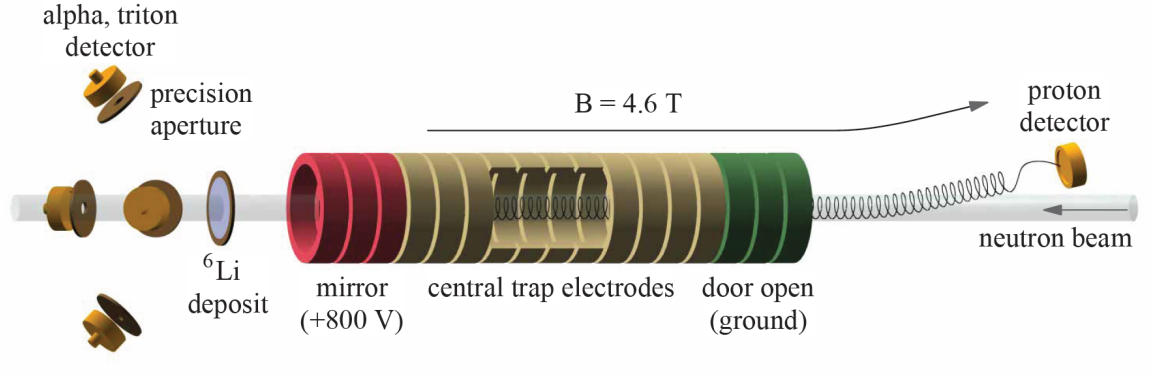


Figure 2.1: Proton trap and neutron flux monitor [Wietfeldt, 2007].

2.1 Measuring Neutron Decays

The ideal trapping volume is one in which all neutron decays inside the volume are detected and decays outside the volume go undetected. In the NIST measurement, this was accomplished with a proton trap. Protons from neutron decay have at most 751 eV of kinetic energy, so an 800 V electrostatic potential from the proton trap axially confines the decay protons (provided the trap is a square-well potential) to a middle region of grounded electrodes with total length L. The proton trap sits in the bore of a superconducting solenoid. The solenoid generates a 4.6 T magnetic field, which confines the decay proton radially.

A reactor source generates a high flux of neutrons in a broad spectrum of energies. The beam of neutrons is characterized by a velocity-dependent differential flux $(\frac{\text{neutrons}}{\text{cm}^2 s} \times \frac{1}{\text{cm/s}})\ I(v)$. For a decay volume of length L, a neutron with velocity v will be present in the decay volume for a time equal to $\frac{L}{v}$. The number of neutrons N_n in the volume at any time is given by the double integral of the $\frac{L}{v}$-weighted differential flux over the area of the beam (A) and the range of neutron velocities:

$$N_n = \int_A \int_v \mathrm{d}aI(v)\frac{L}{v}\mathrm{d}v = L\int_A \int_v \mathrm{d}aI(v)\frac{1}{v}\mathrm{d}v \tag{2.2}$$

and, according to equation 2.1,

$$\dot{N}_n = -\tau_n^{-1} L \int_A \int_v \mathrm{d}a I(v) \frac{1}{v} \mathrm{d}v \tag{2.3}$$

But detection of neutron decays is accomplished by measuring the rate of detected protons ($\dot{N}_p$). The proton detector has an efficiency of ϵ_p, therefore the rate is given by:

$$\dot{N}_p = \epsilon_p \tau_n^{-1} L \int_A \int \mathrm{d}a I(v) \frac{1}{v} \mathrm{d}v \tag{2.4}$$

which is sufficient provided the neutron flux as a function of velocity is well-measured. This could be done most easily on a monochromatic beam, but the detected proton rate from the $\sim 10^3$ lower flux beam would be prohibitively small. Instead, the neutron flux measurement is performed in a way that it is naturally $\frac{1}{v}$ weighted, and the resulting lifetime has no spectral dependence (see section 2.3)

2.2 Measuring Neutron Flux

The neutron flux is measured with a very thin (absorbs $\sim$1 % of the beam) ^{6}LiF deposit (95.65 % isotopic purity [Pauwels et al., 1995]) of known mass (see section 2.3). A neutron incident on ^{6}LiF follows the reaction

$$\mathrm{n} + {}^6\mathrm{Li} \rightarrow \alpha(2.07\mathrm{MeV}) + {}^3\mathrm{H}(2.72\mathrm{MeV})$$

The ^{6}Li neutron capture cross section is, to very good approximation, proportional to the inverse of the incident neutron velocity for cold and thermal neutrons (figure 2.2):

$$\sigma(v) = \frac{\sigma_0 v_0}{v} \tag{2.5}$$

where $\sigma(v)$ is the cross section at velocity v and σ_0 is the cross section at $v_0 = 2200$ m/s (a thermal neutron). Such materials are known as "$\frac{1}{v}$" nuclei. This $\frac{1}{v}$ nature can be distorted by the presence of resonances.

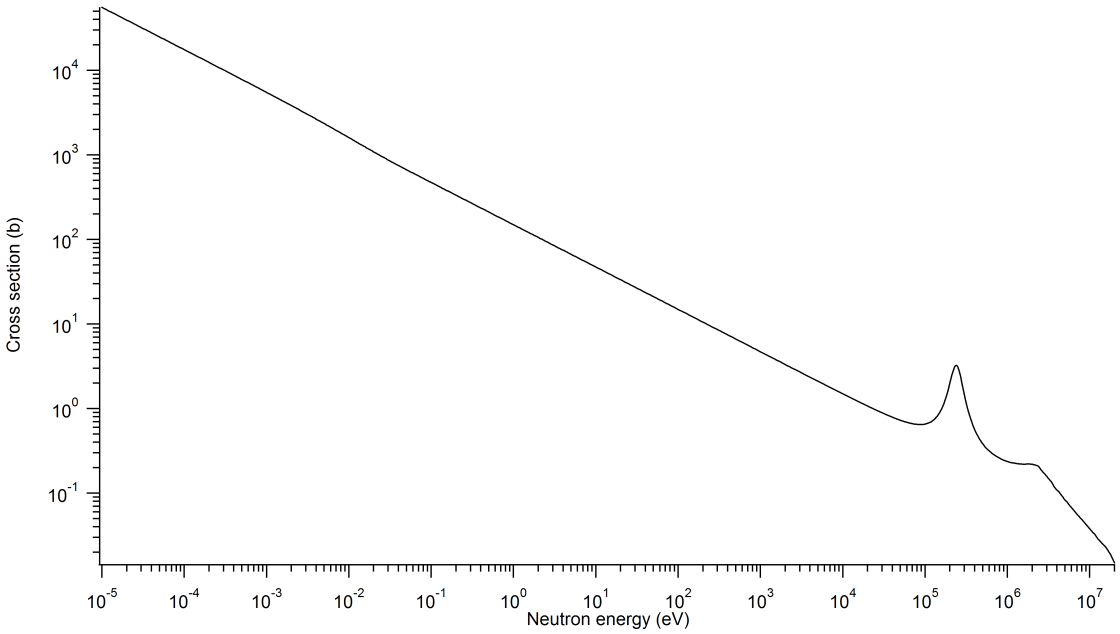


Figure 2.2: Lithium-6 neutron absorption cross section [Carlson et al., 1993].

The Westcott g-factor [Westcott, 1955] is a quantitative measure for how $\frac{1}{v}$ a nuclei is:

$$\mathrm{g}(T) = \frac{1}{\sigma_0} \frac{\int_0^\infty \sigma\left(E\right) M\left(E,T\right) dE}{\int_0^\infty M\left(E,T\right) \left(E/E_0\right)^{\frac{1}{2}} dE} \tag{2.6}$$

where E is the neutron energy, E_0 is the thermal neutron energy, and $M(E,T)$ is the Maxwell-Boltzmann distribution of neutrons with characteristic temperature T. An ideal $\frac{1}{v}$ nuclei has g = 1. The two target nuclei chosen for the lifetime experiment (^{6}Li, ^{10}B) have g-factors very close to unity (table 2.1). The deviation from $g = 1$ is due to the presence of small Lorentzian tails from resonances at higher energies. ^{10}B was used exclusively in the early runs of the experiment, but concerns about material loss from the deposit (via water vapor reacting with the boron to create boric acid) lead the NIST collaboration to use a ^{6}LiF deposit [Lamaze, 2010].

The alpha and triton are detected in four surface barrier detectors. Each detector is masked by a precision aperture to define the detector solid angle. The detectors view the foil from the four cardinal directions and face it at an angle of 45°. This configuration makes the total detector solid angle first-order insensitive to position

Table 2.1: Westcott g-factors for ^{6}Li and ^{10}B at $T = 20.44$ °C [Chowdhuri, 2000; Lamaze et al., 1988].

Nucleus	Reaction	σ_0 (b)	Resonances (keV)	g-factor
^{6}Li	^{6}Li(n,t)α	938.5(13)	248, 2149, 2490, 2900	0.9997
^{10}B	^{10}B(n,α)^{7}Li	3835(9)	130, 370, 530, 1830, ...	0.9997

on the foil. The observed rate is related to the neutron beam rate incident on the foil by the efficiency $\epsilon_{FM}(v)$

$$\epsilon_{FM}(v) = \rho\Omega\sigma(v) = \rho\Omega\sigma_0\frac{v_0}{v} = \epsilon_0\frac{v_0}{v} \tag{2.7}$$

where ρ is the areal density of the ^{6}LiF deposit, Ω is the total solid angle to the four detectors, σ_0 is the ^{6}Li thermal neutron cross section ($v = v_0$ =2200 m/s), and $\epsilon_0 = \rho\Omega\sigma_0$ is the efficiency of the detector for thermal neutrons. The areal density of the deposit and the solid angle to the four detectors are a function of position on the foil, but these effects are small and well-known (see section 6.4 for details). As seen in table 2.1, the ^{6}Li cross section is, to very good approximation, inversely proportional to the incident neutron velocity. Assuming unit efficiency for ~2 MeV charged particles incident on a surface barrier detector, the rate of detected particles ($\dot{N}_{\alpha+t}$) is then:

$$\dot{N}_{\alpha+t} = \int_A \int \mathrm{d}aI(v)\epsilon_{FM}(v)\mathrm{d}v = \epsilon_0 v_0 \int_A \int \mathrm{d}aI(v)\frac{1}{v}\mathrm{d}v \tag{2.8}$$

2.3 Determining the Neutron Lifetime

By expressing the lifetime in terms of the ratio of the two observable rates expressed in equations 2.4 and 2.8, the velocity-dependent integrals cancel:

$$\tau_n = \epsilon_p \left(\frac{L}{\dot{N}_p}\right) \frac{\dot{N}_{\alpha+t}}{\epsilon_0 v_0} \tag{2.9}$$

and the experiment is reduced to the measurement of five observables.

$\left(\frac{L}{\dot{N}_p}\right)^{-1}$ is the measured rate of decay protons per unit length of trap. Proton detection is not continuous. To detect trapped protons, the electric field must be lowered. The upstream trap electrodes are grounded and then arranged in a gentle "ramp" to push the freed protons towards the proton detector. Ideally, the trapping length generated by the Penning trap would be a square well potential. However, this ideal setup cannot be realized, and the actual trap length will have end effects from an imperfect field. The experiment was designed to work around this effect. The Penning trap electrodes are made of precisely machined quartz cylinders coated with gold. By changing the position of the "mirror" electrodes, the trap length is altered. The electrode spacings have been measured *in situ* to a precision of 5 μm, so their contribution to the total length of the trap is very well known. The total length L of the trap is given by:

$$L = nl + L_{\text{end}} \tag{2.10}$$

where n is the number of electrodes, l is the length of an electrode (and its adjacent spacer) L_{end} is the unknown (but constant) extra trapping length due to the imperfect square well potential. Assume proton rate $\dot{N}_p^A$ is measured for n^A electrodes and proton rate $\dot{N}_p^B$ is measured for n^B electrodes. Then we have:

$$\frac{L}{\dot{N}_p} = \frac{(n^B l + L_{end}) - (n^A l + L_{end})}{\dot{N}_p^B - \dot{N}_p^A} = \frac{n^B l - n^A l}{\dot{N}_p^B - \dot{N}_p^A} \tag{2.11}$$

and the dependence on L_{end} is removed. $\frac{L}{\dot{N}_p}$ depends solely on the count rate and the physical length measurements of the electrodes.

Decay protons are accelerated by an approximately -25 kV potential at the detector surface to reduce proton backscatter. Some protons backscatter off the surface barrier detector dead layer and are not detected. Higher order processes such as backscatter followed by turnaround in the steering field cannot be well-simulated so a measurement of ϵ_p is needed. This was done by use of different acceleration

potentials and detectors with varying dead layers, allowing for an extrapolation based on SRIM-calculated backscattered fractions [Ziegler, 2008]. The neutron lifetime result is plotted versus backscattered fraction, and an extrapolation to zero backscattered fraction is performed to arrive at the final neutron lifetime.

The neutron flux monitor efficiency (ϵ_0) is calculated from the product of detector solid angle, ^{6}Li foil areal density, and ^{6}Li thermal neutron cross section. The detector solid angle is defined by a stainless steel frame that holds both the target foil and the masks for the four passivated implanted planar silicon (PIPS) detectors. This rigid frame is designed to be demountable, allowing for occasional solid angle measurements with contact metrology techniques. The solid angle can also be determined by use of α-sources that are designed to fit in the foil holder. NIST maintains a repository of α-sources whose absolute activity has been measured. The known absolute activity and the observed α-rate in the neutron flux monitor are all that is needed to determine the solid angle (provided that the material spot of the α-source is small). These two measurement techniques were demonstrated to agree to 0.1 %, and a final result of $\frac{\Omega}{4\pi} = 0.004196 \pm 0.1\,\%$ was used.

Accurate determination of the foil areal density requires measurements of the amount of ^{6}Li and shape of the deposit. Careful preparation of the foils makes this possible. The foils were produced and characterized in a joint effort between NIST and the IRMM in Geel, Belgium. While uniformity of the deposit is a desireable feature, what is ultimately necessary is a well-*characterized* deposit. That is, the radius and profile of the deposit must be well-understood. A sharp edge is very important in order to determine areal density. The foil deposition uses a custom evaporation rig based on a rotating multi-substrate holder [Pauwels et al., 1995]. A tantalum crucible holding ^{6}LiF is placed approximately 40 cm from the rotator. The substrate holder keeps seven targets at normal incidence to the particle flux that is generated by heating the crucible. The entire substrate holder orbits the crucible ("yearly" rotation), and the individual holders rotate ("daily" rotation). Careful choice of the periods of these two rotations improves the uniformity of distribution in

the event that the evaporation cone is asymmetric. The masking apertures for each foil holder are carefully prepared with optical grinding methods to ensure that they lie flush against the substrates. To ensure that the edge of the apertures are sharp, the final enlargement of the bore is done by clamping pairs of apertures together and carefully grinding to a diameter of 38 mm.

The deposits used in the lifetime experiment were evaporated on Si substrate, but some evaporations were done on stainless steel. These deposits were used to evaluate the radial distribution of deposition. The density was determined experimentally by a visible light spectrophotometer and was calculated from the known dimensions of the evaporation rig and the rotation speeds. As seen in figure 2.4, the measured and derived profiles agree very well. The edge of the deposit was measured by microscope and Talistep recording, and the deposit diameter was measured by Abbe-comparitor [Pauwels et al., 1995].

A combination of relative reaction rate comparison and isotope dilution mass spectrometry (IDMS) is used to determine of the amount of ^{6}Li in the deposits [Scott et al., 1995]. The $\alpha + \mathrm{t}$ reaction rate for each foil is measured on a thermal neutron beam using a rig similar to the flux monitor used in the lifetime. This establishes the ratio of masses between the foils. A foil is then destructively analyzed with IDMS in order to make an absolute measurement of its mass. The absolute mass of each foil is then determined from the IDMS-determined mass of the sacrificed foil and the ratios established by reaction rate comparison. In the lifetime experiment, only one ^{6}LiF foil (areal density $\bar{\rho} = 39.3\ \mu\mathrm{g/cm}^2 \pm 0.25\,\%$) was used.

The ^{6}Li thermal neutron cross section is not measured in this experiment and must be taken from evaluated nuclear data files. At the time of publication, the most recent evaluation was ENDF/B-VI, which reports $\sigma_0 = (941.0 \pm 1.3)$ b [Carlson et al., 1993]. This 0.14 % uncertainty comes from the combined-analysis uncertainty from R-matrix evaluation. Thus, the ENDF-determined ^{6}Li(n,t) thermal neutron cross section used does not come from one precision measurement at thermal neutron energy, but instead from a global evaluation of many neutron reactions. This is the

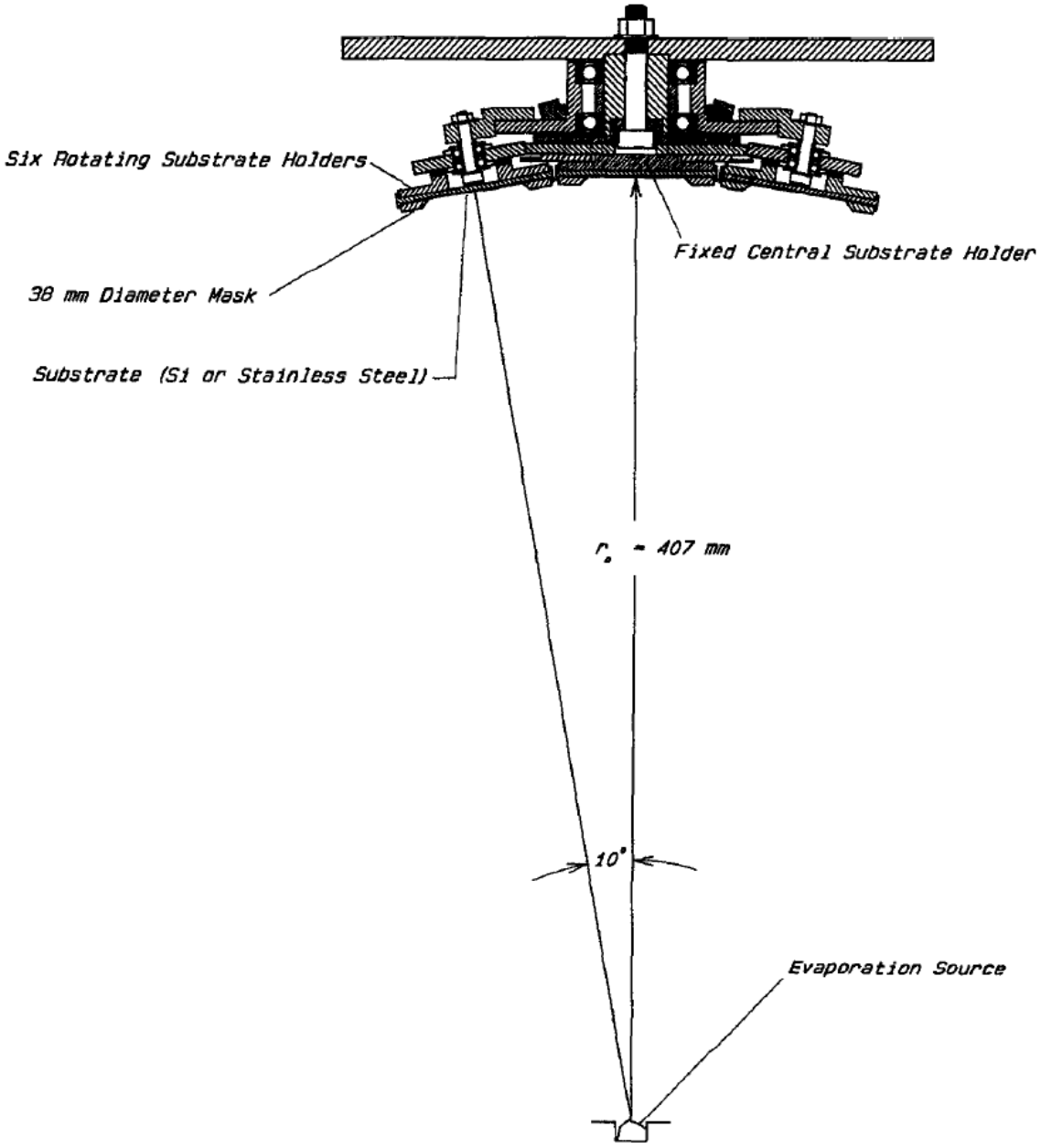


Figure 2.3: The evaporation rig used for the lifetime ^{6}Li deposit [Pauwels et al., 1995].

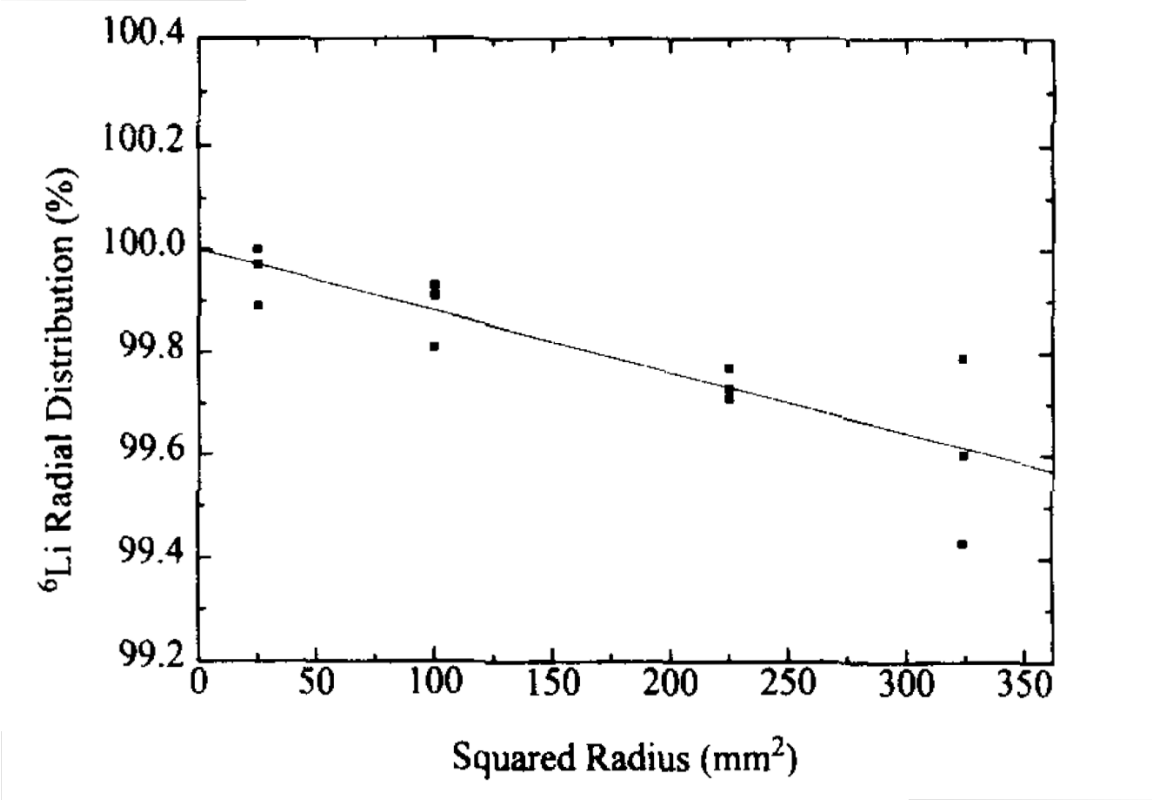


Figure 2.4: Measured (points) and calculated (line) deposit profile for the ^{6}LiF foils [Pauwels et al., 1995].

only quantity that goes into the lifetime that was not a first-principles measurement by the collaboration.

2.4 Assessment of Uncertainties

The experiment reports a value of $\tau_n = (886.3 \pm 1.2 \pm 3.2)$ s. The uncertainty budget for the experiment is given in table 2.2. The 1.2 s proton counting statistical uncertainty is not a fundamental limit of the experiment, but instead a chosen stopping point due to the larger uncertainty in the neutron counting efficiency. The top three sources of uncertainty are those used in determining the flux monitor efficiency. This 0.3 % uncertainty represents the likely state of the art of for determining the combination of detector solid angle, foil areal density, ^{6}Li thermal neutron cross section. Furthermore, because the ^{6}Li cross section is taken from evaluated nuclear data files and not a direct measurement of the cross section, there is some additional concern for this number. Since the publication of the lifetime paper, ENDF/B-VII has been released [Carlson et al., 2009]. Figure 2.5 shows the last three ENDF evaluations of the ^{6}Li thermal neutron cross section. The value of the cross section has almost moved outside of its own uncertainty in each of the last three evaluations. Because τ_n changes each time a new evaluation of σ_0 is released, it is desirable to move away from ENDF to a method that determines the flux monitor efficiency without referencing this cross section.

The limitations of this method were known during the planning stages of the lifetime experiment [Gilliam and Lamaze, 1986]. It was understood that a way forward was to perform a direct calibration of the neutron flux monitor efficiency. A calibration at the 0.1 % level or better paves the way for the experiment to run again towards the goal of a 0.1 % overall uncertainty, eliminates the most problematic source of uncertainty (the ^{6}Li thermal neutron cross section), and potentially allows for an immediate re-evaluation of the 2005 lifetime with reduced uncertainty. This thesis describes the first successful direct calibration of the neutron flux monitor efficiency.

Table 2.2: The beam lifetime experiment uncertainty budget [Nico et al., 2005b]. Items 1-3, 5, and 6 are uncertainties associated with the neutron flux determination.

Source of correction	Correction (s)	Uncertainty (s)
^{6}LiF deposit areal density		2.2
^{6}Li cross section		1.2
Neutron detector solid angle		1.0
Absorption of neutrons by ^{6}Li	+5.2	0.8
Neutron beam profile and detector solid angle	+1.3	0.1
Neutron beam profile and ^{6}Li deposit shape	-1.7	0.1
Neutron beam halo	-1.0	1.0
Absorption of neutrons by Si substrate	+1.2	0.1
Scattering of neutrons by Si substrate	-0.2	0.5
Trap nonlinearity	-5.3	0.8
Proton backscatter calculation		0.4
Neutron counting dead time	+0.1	0.1
Proton counting statistics		1.2
Neutron counting statistics		0.1
Total	-0.4	3.4

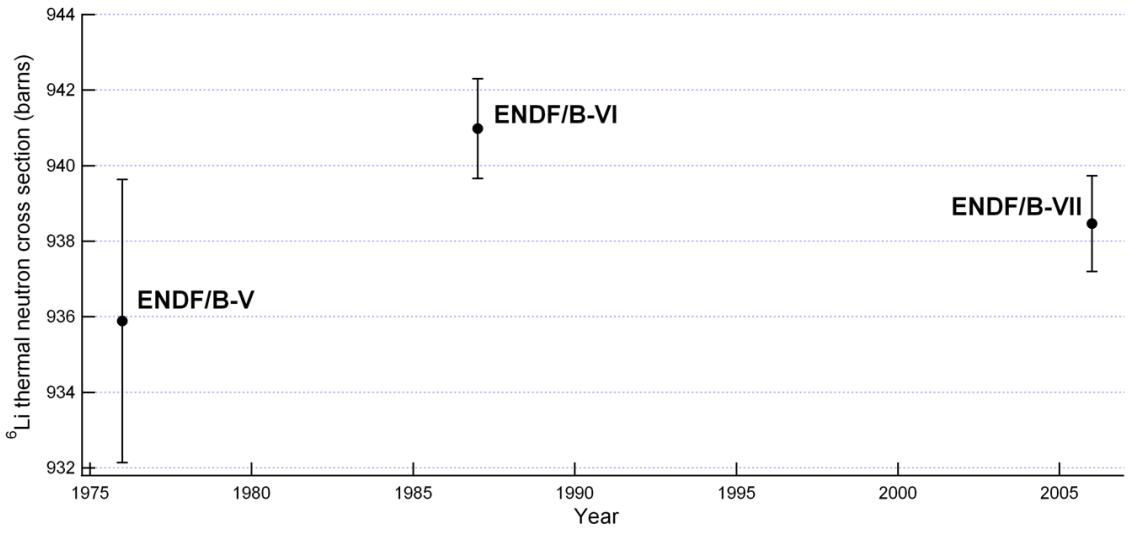


Figure 2.5: Lithium-6 thermal neutron cross section from the last three ENDF evaluations [Carlson and Bhat, 1982; Carlson et al., 1993, 2009].

Chapter 3

Direct Measurement of the Flux Monitor Efficiency

A direct measurement of the neutron flux monitor efficiency was planned as part of the original neutron lifetime measurement campaign at NIST. The goal was to perform a direct measurement to 0.1 %, which requires absolute determination of neutron flux to better than 0.1 %. Designing a device capable of sub-0.1 % absolute neutron rate measurements was an unprecedented challenge. Two techniques were developed with the hope that this would increase the chance of success, and, in the case of both succeeding, would provide much-needed confidence in a very difficult measurement. The neutron calorimeter technique measured the heat produced by neutron interactions in a target and inferred a flux. The Alpha-Gamma technique used a calibrated gamma detector to count the ^{10}B(n,γ) 478 keV reaction gamma rays from a completely absorbing target of ^{10}B.

Because the neutron flux monitor measures the capture flux of a beam, its efficiency is inherently dependent on the spectrum of the neutrons that impinge upon it. By using a monoenergetic (monochromatic) beam of neutrons, the flux monitor operates at one efficiency. The rate of detected alphas and tritons $r_{\alpha,t}$ in the neutron

flux monitor on a beam of wavelength λ is given by:

$$r_{\alpha,t} = \epsilon_0 \frac{\lambda}{\lambda_0} r_n \tag{3.1}$$

where ϵ_0 is the efficiency of the flux monitor at the thermal wavelength λ_0 and r_n is the incident neutron rate. With a measurement of the neutron rate and a measurement of the wavelength of the monochromatic beam, one can determine the efficiency of the flux monitor directly. To measure the efficiency of the neutron flux monitor to 0.1 %, it is necessary to measure both the neutron flux and wavelength of a monochromatic neutron beam to better than 0.1 %. This chapter discusses the techniques developed to measure cold and thermal neutron flux to better than 0.1 %. A discussion of the wavelength measurement is found in chapter four.

3.1 The Neutron Calorimeter

The neutron calorimeter (figure 3.1) operates as an absolute neutron detector by measuring the heat produced by neutrons absorbed in a cryogenic target [Chowdhuri et al., 2003]. The heat is measured by an instrument known as an electronic substitution radiometer, in which the heat of radiation can be compared to an equivalent amount of electrical power. The cryogenic target is coupled to a heatsink through a weak thermal link. The heatsink is kept at a constant temperature, and the power required to maintain the temperature is monitored. The heat generated by reaction products from the absorption of the neutron beam can then be determined from the difference in power required with the beam on and off.

The calorimeter target must be chosen carefully. The ideal target is composed of a material that is totally absorbing to neutrons and its reaction products contribute a known and large enough amount of heat to the bulk of the target. It is also critical that all the energy in neutron capture in the target material be carried by short range

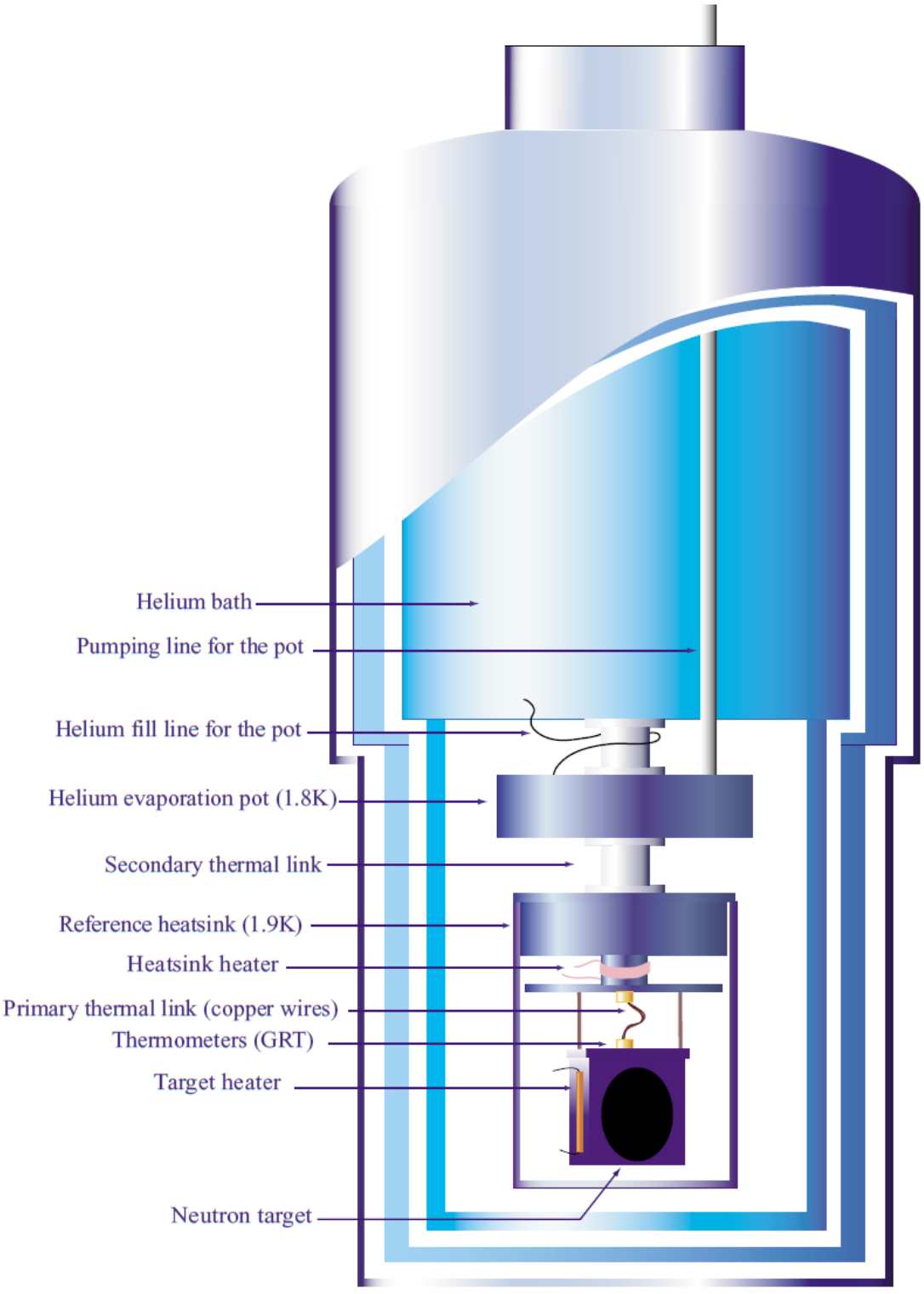


Figure 3.1: Schematic of the neutron calorimeter [Chowdhuri, 2000].

particles so that all reaction energy is deposited in the target. Two detector targets were envisioned in the original proposal - ^{3}He and ^{6}Li.

^{6}Li is a good candidate because of its large neutron absorption cross section, its high Q-value (4.78293 ± 0.00047 MeV), and its readily absorbed reaction products (no gamma-rays). However, a target of pure ^{6}Li is not feasible. At low temperatures ^{6}Li undergoes a first-order phase transition [Pearson, 1965]. The transition can be incomplete, allowing reaction heat to be lost to the phase transition. A transformation inhibiting material must be added to make a viable target. This material may introduce additional neutron absorption and scattering mechanisms to the target, and so it must be chosen carefully. Reaction energy can be stored in lattice defects in these ^{6}Li salts. Energy lost to this mechanism must come from calculations.

^{3}He has a significantly lower Q-value (0.763763 ± 0.000004 MeV) and a higher heat capacity, making it much more technically challenging to perform the power measurement. However, liquid ^{3}He is not subject to solid state effects that make the more accessible ^{6}Li-based measurements difficult to interpret. To date, three measurements have been attempted with the neutron calorimeter using both ^{6}Li-based solid targets and liquid ^{3}He.

3.1.1 First Run of the Neutron Calorimeter

The first run of the neutron calorimeter was performed in parallel with the first run of the Alpha-Gamma device on NG6 [Richardson, 1993]. The neutron flux monitor could not be calibrated in these runs, since the wavelength distribution of the polychromatic beam was only roughly known. Instead, a measurement of r_n was performed with both devices and the comparison hoped to show agreement between the two to bolster confidence in the techniques used.

For this measurement, the neutron calorimeter was run with two ^{6}LiPb targets at a temperature of 4.2 K. The first of the two targets was suspected to have regions of pure Pb, which lead to higher levels of neutron backscattering from the target. The

neutron calorimeter and Alpha-Gamma device were put in series on the beamline, and the measured r_n was compared. The neutron calorimeter was found to report $(1.6 \pm 0.3\,\%)$ fewer neutrons than the Alpha-Gamma device. It was concluded that this was unlikely to be a heat loss, but instead a neutron loss mechanism such as improperly determined neutron albedo.

3.1.2 Second Run of the Neutron Calorimeter

A number of significant improvements were made in the second run of the neutron calorimeter [Chowdhuri, 2000; Chowdhuri et al., 2003]. A monochromatic, lower flux beamline was constructed for the purpose of developing the detector and calibrating the two neutron flux monitors used in the neutron lifetime experiment that was taking place on NG6. The wavelength was measured by Bragg scattering with a perfect silicon crystal analyzer. A ^{6}LiMg target was used in addition to the two ^{6}LiPb targets from the previous measurement. The new target had the advantage of lower heat capacity (due to lower mass) and less neutron backscattering. By operating the calorimeter at 1.8 K instead of 4.2 K, the heat capacity of the target was reduced by a factor of eight. A careful assessment of neutron backscattering from both target types was performed with Dy foil irradiations (described in chapters four and six). It was determined that the backscattered fraction was roughly thirty times smaller with the new ^{6}LiMg target.

Sub-0.1 % measurements of the neutron flux monitor efficiency were established for two ^{6}LiF foils. However, there remained doubts about the absolute accuracy of the neutron calorimeter. It was found that r_n with the ^{6}LiMg target was $(1.71 \pm 0.06\,\%)$ higher than that measured by the ^{6}LiPb target. This is consistent with the difference between the ^{6}LiPb target and the Alpha-Gamma device, but a thorough accounting for the difference was never completed satisfactorily. Additionally, calculations showed that energy lost to the formation of defects in the target required a 0.1 % correction, but a corroborating measurement of this effect was not possible. Further

efforts to calibrate the neutron flux monitor would require a target not susceptible to these defects.

3.1.3 Third Run of the Neutron Calorimeter

The problem of defect formation in the solid targets was addressed by modifying the neutron calorimeter to operate with a liquid-^{3}He target [Hansen, 2004]. While the use of ^{3}He rid the experiment of pernicious solid-state effects, it added significant technical challenges. Because of the six-fold lower reaction Q-value and higher heat capacity of ^{3}He, the power measurement is more difficult. Also, there is considerable added challenge in simply operating a cryogenic liquid target. A 0.1 % measurement of the neutron flux monitor efficiency was attained, but the value differed by 4 % from the previous calorimeter measurement. It is believed that this measurement was in error due to heat leaks in the apparatus. However, great strides were made in improving the beam wavelength measurement. These improvements are detailed in chapter four.

3.2 The Alpha-Gamma Technique

The Alpha-Gamma technique [Gilliam et al., 1989] makes use of neutron absorption in a target of ^{10}B, which produces ^{7}Li and an α. The ^{7}Li nucleus is in an excited state 93.7 % of the time [Deruytter and Pelfer, 1967; Stelts et al., 1979] and will rapidly ($\tau = 73$ fs) de-excite by emission of a 478 keV gamma ray. This can be thought of as two separate reactions - an alpha-only reaction:

$$\mathrm{n} + {}^{10}\mathrm{B} \rightarrow {}^{7}\mathrm{Li}(1015\mathrm{keV}) + \alpha(1776\mathrm{keV})$$

and an alpha + gamma reaction (branching ratio $b_\gamma = 93.7\%$):

$$\begin{aligned} \mathrm{n} + {}^{10}\mathrm{B} &\rightarrow {}^{7}\mathrm{Li}^{*} + \alpha(1472\mathrm{keV}) \\ &\downarrow \\ &{}^{7}\mathrm{Li}(840\mathrm{keV}) + \gamma(478\ \mathrm{keV}) \end{aligned}$$

In the alpha + gamma reaction, the ^{7}Li nucleus recoils with a velocity parameter $\beta = 0.016$, which leads to a gamma-ray distribution anisotropy. This anisotropy must be accounted for in the alpha-gamma coincidence method because it perturbs the coincidence rate. For the α-source technique, the anisotropy is irrelevant.

The Alpha-Gamma (AG) device uses a totally absorbing target of enriched $^{10}B_4C$ to stop a beam of cold neutrons. Because the ^{10}B cross section for cold is very high (10580 barns for 5 Å neutrons), only a thin (0.32 mm) target of enriched ^{10}B is needed to stop all but a negligible portion of the beam. The incident neutron rate is determined by measuring the rate of reaction gammas in a calibrated gamma detector.

Alphas from the n+^{10}B reaction can scatter off boron atoms, and for this thickness of target, the observed alpha spectrum suffers significant distortion. Because of this, alpha counting from the fully absorbing target cannot be used to determine the neutron flux. Instead, the gamma rays are used as they can escape with minimal interaction in the thick target. However, the same properties make the gamma rays difficult to detect with high efficiency. High purity germanium (HPGe) gamma detectors are used in this experiment for their excellent resolution of the 478 keV signal peak, but this comes at a cost of low (and difficult to quantify) efficiency.

The detection geometry and coordinate system for the Alpha-Gamma device is shown in figure 3.2. The Alpha-Gamma device is centered around an interchangeable target foil at the origin which faces the (1,-1,1) direction. The foil is viewed face-on by a charged particle detector and from above and below by an HPGe detector. A

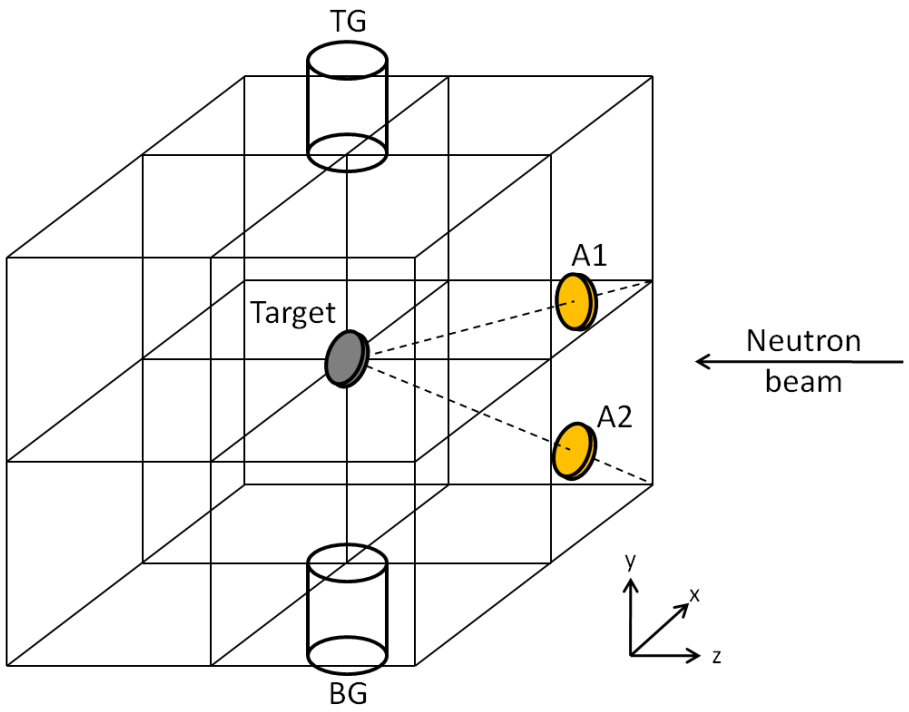


Figure 3.2: Detection geometry for the Alpha-Gamma device (not to scale)

second charged particle detector can view the foil from the (1,0,1) direction. When the completely absorbing ^{10}B foil is in the device, the neutron flux incident on the foil can be determined from the observed gamma rate and the gamma detection efficiency:

$$r_n = \frac{r_\gamma}{\epsilon_\gamma} \tag{3.2}$$

The efficiency of an HPGe gamma detector is dependent on the geometry of the germanium crystal. The Ortec detectors used in this experiment use a beveled cylindrical crystal with a central bore. The dimensions of these crystals vary from one detector to another. Their detection efficiency can be determined by very precise measurements of the crystal dimensions and the detection geometry. Calibrations of this type have been performed at the 0.1 % level [Hardy et al., 2002]. The Alpha-Gamma detection geometry is not conducive to this type of measurement, so other calibration techniques have been developed. The calibration process establishes the

efficiency of the two gamma detectors per neutron absorbed by the ^{10}B foil. This process can be completed in two ways - an alpha-gamma coincidence method or by transfer calibration with an α source.

Coincidence counting (typically alpha-beta and beta-gamma) methods have a long and successful history in nuclear physics. The alpha-gamma coincidence method makes use of the $(n, \alpha + \gamma)$ reaction from a thin ($\sim$ 25μg/cm^2) foil of ^{10}B. A neutron beam impinges upon the target, the reaction products are detected in the HPGe detectors and the A1 charged particle detector, and the coincidence events are recorded. Let R be the rate of neutrons absorbed in the thin foil. Then the detected alpha particle rate r_α is given by

$$r_\alpha = \epsilon_\alpha R \tag{3.3}$$

where ϵ_α is the efficiency of the alpha detector. Similarly, if we take ϵ_γ to be the efficiency of the gamma detectors, the detected gamma rate r_γ is given by

$$r_\gamma = b_\gamma \epsilon_\gamma R \tag{3.4}$$

where b_γ is the gamma branching ratio. If ϵ_α and ϵ_γ can be taken to be independent probabilities (which is true when detector A1 is used), then the coincidence rate $r_{\alpha\gamma}$ is given by:

$$r_{\alpha\gamma} = b_\gamma \epsilon_\alpha \epsilon_\gamma R \tag{3.5}$$

By combining equations 3.3, 3.4, and 3.5, we can express R in terms of the counting rates:

$$R = \frac{r_\alpha r_\gamma}{r_{\alpha\gamma}} \tag{3.6}$$

Substituting in for R in equation 3.4, we have:

$$r_\gamma = \epsilon_\gamma b_\gamma \frac{r_\alpha r_\gamma}{r_{\alpha\gamma}} \tag{3.7}$$

and thus

$$\epsilon_\gamma = \frac{r_{\alpha\gamma}}{r_\alpha b_\gamma} \tag{3.8}$$

R is given by the incident neutron rate (r_n) times the ^{10}B cross section (σ) and the areal number density of the ^{10}B foil (ρ_N):

$$R = r_n \sigma \rho_N \tag{3.9}$$

and the coincidence rate is then

$$r_{\alpha\gamma} = b_\gamma \epsilon_\alpha \epsilon_\gamma r_n \sigma \rho_N \tag{3.10}$$

In our setup, $\rho_N \approx 1.4\times10^{18}$ atoms/cm^2 ($\rho \approx 25\mu$g/cm^2), $\epsilon_\alpha \approx 7\times10^{-3}$, $\epsilon_\gamma \approx 4\times10^{-3}$, $\sigma = 10580$ b, and $r_n \approx 3.5 \times 10^5$/s at ~ 5Å for our typical beam size. This leads to an expected coincidence rate of $\sim 10^{-1}$ s^{-1}, which would require several months of running to achieve 0.1 % statistical precision. The coincidence method is better suited for beams approximately an order of magnitude more intense, where the coincidence rate is more manageable, yet the singles rates do not require large pile-up and dead time corrections. In this work, the α source method is used. By using a calibrated α source and the (n,$\alpha+\gamma$) reaction from a thin ^{10}B foil, we can transfer the calibration of the α source to the gamma detector pair.

A ^{239}Pu α source is measured in a low-solid angle counting stack whose solid angle is known to better than 0.05 %. From the known solid angle Ω_{stack} and the measured α rate r_α(stack), the 4π disintegration rate of the source is determined:

$$R_\alpha(\text{Pu}) = \frac{r_\alpha(\text{stack})}{\Omega_\alpha(\text{stack})} \tag{3.11}$$

The ^{239}Pu source is then loaded into the Alpha-Gamma vacuum can, and the α rate is measured in the A2 charged particle detector (r_α(Pu)). The efficiency of this detector

(ϵ_α) is given by the observed alpha rate over the known total alpha rate:

$$\epsilon_\alpha = \frac{r_\alpha(\mathrm{Pu})}{R_\alpha(\mathrm{Pu})} \tag{3.12}$$

A thin ^{10}B foil replaces the ^{239}Pu in the vacuum can, and the neutron beam is turned on. The observed alpha rate and the known detector efficiency determine the neutron absorption rate R in the deposit:

$$R = \frac{r_\alpha}{\epsilon_\alpha} = r_\alpha \frac{R_\alpha(\mathrm{Pu})}{r_\alpha(\mathrm{Pu})} \tag{3.13}$$

Note that this relies on the assumption that the efficiency of the alpha detector is the same for the ~ 5 MeV alphas from ^{239}Pu and the ~ 2 MeV alphas from ^{10}B(n,α). Any deviation from identical efficiencies would enter equation 3.13 as a ratio of the effects at each energy. Thus, small effects such as backscattered alphas from the detector surface enter as the ratio of losses at 2 and 5 MeV. SRIM [Ziegler, 2008] calculations show that backscattering is negligible at the level of 0.01 % for both 2 MeV and 5 MeV alpha particles and thus can safely be ignored. Because the both sources are very thin ($\sim$ 100 nm thickness), no significant alpha loss or scatter occurs within the material.

The observed gamma rate is given by:

$$r_\gamma(\mathrm{thin}) = \epsilon_\gamma b_\gamma R \tag{3.14}$$

and therefore the gamma detector efficiency can be determined:

$$\epsilon_\gamma = \frac{r_\gamma(\mathrm{thin})}{b_\gamma} \frac{r_\alpha(\mathrm{Pu})}{r_\alpha} \frac{1}{R_\alpha(\mathrm{Pu})} \tag{3.15}$$

Prior to the work detailed in this thesis, the two Alpha-Gamma techniques (coincidence method and α source method) have been used once in a proof-of-concept prototype and once with the current Alpha-Gamma device.

3.2.1 Alpha-Gamma Prototype

The groundwork for the Alpha-Gamma technique was developed at NIST in the late 1980s. The prototype apparatus was composed of a single charged particle detector and a single HPGe detector [Lamaze et al., 1988]. The apparatus was run on BT-7, a thermal neutron beam in the confinement building of the NBS Research Reactor (now known as the NIST Center for Neutron Research). A flux of $\sim 3 \times 10^7$ n/cm^2 was incident on a ^{10}B foil backed by stainless steel. The coincidence method achieved a statistical uncertainty of 0.4 % in approximately 24 hours of beam time. The α source method was performed with calibrated deposits of ^{237}Np and ^{239}Pu, with a final uncertainty in the determined gamma detector efficiency of 0.8 %. Corrections of ~ 1 % to the gamma detector efficiency had to be made for "accidental" coincidences and gamma attenuation in the foil backing.

3.2.2 First Run of the Alpha-Gamma Device

The shortcomings of the prototype apparatus were understood during the undertaking of the experiment and were outlined in the paper summarizing the results. The mark II apparatus was constructed in 1989, this time with two HPGe detectors and two charged particle detectors. The detection geometry was chosen to minimize the effect of beam and foil position shifts on the efficiency of the detectors. The geometry was also chosen to minimize the alpha-gamma coincidence rate perturbation from the recoil of the ^{7}Li nucleus.

The first run of the Alpha-Gamma device [Richardson, 1993] was also the first for beamline NG6 in the CNRF (Cold Neutron Research Facility, now NCNR) cold neutron guide call. NG6 is a polychromatic beam, so calibration of the neutron flux monitor was not possible for this run. Instead, a measurement of ϵ_γ and r_n were performed using both the alpha-gamma coincidence and alpha source methods. The high flux of the polychromatic beam led to very high singles rates, and large (1 - 10 %) dead time corrections were required. This necessarily led to running the apparatus

at smaller collimations, which led to the coincidence method being statistics-limited. The alpha source method was hampered by material loss from the two ^{239}Pu sources used. Still, the resulting ϵ_γ measurements differed by only $(0.30 \pm 0.28\,\%)$.

Additional complications enter when the thick target was used to measure r_n. The thick target used in this experiment was a 1.8 mm thick slab of natural boron nitride. Because of the $\sim$20 % abundance of ^{10}B in natural boron, neutrons penetrate into the material before being absorbed. This meant that gamma rays born in the target had to travel appreciable distances in the material before reaching the HPGe detectors. Gamma rays scatter off the target material, leading to a $\sim$5 % correction for lost gamma rays reaching the top detector and $\sim$0.2 % for the bottom. Additionally, this attenuation was not measured. There was only one thick target, so a measurement of gamma rate versus target thickness (and hence, attenuation per unit thickness) could not be made.

3.2.3 Second Run of the Alpha-Gamma

The work in this thesis represents the second run with the Alpha-Gamma device and the first to operate it simultaneously with the lifetime neutron flux monitor on a monochromatic neutron beam. It is also the first measurement performed on NG6m since the installation of a new monochromator. A number of significant improvements have been made since the last Alpha-Gamma run.

Since the first run of the Alpha-Gamma device, it was determined that detector A2 was not facing the target foil directly. While not necessarily a problem, having the detector positioned properly minimizes the effects of target or beam movement on its solid angle. Modifications to the vacuum can were made to fix the detector position. New HPGe detectors were purchased, and the A2 charged particle detector was upgraded to a passivated implanted planar silicon (PIPS) detector. The data acquisition code was improved and a digital, four channel multi-channel analyzer has been added. Two enriched $^{10}B_4C$ targets (0.32 and 0.565 mm thick) were

obtained after the first Alpha-Gamma run. These thinner targets attenuate ∼1-2 % of gamma rays passing through. This effect is still one of the largest corrections in the experiment, but it is experimentally determined to sub-0.1 % precision. Because there are two targets, a precision measurement of the attenuation can be peformed with each target and with the pair together. A dedicated Si foil holder has been made to perform a measurement of the Si backscattering enhancement in the ^{6}Li foil. It is also used to measure the gamma ray attenuation in the Si backing of the thin ^{10}B target. Another significant improvement to the apparatus is the ability to perform the wavelength measurement periodically without disturbing the calibration setup. This new wavelength measuring setup is described in section 4.4.

Chapter 4

Characterizing the Beamline

Performing a calibration of the neutron flux monitor with the Alpha-Gamma device imposes several constraints on any candidate beamline. The calibration must be performed for neutrons of a particular velocity, so a beam of monochromatic neutrons is required. The neutron flux monitor has a very low detection efficiency ($\sim 8 \times 10^{-5}$ for 5 Å neutrons), so the combination of neutron flux and beam size must be adequate to achieve the desired statistical uncertainty. The beam size must be small enough that the entire spot is incident on the target foils in the Alpha-Gamma. In the thin target running configuration, the flux should be high enough to achieve the desired statistical uncertainty in the gamma counting, yet the same configuration must not produce excessive pile-up when the thick target is used in the neutron rate measurement. These constraints are satisfied by careful alignment of the apparatus and characterization of monochromatic beamline NG6m at the NCNR.

4.1 The NIST Center for Neutron Research

The measurements described in this dissertationstook place at the NCNR. The NCNR is a user facility providing neutron measurement capabilities to researchers in academia, industry, and government [Cappelletti et al., 2001].

The heart of the NCNR is a 20 MW D_2O-moderated research reactor pictured in figure 4.1. Fast neutrons from the nuclear fission of ^{235}U are thermalized to room temperature by the surrounding D_2O. The fuel elements reside above and below the neutron ports, which greatly reduces line-of-sight gamma rays reaching the experiments at only a slight cost in neutron flux. The peak thermal neutron flux at the core is approximately 4×10^{14} /cm^2/s.

The reactor has 9 beamlines in the confinement building that make direct use of the high flux of thermal neutrons. However, a number of experiments are best served by sub-thermal neutrons. To accomodate this need, a section of this space houses a liquid hydrogen moderator where thermal neutrons are moderated by elastic scattering. These elastic collisions tend to reduce neutron energy quickly (taking only a few bounces to approach the desired temperature), but energetic hydrogen nuclei can also give up their energy to a neutron. The approximately Maxwellian distribution that describes the outgoing neutrons has a characteristic temperature of about 38 K [Williams, 2007]. These neutrons have the proper energy to be efficiently transported tens of meters from the source by neutron guides. This is made possible by careful choice of guide material. The nuclear potential V the neutron experiences at the material boundary of the guides is given by:

$$V = \frac{2\pi\hbar^2\rho_N a}{m_\mathrm{n}} \tag{4.1}$$

where ρ_N and a are the number density and the scattering length of the nuclei that make up the material boundary. A neutron will reflect from the guide if the neutron's wavevector normal to the guide surface satisfies

$$V > \frac{\hbar^2 k_\perp^2}{2m_n} \tag{4.2}$$

If we define θ as seen in figure 4.2, the normal wavevector as is given by:

$$k_\perp = k\sin\theta \tag{4.3}$$

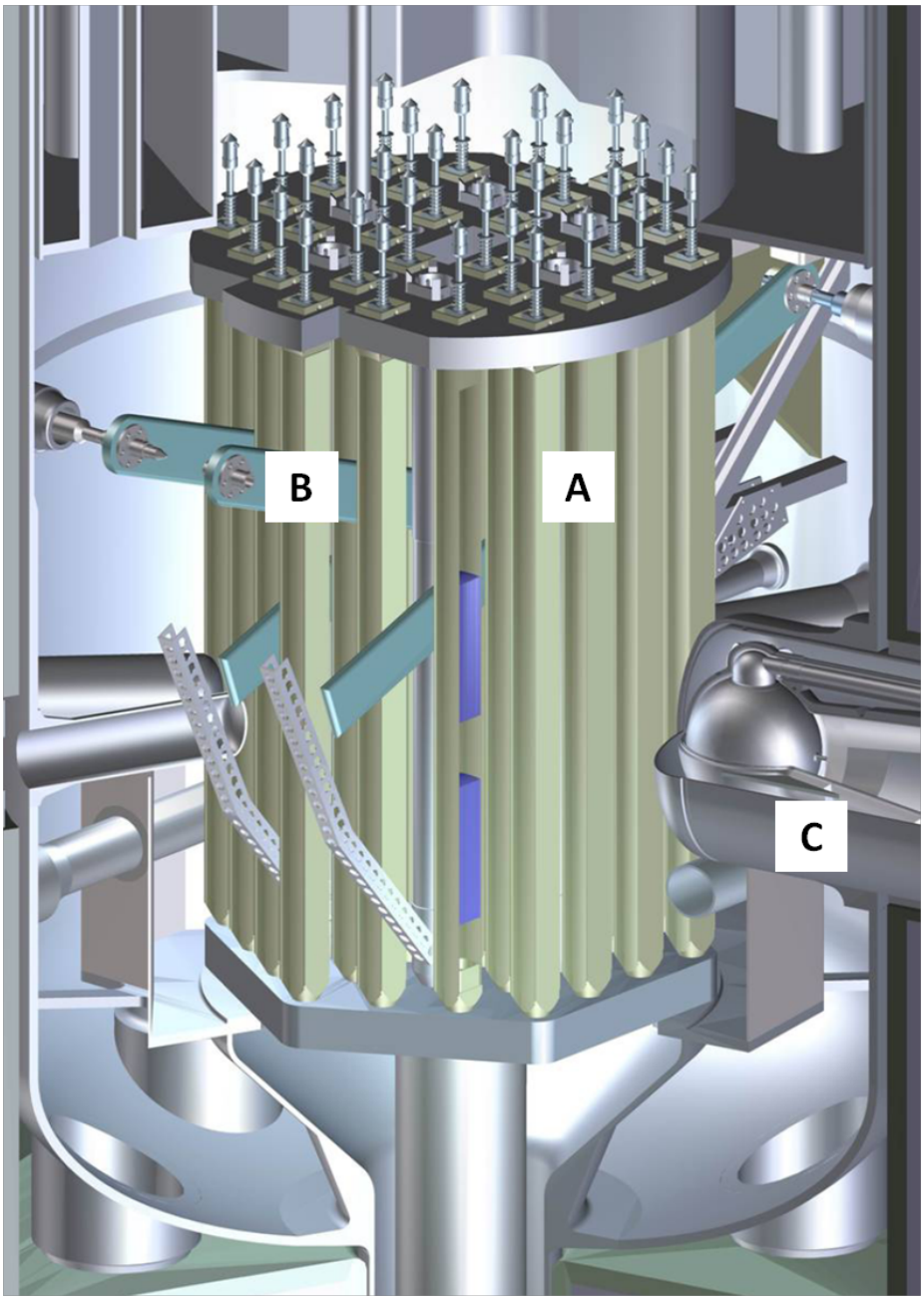


Figure 4.1: Schematic of the reactor core. Neutrons are produced in ^{235}U fuel rods (A) and cadmium shim-arms (B) serve as control rods. A vessel filled with 20 K liquid hydrogen (C) is the source for cold and thermal neutrons for the guide hall [Williams, 2007].

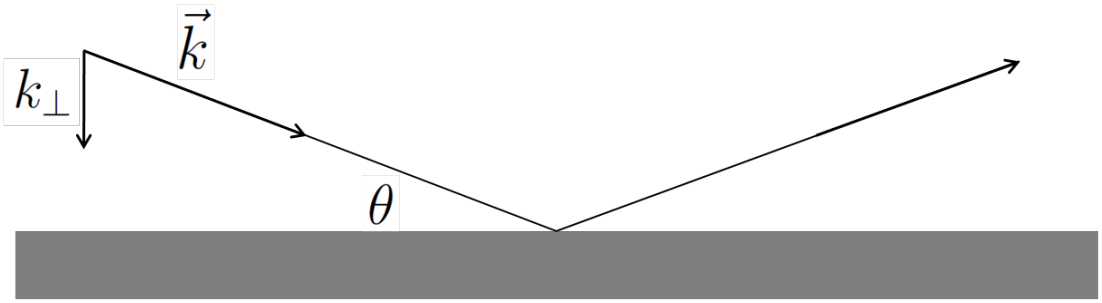


Figure 4.2: A neutron incident on a material boundary.

A critical angle θ_{crit} for total reflection arises when we turn equation 4.2 into an equality:

$$(k \sin \theta_{\text{crit}})^2 = 4\pi\rho_N a \tag{4.4}$$

which, along with an expression for the wave vector in terms of wavelength, leads to an expression for the critical angle in terms of the material number density and bound coherent scattering length:

$$\sin \theta_{\text{crit}} = \lambda\sqrt{\frac{\rho_N a}{\pi}} \tag{4.5}$$

The guides at the NCNR are rectangular tubes made from ^{58}Ni-coated, optically flat borated glass. ^{58}Ni has a neutron scattering length $a = 14.4 \times 10^{-13}$cm, giving it one of the better neutron reflective potentials.

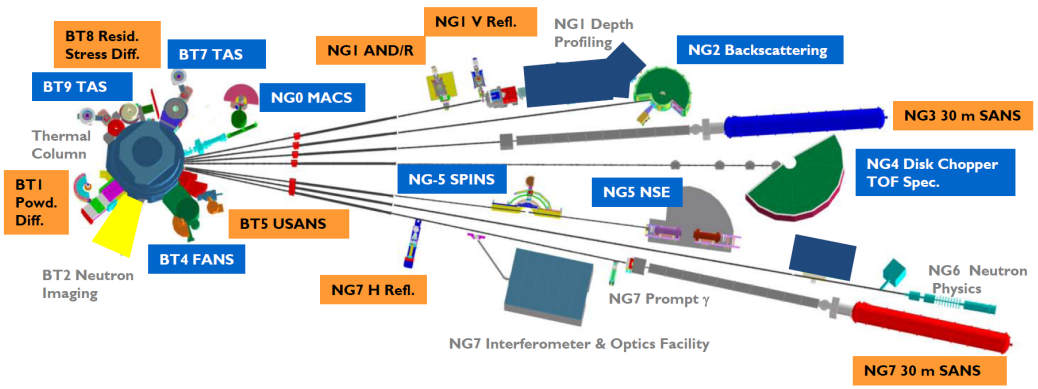


Figure 4.3: The NIST Center for Neutron Research confinement building and guide hall [Dimeo, 2009].

In additional to being efficient transporters of cold and thermal neutrons, the neutron guides allow experiments to be located tens of meters from the reactor core. This has a significant impact on the ambient gamma backgrounds, which is beneficial for the experiments making use of gamma-sensitive detectors and serves to keep the radiation dose to personnel minimal. Gamma backgrounds in the end station beams can be further mitigated with single crystal bismuth filters.

The instruments in the NCNR confinement building and guide hall are shown in figure 4.3. The primary users of the facility are material scientists and condensed matter physicists, but one cold beamline (NG6) is dedicated to the study of fundamental neutron physics [Nico et al., 2005a]. NG6 has three reflected beamlines and an end station. The end station provides a high-flux, broad spectrum of cold neutrons from the liquid hydrogen moderator. The polychromatic beam impinges on three monochromators upstream of the end station, Bragg reflecting out three monoenergetic beamlines for specialized use. They are NG6a (3.8 Å), NG6m (5 Å), and NG6u (8.9 Å). The calibration technique used on the neutron flux monitor requires a monoenergetic beam of neutrons. NG6m was used for this measurement.

4.2 NG6m

NG6m is generated by Bragg reflection of the broad spectrum of neutrons from NG6. Neutrons of approximately 5 Å Bragg reflect off a pyrolytic graphite (PG) monochromator. The orientation of the graphite crystalites is not perfect - a deliberate "mosaic" spread allows for better acceptance of neutrons near the nominal Bragg wavelength at the expense of accepting a broader range of neutron energies.

The original PG monochromator was lost to an upstream guide implosion in 2005. A large shard of guide glass struck the NG6m monochromator and caused irreparable damage. All previous calibrations of the neutron flux monitor and beam wavelength measurements were performed with this monochromator. As such, the

characterization detailed in section 4.4 is the first precision assessment of the new NG6m beam properties.

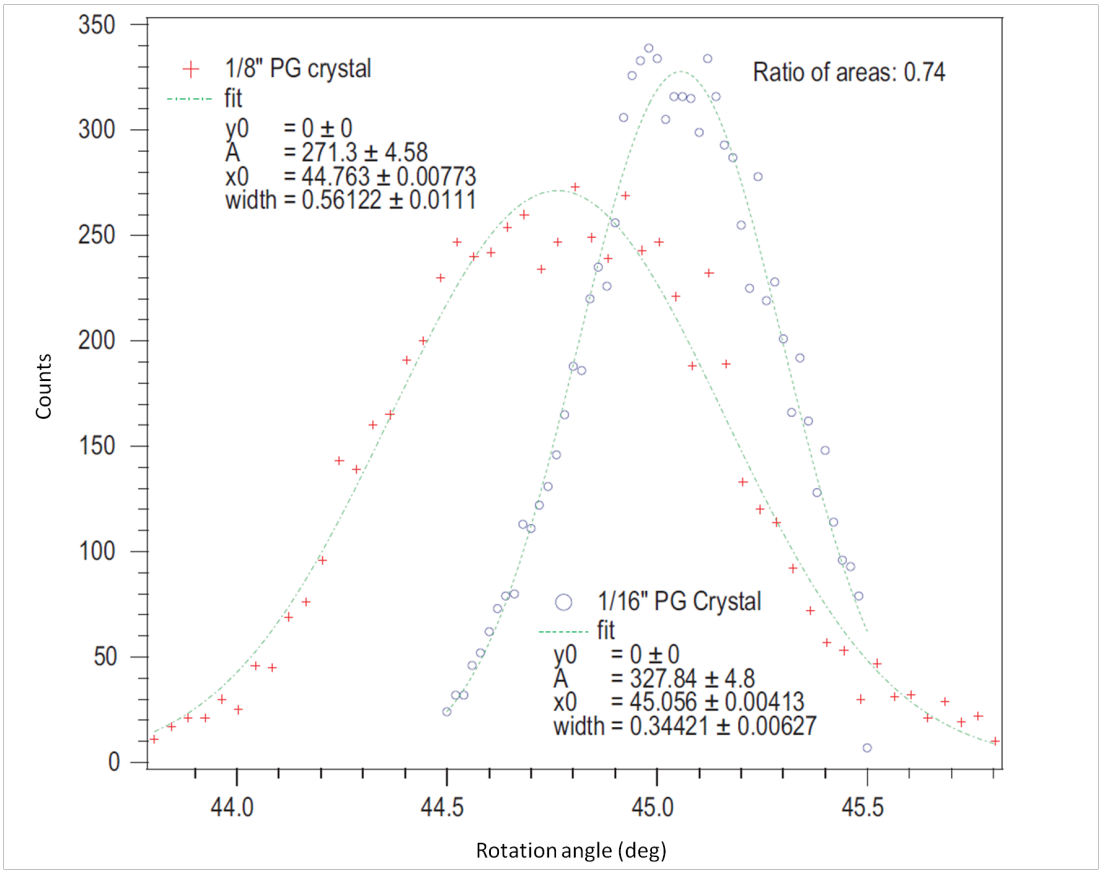


Figure 4.4: Reflectivity and rocking curves for the two candidate monochromators [Mumm, 2005].

Two candidate monochromators were tested on the NG1 neutron reflectometer. The reflectivity and rocking curve width were measured (figure 4.4). From these data, a beam simulation was performed and it was determined that the thin crystal could deliver roughly 40 % more flux, and do so in a narrower wavelength band. The thin crystal was installed in 2005 and the beamline was reconstructed [Mumm, 2005]. Installation of the Alpha-Gamma experiment began in 2006.

4.3 Aligning and Imaging the Beam

It is critical that all parts of the neutron beam incident on the flux monitor target continue on to impinge upon the Alpha-Gamma target. The most stringent limits on the beam diameter are set in the thin ^{10}B configuration, where the Alpha-Gamma target is a 38 mm circle. Because the target faces the (1,-1,1) direction and the incident beam travels along the z-axis (figure 3.2), a circular beam incident on the target has a pronounced elliptical shape (seen in figure 4.5). Thus, our beam diameter must be much smaller than the 38 mm target. This leads us towards smaller beam collimations but comes at a price of decreased neutron rate and hence longer running time to achieve the desired statistical precision. To optimize the balance, careful alignment and imaging of the beam is essential.

Alignment of the beam is performed with a theodolite. The theodolite sits on a heavy tripod stand with height adjustment and a horizontal translation stage. The theodolite mounts to the tripod by means of a tribrach, which sets the plane of horizontal rotation for the device. A series of three spirit levels on the tribrach give an approximate leveling of the device with respect to gravity. In practice, the vertical viewing angle is set to 90°, and a beam height marker is sighted. The tribrach is then adjusted to level the theodolite. A planar bubble level allows the user to achieve good leveling using the tribrach thumbscrews without iteration. For more precise leveling, a typical spirit level is leveled along the direction of two of the tribrach thumbscrews, and then again perpendicular to those two by the third tribrach thumbscrew. Once the device is leveled, fine adjustment of the height is performed and the sighting of the beamline markers can continue.

Figure 4.6 demonstrates the nonuniformity of the beam intensity across the surface of the monochromator. This is a concern for choosing a beam height, but is largely irrelevant for beam direction. The beam direction is set by a series of five floor markers. All five markers cannot be used simultaneously - markers three and four do not fall on the line set by markers one, two, and five. In practice, a preliminary line

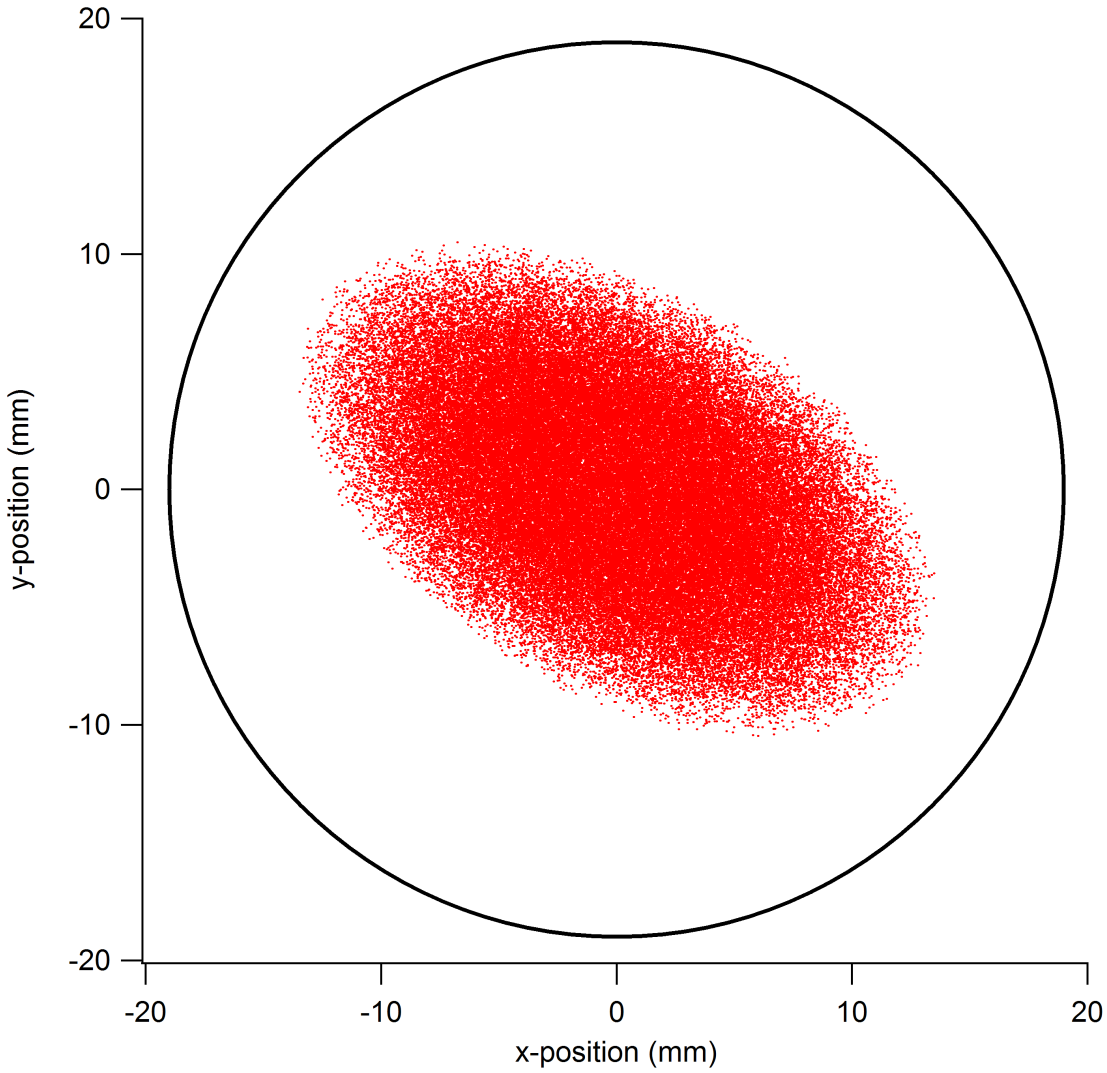


Figure 4.5: A simulation of the beam spot on the Alpha-Gamma target foil with a 15mm upstream collimator and an 8.38mm downstream collimator. The black circle represents the active area of the thin target.

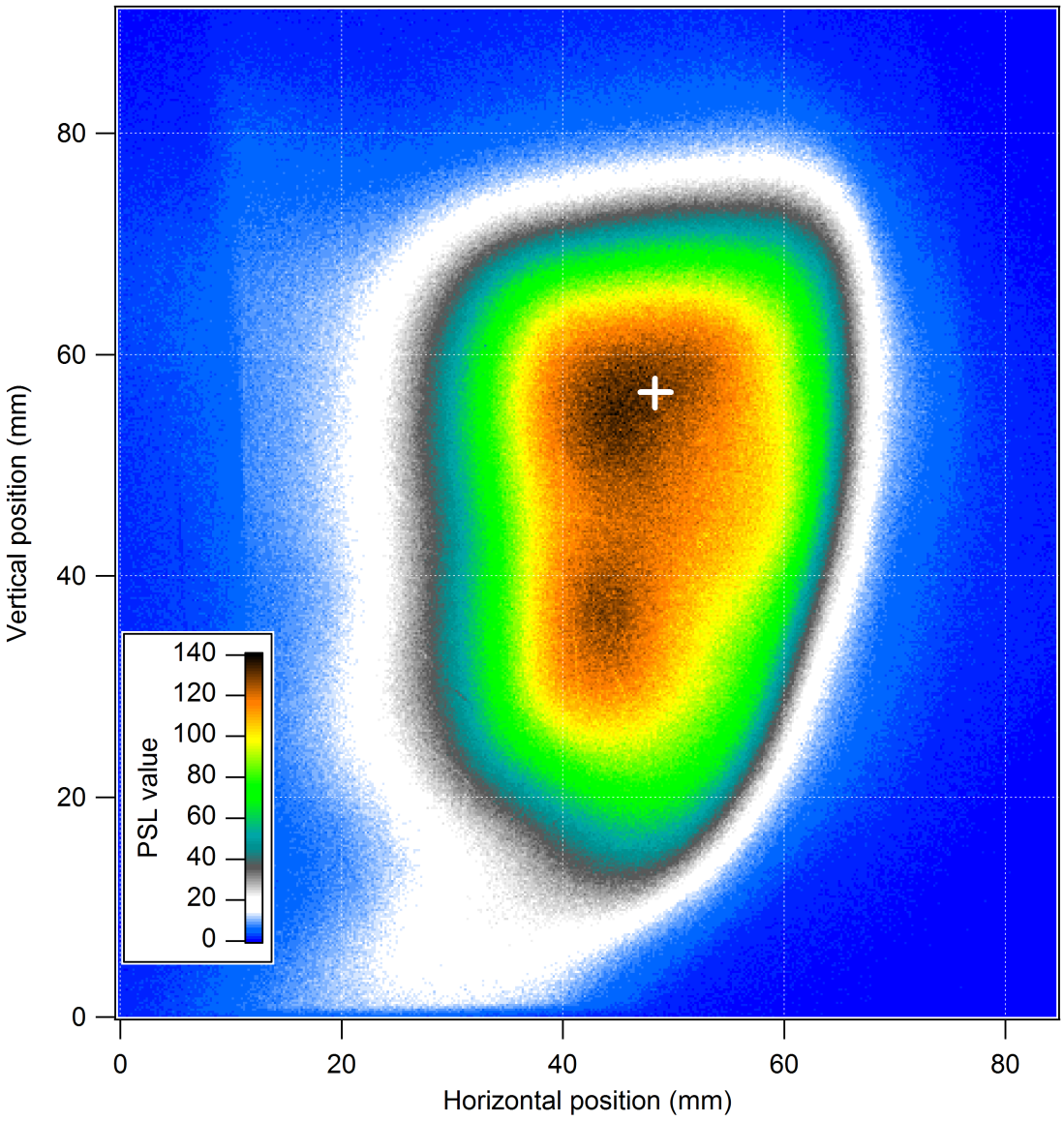


Figure 4.6: FujiBAS neutron imaging plate image of the NG6m beam at the shutter exit and approximate sighted center.

is set up by sighting markers one and two on a line, then tuning between markers one and five.

Imaging of the beam is accomplished by irradiation of a FujiFilm BAS imaging plate (commonly referred to as a Fuji plate). These plates make use of special photo-stimulable phosphor that releases stored energy upon exposure to visible light. Incident radiation on the phosphor induces electron excitation which, by virtue of the phosphor material, is trapped in color centers. Visible laser light is then used to extract this dislocating energy. The measured photo-stimulable luminescence (PSL) is directly proportional to the intensity of the incident radiation over a wide dynamic range. The resulting image can have pixel resolution down to 50×50 μm^2.

These image plates are not directly sensitive to neutrons and thus require an intermediate neutron-sensitive target. The Neutron Interactions and Dosimetry (NI&D) group owns a composite Fuji plate with a built-in neutron reactive layer, which eliminates the need for a transfer exposure. However, for highly position sensitive imaging, use of a more rigid, precise intermediate irradiation target is desirable. Natural dysprosium metal is a good choice. Roughly 20 % of natural dysprosium is ^{164}Dy, which is highly absorbing to neutrons (7800 b at 5 Å), and the subsequent beta decay of ^{165}Dy has an appropriate half-life (2.3 h). It is affordable, inert, and can be machined to the desired shape. The irradiated Dy foil is then placed on the surface of a normal Fuji plate to make the image. Imaging of the beam upstream of the the two apparatus was performed by irradiating a direct image plate and imaging of the beam inside the Alpha-Gamma device and the neutron flux monitor was done by dysprosium irradiation.

The other tunable parameter was the tilt of the PG monochromator. Changing the tilt alters the up-down direction of the beam. Ideally, the beam would run directly along the sighted line with no up-down component. Measuring the beam tilt was done by imaging the beam at several downstream positions with a 35 mm upstream collimator and no downstream collimator. Images taken after initial commissioning of the beam revealed that the center of intensity trended upwards the

further downstream the image location. The direct image plate was used for this measurement. A double exposure technique was used to image the beam spot and then image the center and orientation of the image. A borated aluminum (BorAl) plate with four 1 mm holes in an "L" shape was placed just upstream of the image plate and was aligned to the beam center by a theodolite. The BorAl plate is highly absorbing for neutrons, so only the "L" hole pattern was exposed to the existing image providing the beam center and image orientation. Fits to the center of the intensity of the beam image were performed and could be compared to the sighted beamline.

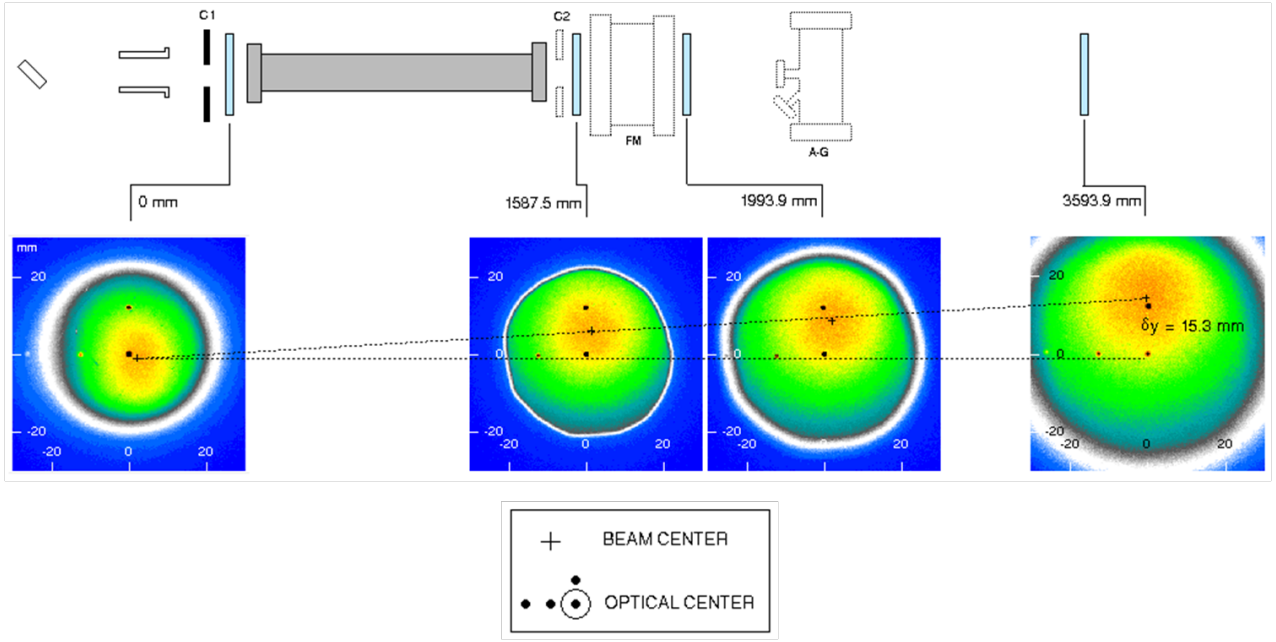


Figure 4.7: Measurement of the beam tilt on NG6m using a neutron-sensitive FujiBAS image plate.

Table 4.1: Collimations used in the Alpha-Gamma experiment.

Configuration name	C1 diameter (mm)	C2 diameter (mm)
15/7	15	7.2
15/8	15	8.38
15/10	15	10.5

Fitting these centers versus downstream distance to a line worked well, and the resulting slope showed that the beam was tilted up by approximately 0.25° with respected to the sighted beamline. The images are shown in figure 4.7. It was clear that we needed to remove the tilt to better insure that we would not lose neutrons in-between the two apparatus. The crystal has a motorized tilt and rotation stage and the cables for performing these rotations were readily accessible outside of the shielding. To correct a tilt of 0.25° the monochromator needed to be tilted down 0.125°. This was accomplished with a Parker Zeta 6104 motor controller. After the tilt was complete, another series of images was taken, and it was verified that the tilt had been removed. A small residual downward tilt of 0.06° remains, but was considered too small to be of concern.

Beam images were also taken to investigate the possibility of a beam halo. Any neutrons that pass through the flux monitor target foil but not the Alpha-Gamma target result in a systematic underassessment of the neutron flux. Beam images were perfomed at the Alpha-Gamma target foil location to search for a beam halo. Neutron and film exposure times varied with collimation choice (flux) but were on the order of minutes. For our typical calibration collimations (table 4.1), the beam was turned on for 15 minutes and the Dy foil was exposed to the image plate for 15 minutes.

Images of the beam in the three collimation configurations are found in figure 4.9. The circles surrounding the images represent the active region of the thin target. Any neutrons outside this region will not interact with the thin ^{10}B deposit. Assessing this fraction is challenging for a number of reasons. The final image suffers from noise, which must be assessed by averaging a representative region of the image and finding

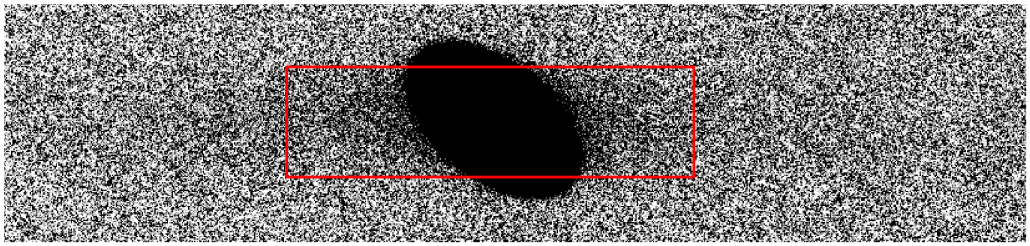


Figure 4.8: The "galaxy" effect - imaging artifacts appear as the plate reader scans through areas of high intensity. A red box shows the approximate extent of the "galaxy." The image is displayed in a small PSL-range greyscale to better display the effect.

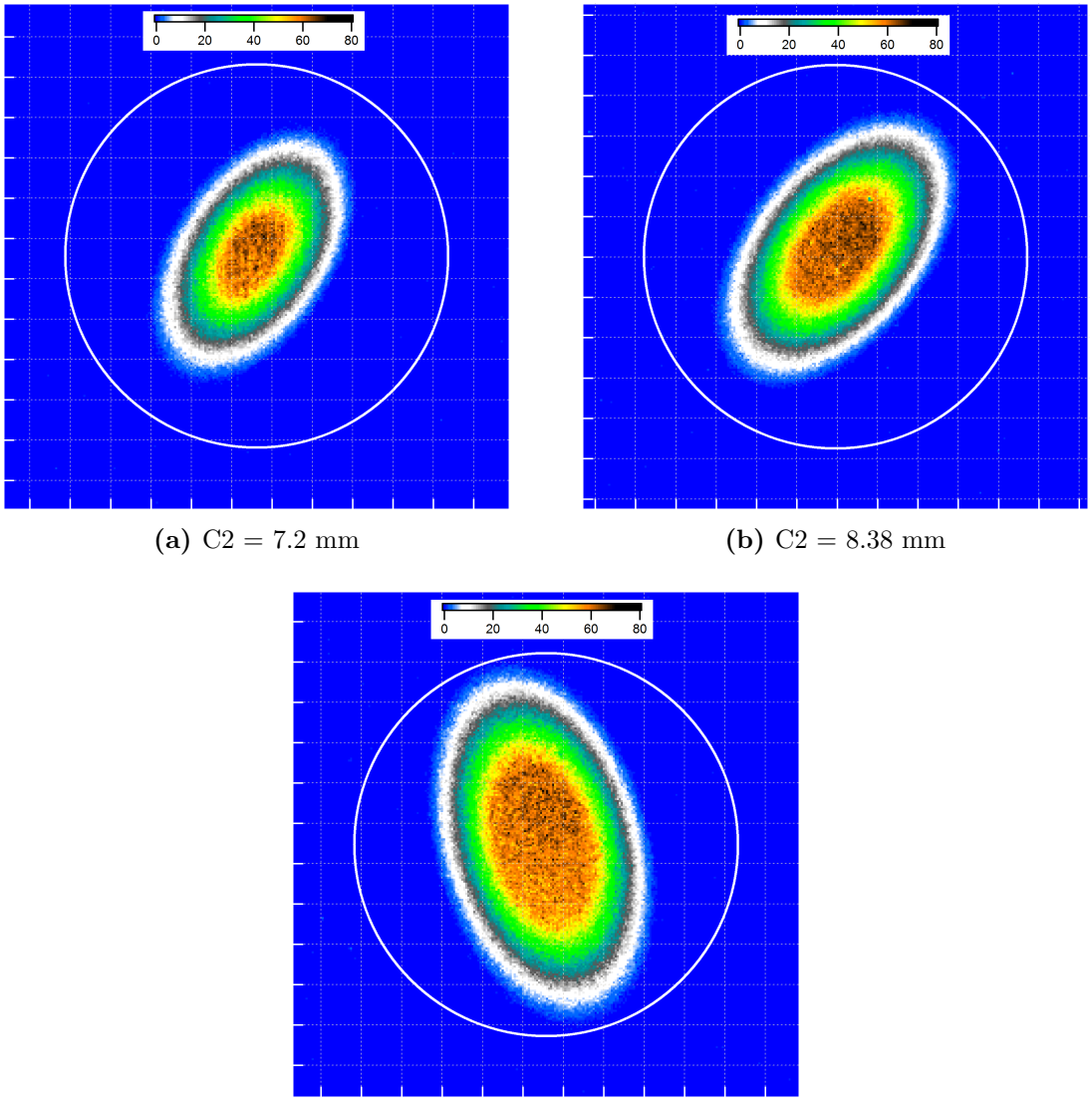
Table 4.2: Measured halo for each running configuration.

Configuration	PSL sum (38 mm)	PSL sum (50 mm)	Measured halo (fractional)
15/7	170799.74	170847.25	2.8×10^{-4}
15/8	304734.05	304869.34	4.4×10^{-4}
15/10	333335.47	333500.75	5.0×10^{-4}

a noise value per pixel. This can be complicated due to sources of nonuniform noise. The cleanest images are made on image plates that were erased just before exposure to the Dy foil and not subjected to any light exposure.

A peculiar artifact of the image reading process adds a nonuniform background to the image. As the plate reader scans through areas of high intensity, streaks perpendicular to the scan direction are left outside the boundaries of the beam image. This "galaxy" effect is shown in figure 4.8. Conceivably, this can cause a small distortion of the measured fraction of neutrons outside the active area of the foil. It is expected that our measured halo will be slightly larger than the actual halo because of this effect.

Figure 4.10 shows a radial profile of a 15/8 beam image, including the galaxy effect. Table 4.2 summarizes our findings for the halo including the galaxy effect. If the halo is a first order effect on the efficiency, then a $\sim 10^{-4}$ halo would need to be carefully studied. However, due to a built-in immunity in the Alpha-Gamma device, even a $\sim 1\,\%$ halo outside the thin target radius (but within the ~ 50 mm radius of



(a) C2 = 7.2 mm

(b) C2 = 8.38 mm

(c) C2 = 10.5 mm

Figure 4.9: Beam images at the Alpha-Gamma foil location with C1 = 15 mm and C2 = 7.2, 8.38, and 10.5 mm. The grid spacing is 4 mm. The white circle corresponds to the edge of the active area of the thin ^{10}B foil. Image orientation is arbitrary, but the 15/8 image is representative of the image that would be seen looking from the Alpha-Gamma alpha detector towards the target foil.

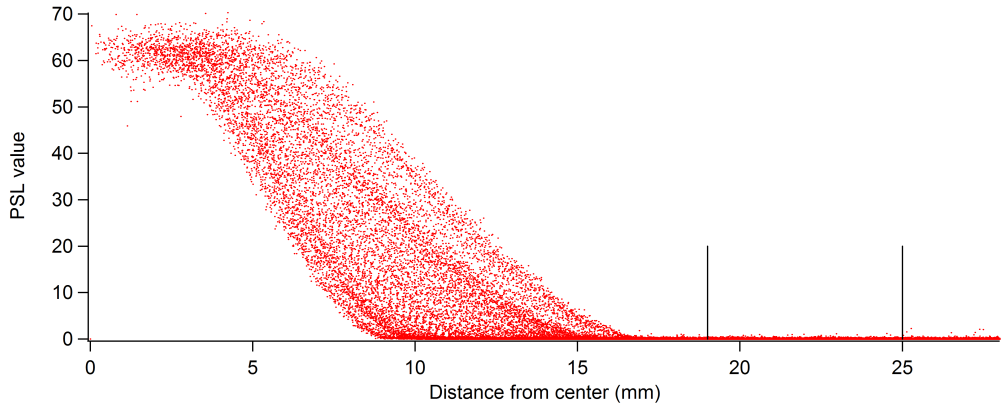


Figure 4.10: Radial profile of a 15/8 beam image. The red dots represent the PSL value of each pixel within the region of interest. The vertical line at 19 mm marks the edge of the active radius of the thin ^{10}B deposit and the line at 25 mm marks the edge of the steel mask of the foil holder.

the thick target) will not impact the neutron rate determination at a level greater than $\sim 10^{-4}$. Let 1 % of the beam fall outside the thin target radius as shown in figure 4.11. The reaction rate in the thin foil will be given by $R^* = 0.99R$. The measured α/γ ratio will be given by:

$$\alpha/\gamma(\text{halo}) = \frac{R^*\Omega^*_\alpha}{R^* b_\gamma \epsilon^*_\gamma} = \frac{\Omega^*_\alpha}{b_\gamma \epsilon^*_\gamma} \tag{4.6}$$

where Ω^*_α and ϵ^*_γ are the average α-detector solid angle and efficiency of the gamma detector for the truncated beam spot, respectively. The absorbed neutron rate falls out and the effect only shows up as the ratio of the two perturbed solid angles. If the thin target were made large enough to accomodate the halo neutrons we would have:

$$\alpha/\gamma(\text{no halo}) = \frac{R\Omega_\alpha}{R b_\gamma \epsilon_\gamma} = \frac{\Omega_\alpha}{b_\gamma \epsilon_\gamma} \tag{4.7}$$

Using the beam spot shown in figure 4.11, a simulation of each scenario shows

$$\frac{\epsilon^*_\gamma}{\epsilon_\gamma} = \frac{1/\alpha/\gamma(\text{halo})^{-1}}{\alpha/\gamma(\text{no halo})^{-1}} = 0.9996$$

That is, the perceived gamma detector efficiency is 0.04 % lower with the 1 % halo beam. We now switch to the thick target. Because the halo does not fall outside the extent of the thick target, the entire beam is absorbed and a gamma rate of R_γ is observed. The true neutron rate r_n is given by:

$$r_n = \frac{R_\gamma}{\epsilon_\gamma} \tag{4.8}$$

But the efficiency determined by the thin target (ϵ^*_γ) will be used to determine the perceived neutron rate r^*_n:

$$r^*_n = \frac{R_\gamma}{\epsilon^*_\gamma} \tag{4.9}$$

The error in the measured neutron rate is given by:

$$\frac{r^*_n}{r_n} = \frac{\epsilon_\gamma}{\epsilon^*_\gamma} = 1.0004 \tag{4.10}$$

Thus, a 1 % beam halo leads to a 0.04 % error in the determined neutron rate. For a 10^{-4} halo, the effect is completely negligible. By similar rationale, the galaxy effect has no meaningful impact on the measured neutron rate.

4.4 Measuring the Beam Wavelength

NG6m is generated by Bragg reflection of the NG6 polychromatic beam on a pyrolytic graphite monochromator. The direction and energy band of the reflected beam are determined by the lattice spacing (d) and orientation (θ) of the crystal planes with respect to the incident neutron beam. For neutrons of wavelength λ, the Bragg condition is given by:

$$n\lambda = 2d \sin\theta \tag{4.11}$$

Neutrons that satisfy the Bragg condition will be reflected 2θ from the main beam (roughly 90°). The Bragg condition is met for $\sim$ 5Å neutrons ($n = 1$), and thus $\sim$ 2.5Å ($n = 2$), and higher order reflections. The calibration of the neutron

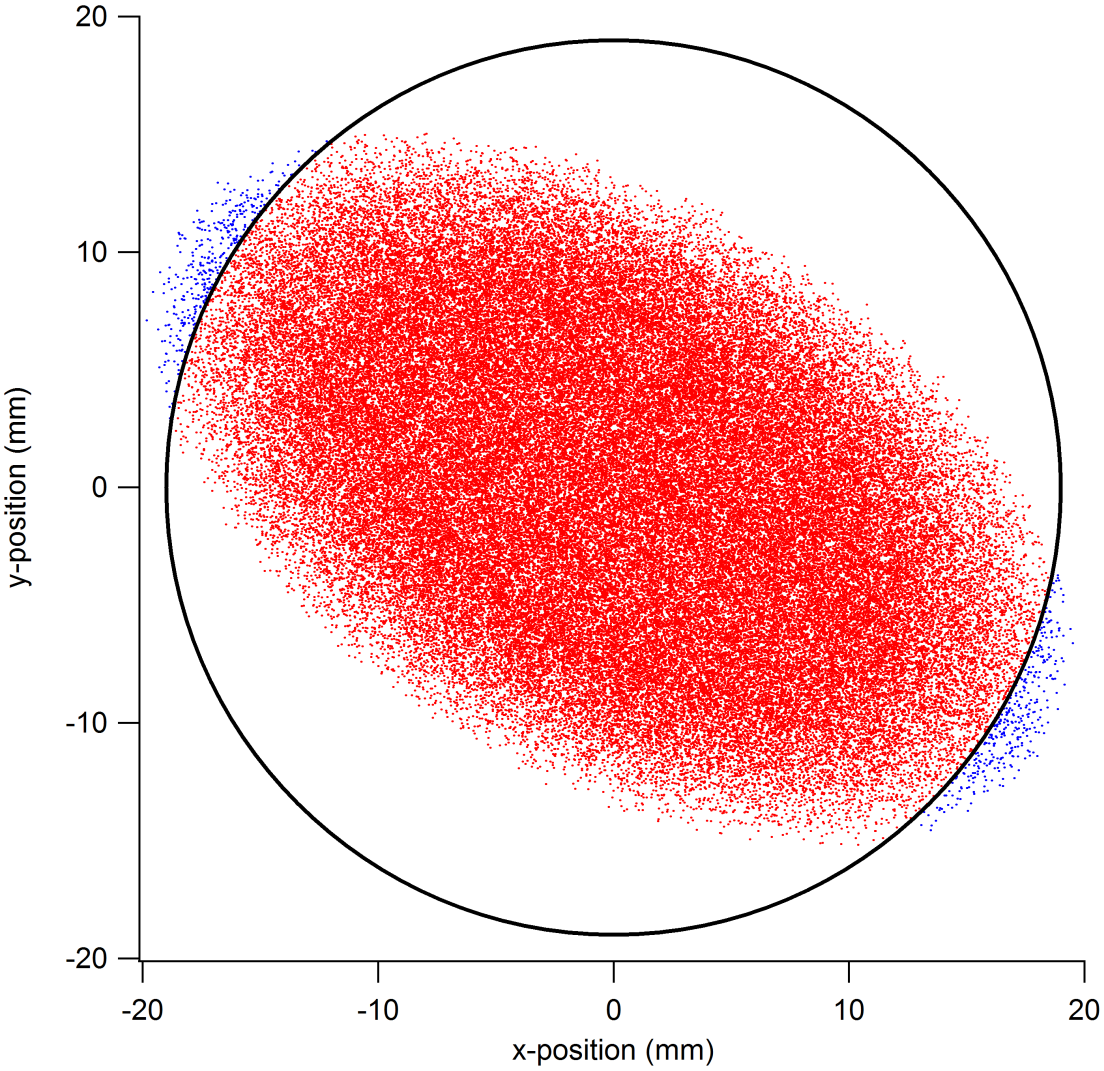


Figure 4.11: A hypothetical 1 % beam halo.

flux monitor must be performed with a beam whose wavelength distribution is very well characterized. While the $\lambda/2$ and lower wavelength reflections can be assessed, it is desireable to supress them as much as possible. This can be done with a polycrystalline material whose allowed Bragg reflections accept $\lambda/2$ and higher-order components but cannot reflect neutrons of wavelength λ. Polycrystalline beryllium has a Bragg cutoff of 3.96Å, which effectively removes higher-order components of the beam. Diffuse scattering due to phonon excitation occurs for all wavelengths, but it can be suppressed by cooling the crystal to 77K (figure 4.12).

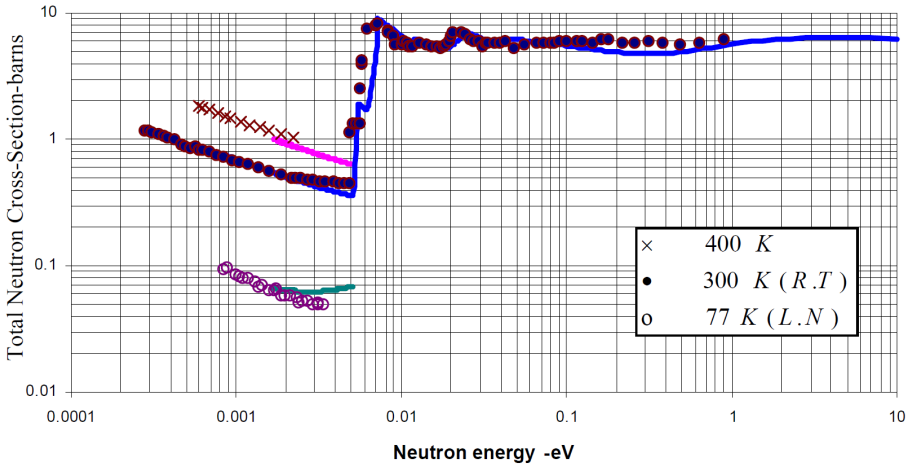


Figure 4.12: Neutron scattering cross section for beryllium [Wahba, 2002].

The principle used to generate the beam can also be used to measure its wavelength. The neutron wavelength is measured by Bragg diffraction from the (111) planes of a silicon crystal analyzer in Laue geometry. The Bragg condition is satisfied for a positive and negative angle. The monochromator has a mosaic spread leading to a small band of generated wavelengths. The silicon analyzer crystal also has an acceptance band. As such, a measurement of reflected neutron intensity versus angle will not be a plot of two delta functions, but instead two rocking curves. The positive and negative angles are determined from a weighted centroid of these two rocking curves. Highly uniform silicon crystals can be produced in sizes large enough to intercept a well-collimated neutron beam. The lattice spacing of perfect

crystal silicon is the most precisely measured lattice spacing. For cold neutrons at the wavelengths of interest the Bragg reflected beams are at large enough angles from the main beam to permit measurement at distances of $20 - 30$ cm. This separates the neutron detectors from the significant incoherent neutron scattering background from the silicon crystal. Absolute counting of the neutron rate is not necessary, but the accuracy of the change in angle between steps must be high. A typical stepper motor paired with a rotation stage will have a simple way to determine angle as a function of step number over a small angle range, but nonlinearities may develop over larger angle ranges. In this measurement, the crystal rotates nearly 120°, so the nonlinearities must be addressed.

The two neutron radiometer experiments performed precision measurements of the wavelength of the beam. Both of these measurements used the old monochromator, which was destroyed in March 2005. The Alpha-Gamma experiment was been the first on the reconstructed NG6m beamline to require precision wavelength information. In the current experiment, two separate measurements of the wavelength have been performed. Each of these measurements used a different setup.

The first measurement of the wavelength on NG6m was performed by Zema Chowdhuri in 1998. A perfect silicon crystal 4.7 cm long, 0.6 cm thick, 2.5 cm wide was mounted on a Huber tilt stage, which was then mounted on a Huber 408 rotation stage. No angle encoder was used in this measurement, so angle corrections for the rotation stage had to be calculated. The assembly was aligned such that the crystal sat at the location of the flux monitor target. A single ^{3}He detector that swung from one position to the other was used to have identical electronic noise and detection efficiency for parallel and antiparallel curves. Her final result was $\lambda = (4.963 \pm 0.002)$ Å. The $\lambda/2$ component was found to have an average wavelength of (2.479 ± 0.003) Å with a 0.1 % relative intensity with respect to the λ component.

The second measurement was performed by Greg Hansen in 2004. A perfect silicon crystal (dimensions of 60 mm$\times$ 25 mm $\times$ 4 mm) was used, and several pieces of the Chowdhuri apparatus were re-used. Beyond that, several improvements were made. A

Huber 408 rotation stage was used again, and a Heidenhain optical encoder was used to read out the crystal position. Instead of one ^{3}He detector, each side of the rocking curve had its own detector. Additional shielding was constructed for each detector to reduce neutron background. A beam monitor was added for rate normalization. An exhaustive list of systematic effects were measured and calculated. The final result from this measurement was $\lambda = (4.9592 \pm 0.0003)$ Å. A $\lambda/2$ component was found at an average wavelength of (2.48 ± 0.02) Å when the beryllium filter was removed. With the filter in place, the $\lambda/2$ component was found at 2.63 Å with a 0.05 % relative intensity with respect to the λ component.

Our first measurement was performed in 2007 as a proof of concept. The device is pictured in figure 4.13. Instead of the perfect silicon crystal used in the prior two measurements, we opted for a thick strained silicon crystal. The strain adds a small mosaic spread to the crystal which increased acceptance and thus neutron count rates in the detectors. The Huber 408 rotation stage and the Heidenhain optical encoder were used with an existing rotation stage mount, rotation shaft, and tilt stage. The device was mounted onto an optical breadboard that was mounted onto an instrument table made of extruded aluminum. The setup was placed at the Alpha-Gamma foil position and aligned by theodolite. The only centering marks on the wavelength apparatus were a pair of optics bench steel posts with small set screws sticking up from the top. By simultaneously aligning the center of the two set screws, the apparatus was aligned to the proper height and direction. The breadboard base for the device was floated above the rest of the instrument table by three screws. The tilt of the breadboard, and hence the axis of rotation of the apparatus could be controlled by turning the three screws and using a digital level to assess the tilt. Because this was a crude alignment method, the alignment of the device was tested implicitly by building it once, doing the measurement, breaking it down, and rebuilding and remeasuring. Two collimations were used: 35 mm upstream / 4 mm downstream and 35 mm upstream / 1 mm downstream. The same two ^{3}He detectors used in Hansen's measurement were used here. A measurement of $\lambda/2$ was attempted

while the beryllium filter was in place, but none was detected at the expected angle. An average wavelength of 4.9618 ± 0.0001 was measured. The data can be seen in figure 4.14.

It was clear that this setup would not be used for our final calibration for a number of reasons. While the strained silicon crystal gave us excellent statistical accumulation, the rocking curves were unnecessarily broad and asymmetric. The device had little fine alignment and rotation axis tilt adjustment, limited structural stability, and, most importantly, could not be operated with the Alpha-Gamma device in place. It was highly desireable to perform occasional measurement of the beam wavelength over the course of our efficiency calibrations to provide confidence that the wavelength was not prone to drifts. This measurement plan could not be easily realized with this setup.

With these problems in mind, a second apparatus was designed and built. Co-existence between the wavelength and flux monitor calibration setups was achieved by having the wavelength setup just upstream of the calibration setup. The height of the instrument table for the neutron monitor and the size of the air gap between the beam tube and the flux monitor were insufficient to simply place the previous crystal housing and positioning setup on the table. The most reasonable solution was to have the crystal housing and position control hang down from a frame.

Figure 4.15 shows a schematic of the new apparatus. Double-width aluminum extrusion makes up the lightweight but sturdy frame. The frame is fastened to the edges of the existing instrument table. Interior corner gussets and exterior joining plates provide excellent structural stability for the frame. The crystal positioning device is bolted into an adjustable aluminum block hanging from the crossbar.

The crystal positioning device is pictured in figure 4.16. It consists of a two-axis tilt stage to adjust the crystal rotation axis direction, an encoder-rotation stage pair, and a small one-axis tilt stage on the crystal housing to adjust the orientation of the crystal lattice planes. A custom aluminum frame (figure 4.17) was designed to hold the rotation stage and encoder parallel to one another, increasing fidelity

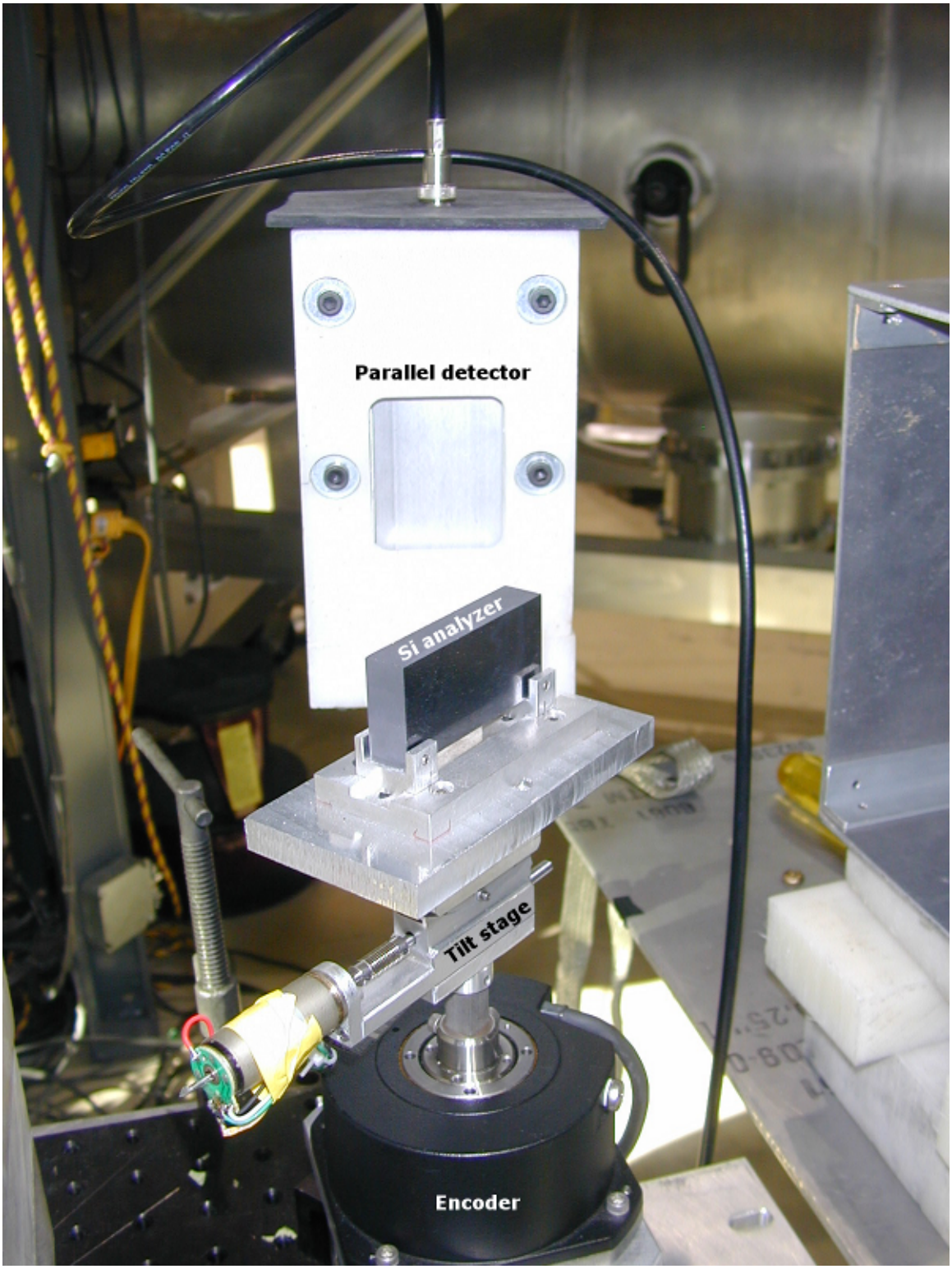


Figure 4.13: The 2007 wavelength test setup.

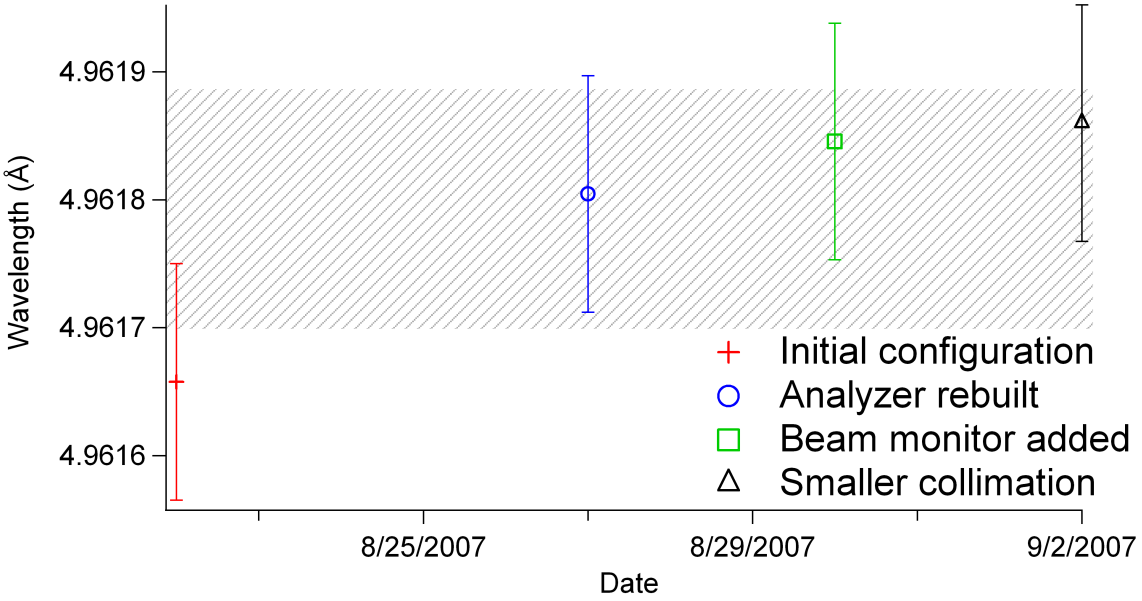


Figure 4.14: Wavelength measurements from the 2007 wavelength setup. The shaded band is a weighted constant fit to the data.

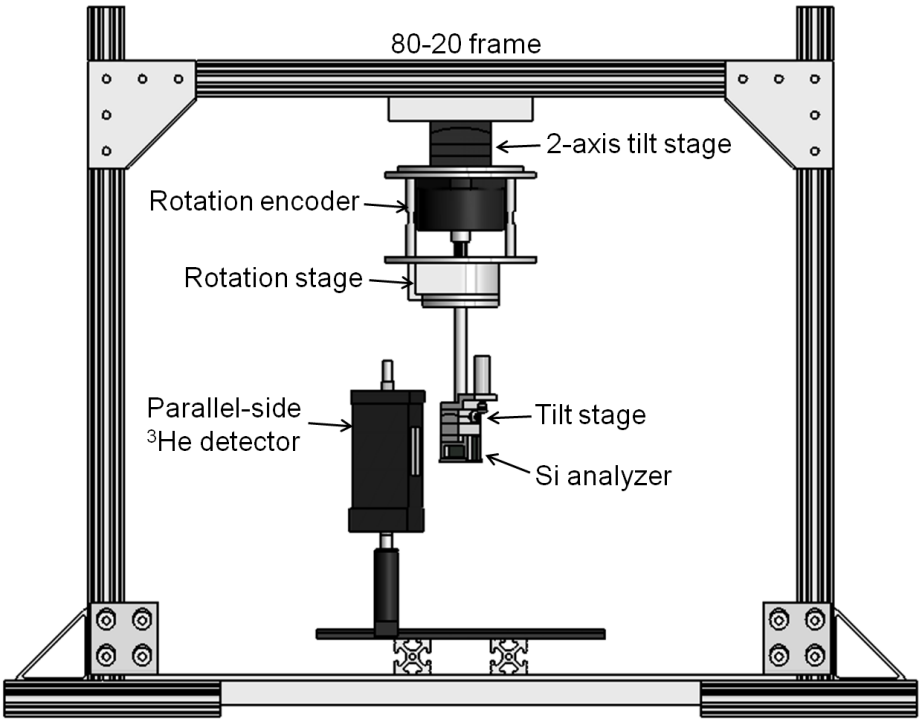


Figure 4.15: A schematic of the new wavelength measuring apparatus installed on NG6m.

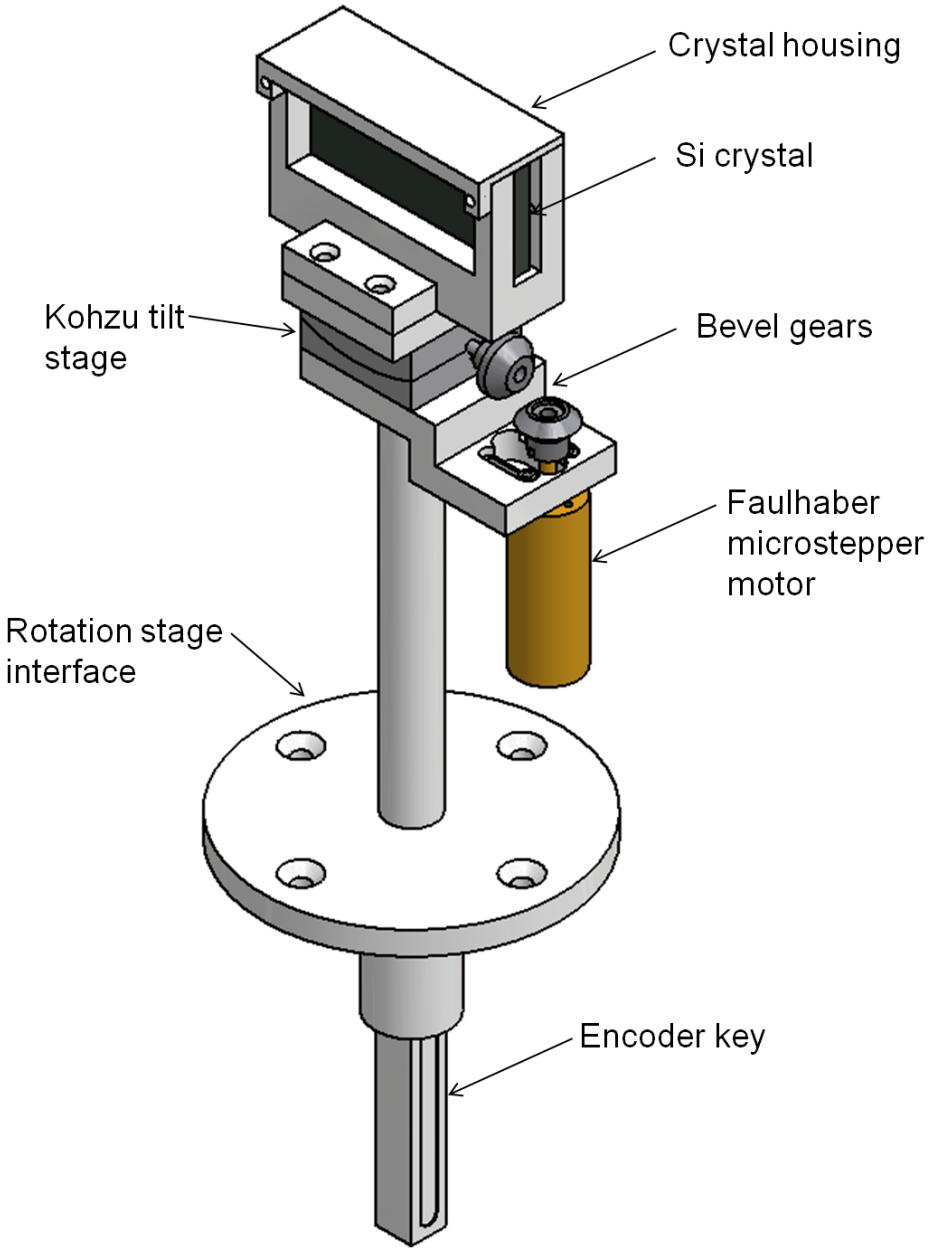


Figure 4.16: Detail of crystal housing and positioning device.

of the reported angle from the encoder. The rotation stage frame was assembled on the lathe. Parallel surfaces were ensured by turning each surface flat during the construction process. Similarly, the crystal rotation shaft was carefully turned from a single piece of aluminum, ensuring the crystal housing is parallel to the rotation stage. The perfect silicon crystal (the same used in Greg Hansen's measurements) sits in the rectangular aluminum housing. A felt strip on the bottom of the housing prevents any scratching or chipping of the crystal. Two 2-56 nylon-tipped set screws hold thin aluminum shim against the outer edges of the crystal. This provides just enough pressure to hold the crystal in all conceivable orientations while being mindful of adding unnecessary strain.

To align the setup, an aluminum block replaces the silicon crystal. The block (figure 4.18) is the same size as the crystal (60 mm$\times$ 25 mm $\times$ 4 mm) with a 1 mm diameter bore at the three-dimensional center of the block. Alignment is achieved when the center of the block is aligned with the beam sight line for all rotation and tilt angles. This requires proper x and y positioning of the crystal by adjusting the height of the crossbar and the position of the hanging aluminum block. We also require the rotation axis to be perpendicular to the sight line. An aluminum platform takes the place of the crystal rotation shaft on the rotation stage, and a digital level is placed on it. We level the platform along two perpendicular lines (nominally the two axes of the tilt stage, but this is not necessary) by leveling at one position, leaving the level on the platform and issuing the rotation stage a 90° rotation. The alignment procedure is repeated, and further iteration between the two steps quickly converges upon the proper alignment. No quantitative assessment is made of the alignment uncertainty, but an estimate can be made by the limit of our ability to discern a misalignment. Misalignment between the alignment bore and the crosshair can easily be detected at the level of 0.1 mm.

The same two 2 in x 2 in ^{3}He detectors used in the 2007 measurement were used to measure the parallel and antiparallel rocking curves. Optical table rails were set at two positions, allowing the detectors to be used at a position very close to the analyzer

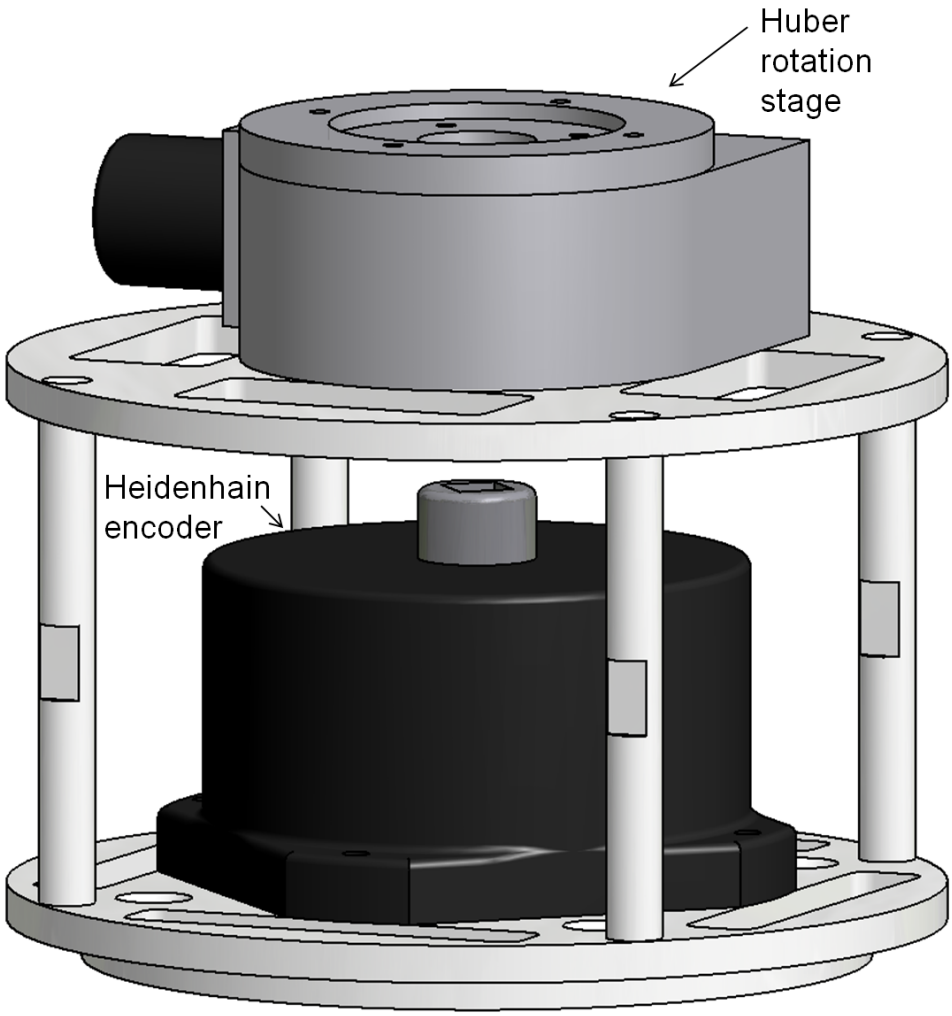


Figure 4.17: An aluminum frame ensures the encoder and rotation stage are parallel to each other.

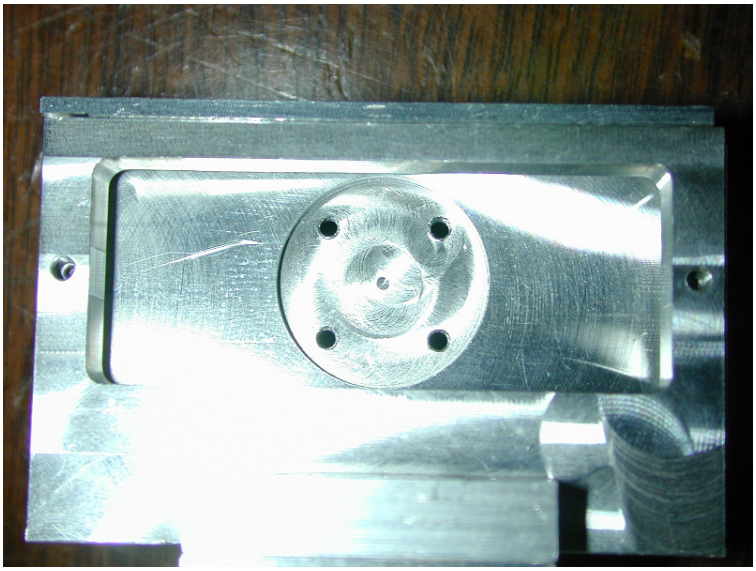


Figure 4.18: The aluminum alignment block inside the crystal housing.

(approximately 3 cm) or, more typically, approximately 20 cm away. This allowed us to measure the wavelength under very different neutron background conditions, which served as a check for any wavelength shift due to background change.

The wavelength measurement is made up of a succession of rocking curves and tilt curves. Rocking curves are measurements of reflected neutron intensity versus rotation angle. With the detectors set up and the crystal aligned, the first step is to roughly determine the parallel and antiparallel centroids (θ_P and θ_{AP}, respectively) with coarse rocking curves. The next step is to perform a tilt curve - a series of rocking curves at different analyzer crystal tilts. The crystal alignment procedure does not guarantee that the crystal planes will be properly oriented (perpendicular) with respect to the mean momentum vector of the neutron beam. Deviating from the optimal tilt presents a slightly larger lattice spacing to the neutron beam, and neutrons of higher wavelength will be accepted. Thus, the measured centroid of the rocking curve versus tilt of the analyzer crystal takes on a parabolic shape, with the optimal tilt located at the point of inflection of the tilt curve. Once the tilt curve is established, the analyzer crystal is set to the optimal tilt, and a final rocking curve is performed to determine the wavelength.

A typical rocking curve pair is seen in figure 4.19. The data acquisition code allows for multiple step sizes, so a coarse step is used to measure background at the "wings" of the rocking curve and a fine step is used to measure the peak. A quadratic fit to the background is performed. The fit function values for the background are subtracted from each point of the peak and a first moment calculation is performed. A typical tilt curve is shown in figure 4.20.

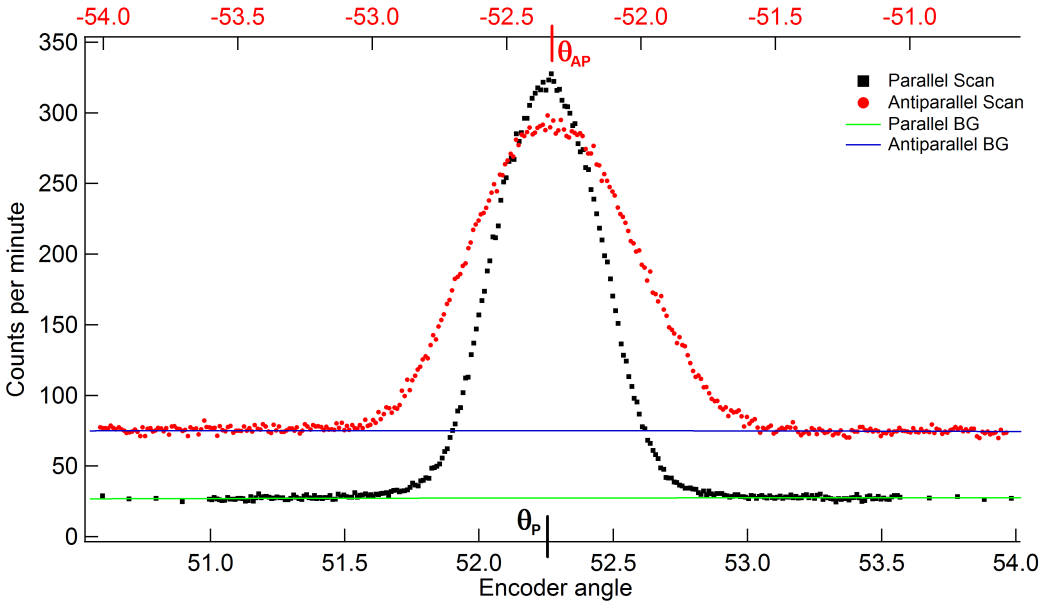


Figure 4.19: A typical rocking curve pair from the new wavelength setup.

The observed neutron background is a combination of the cold and thermal neutron background in the guide hall and incoherent neutron scattering from the crystal. The thermal neutron background is constant to first order, and the incoherent scattering is proportional to the amount of material the neutrons pass through. This is a simple function of the thickness of the crystal and its angle with respect to the beam : $t \sin\theta$. By using an aluminum plate in place of the silicon crystal, we demonstrated the sinusoidal nature of this background (figure 4.21). In the region around a rocking curve (about 6°), a quadratic is the appropriate fitting function.

A summary of the wavelength measurements performed with the new setup is seen in figure 4.22. The larger statistical uncertainty on the May 2009 data is due to the

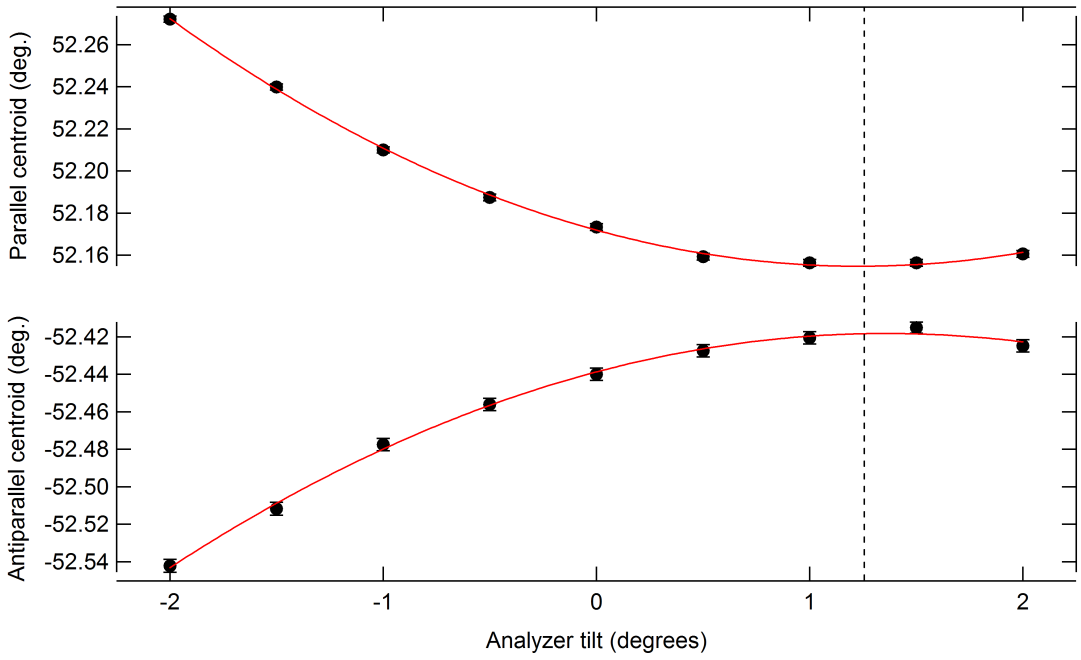


Figure 4.20: A tilt curve pair from the new wavelength setup. The dashed line represents the tilt that best minimizes the parallel centroid and maximizes the antiparallel centroid.

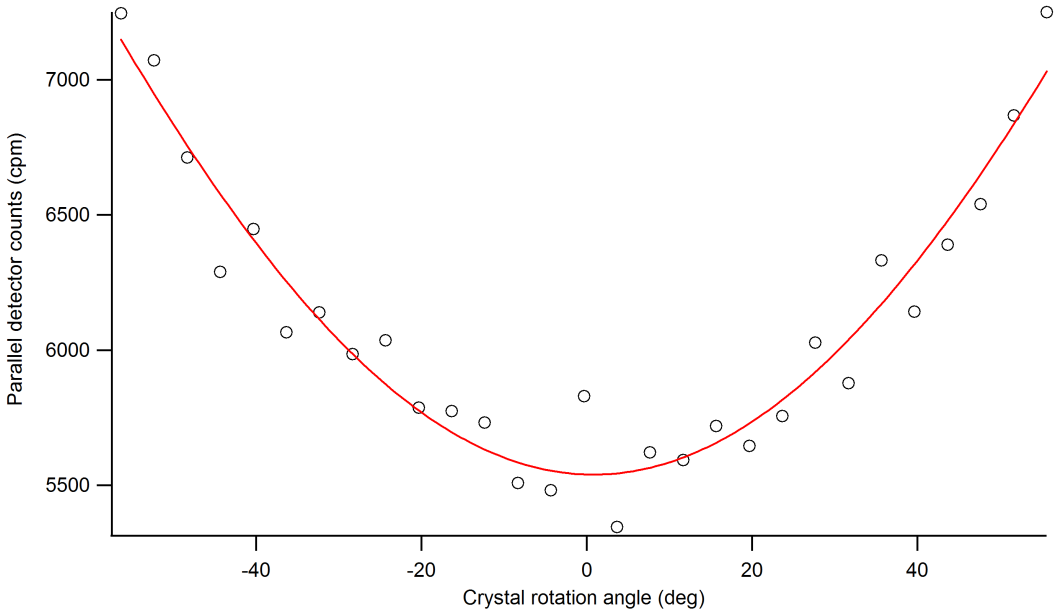


Figure 4.21: An aluminum block scanned over a wide angle range demonstrates the sinusoidal neutron background from incoherent scattering.

detectors being in the near position, causing larger backgrounds. Two measurement sets (June 2009 and February 2010) appear to be discrepant. It is suspected that the discrepancy is driven in part by an underassessment of the statistical uncertainty in each centroid. Yet, the clustering of these points is suggestive a possible shift. The origin of this shift remains unknown. A weighted fit to the data is used to find the Bragg angle. A conservative estimate of the uncertainty is made by using the standard deviation of the data set. This gives us $\theta_{\text{Bragg}} = 52.279(7)^\circ$. The silicon lattice spacing is known to a relative precision of 1.6×10^{-8} [Mohr et al., 2006]:

$$a = 5.431020504(89)\text{Å}$$

The (111) spacing is given by:

$$d_{111} = \frac{a}{\sqrt{(1^2 + 1^2 + 1^2)}} = 3.135601150(51)\text{Å} \tag{4.12}$$

Substituting into equation 4.11, we find $\lambda = 4.9605(5)$Å.

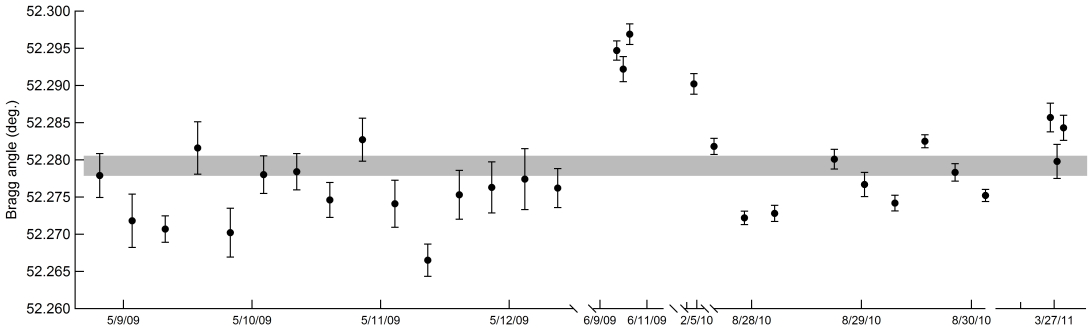


Figure 4.22: Measured Bragg angles from the new wavelength setup. The centroid of the shaded band comes from a weighted constant fit ($\chi^2/\nu = 23.2$) and the uncertainty is given by the standard deviation of the data set.

Despite the presence of the beryllium filter, there exists the possibility for a small $\lambda/2$ component. As such, a quantitative assessment of the $\lambda/2$ contamination is needed to determine the true composition of the beam. First, the location and

strength of the unfiltered $\lambda/2$ component is measured. Then, the filter is placed into the beam and a the $\lambda/2$ measurement is repeated. Figure 4.23 shows the unfiltered $\lambda/2$ component. A Bragg angle of 23.28(2)° is measured. This gives $\lambda/2 = 2.479(2)$ Å, which agrees well with dividing the λ result by two. The filtered $\lambda/2$ rocking curves are shown in figure 4.24. No detectable $\lambda/2$ component can be seen in the filtered beam, and no correction to the wavelength is necessary. This is in contrast to the conclusions reached by both Chowdhuri and Hansen. It must be mentioned that their results disagreed with one another, and our measurement was performed on a different monochromator.

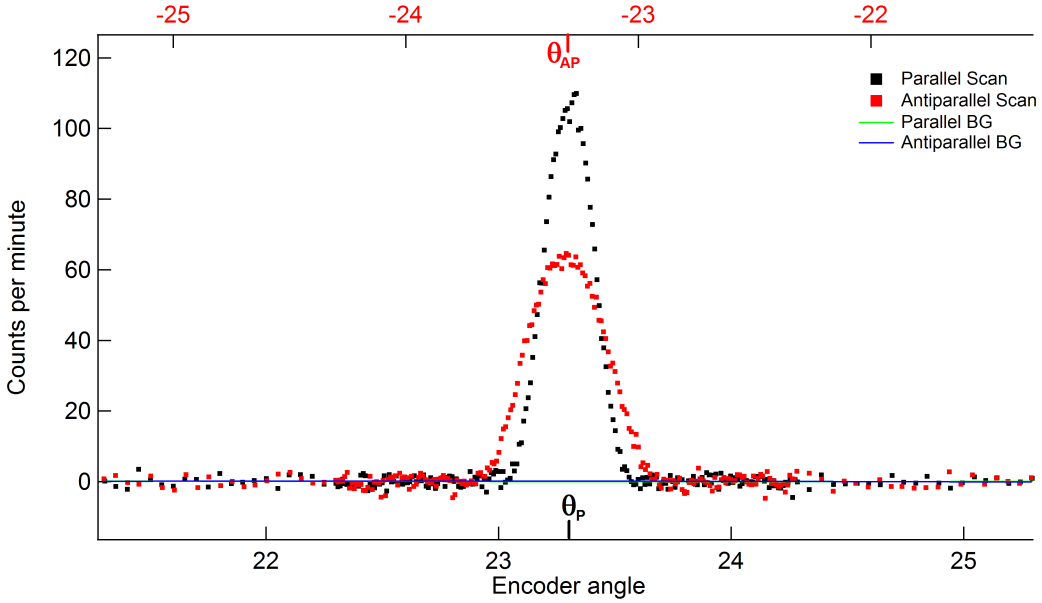


Figure 4.23: The $\lambda/2$ rocking curve for the unfiltered beam.

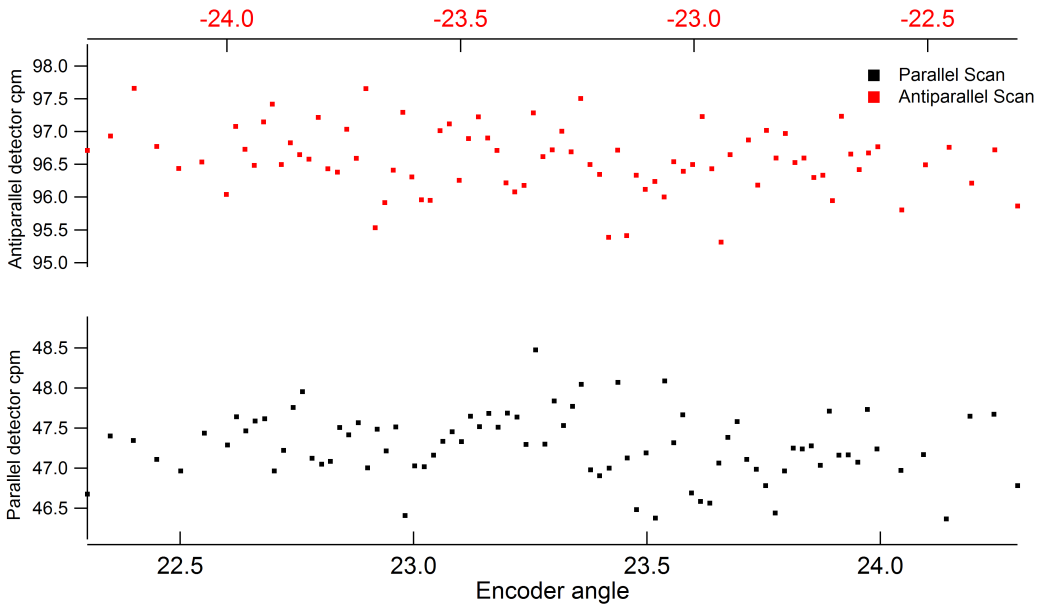


Figure 4.24: The $\lambda/2$ rocking curve for the filtered beam. Detectors were moved to the close position to increase count rate.

Chapter 5

The Alpha-Gamma Device

The Alpha-Gamma device has been used to measure the total neutron rate of a polychromatic cold neutron beam on one occasion. This work represents the first measurement in which the Alpha-Gamma device has been used on a monochromatic beam to calibrate the neutron flux monitor used in the neutron lifetime experiment. This chapter describes the Alpha-Gamma device in detail.

5.1 Device Construction

The Alpha-Gamma device is composed of an interchangeable target, a pair of HPGe gamma detectors and a PIPS detector masked by aprecision aperture. If the target foil center is taken to be the origin of a coordinate system (as illustrated in figure 5.1), the normal vector from the foil surface points in the (1,-1,1) direction. The gamma detectors view the target from the top and bottom, and the PIPS detector views the foil face-on from (1,-1,1).

The target foils are mounted in a two piece stainless steel foil holder pictured in figure 5.4. The foil sits in a 0.010" machined groove in the backing ring. The targets used are thicker than 0.010", so the target face presses up against the back of the front foil support. When the two pieces are bolted together, small spring washers (Belleville disc springs) are put in pairs on each of the four bolts that fasten the

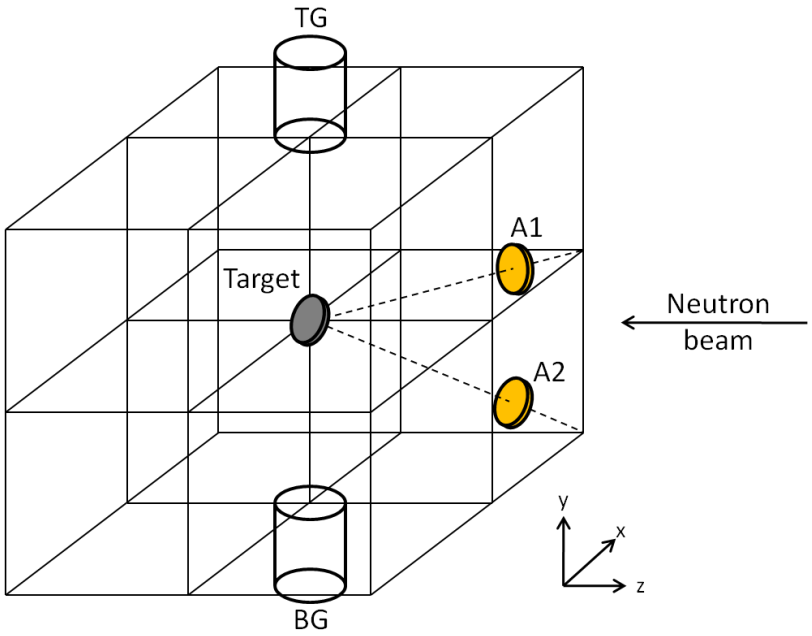


Figure 5.1: Alpha-Gamma detection geometry.

holder to prevent overtightening that could cause strains on the foil. The washers flex as the bolt tightens, which better distributes the force and keeps the foil from being damaged. The foil holder is held by an aluminum "arm" that points the foil in the (1,-1,1) direction. This "foil positioner" is permanently affixed to one of the side flanges on the Alpha-Gamma vacuum can. A weighted "trolley" bolts into the flange, allowing the flange and foil positioner to slide out of the vacuum can along a rail affixed to the south side of the device.

This foil loading system is necessary because several targets are used to calibrate the Alpha-Gamma device. For the alpha-to-gamma cross calibration to be valid, the positioning of the ^{239}Pu α-source and the ^{10}B foils must be identical to below 0.1 %. The ability to switch between target foils without disturbing the positioning of the target is essential. Since the device is used to count alpha particles from ^{239}Pu and $^{10}\mathrm{B}(n, \alpha + \gamma)$, the target foil and the PIPS detector must be in a common vacuum. With those two requirements in mind, the most sensible option for optimal foil repositioning was having the foil positioner attached to a kinematic mount held in

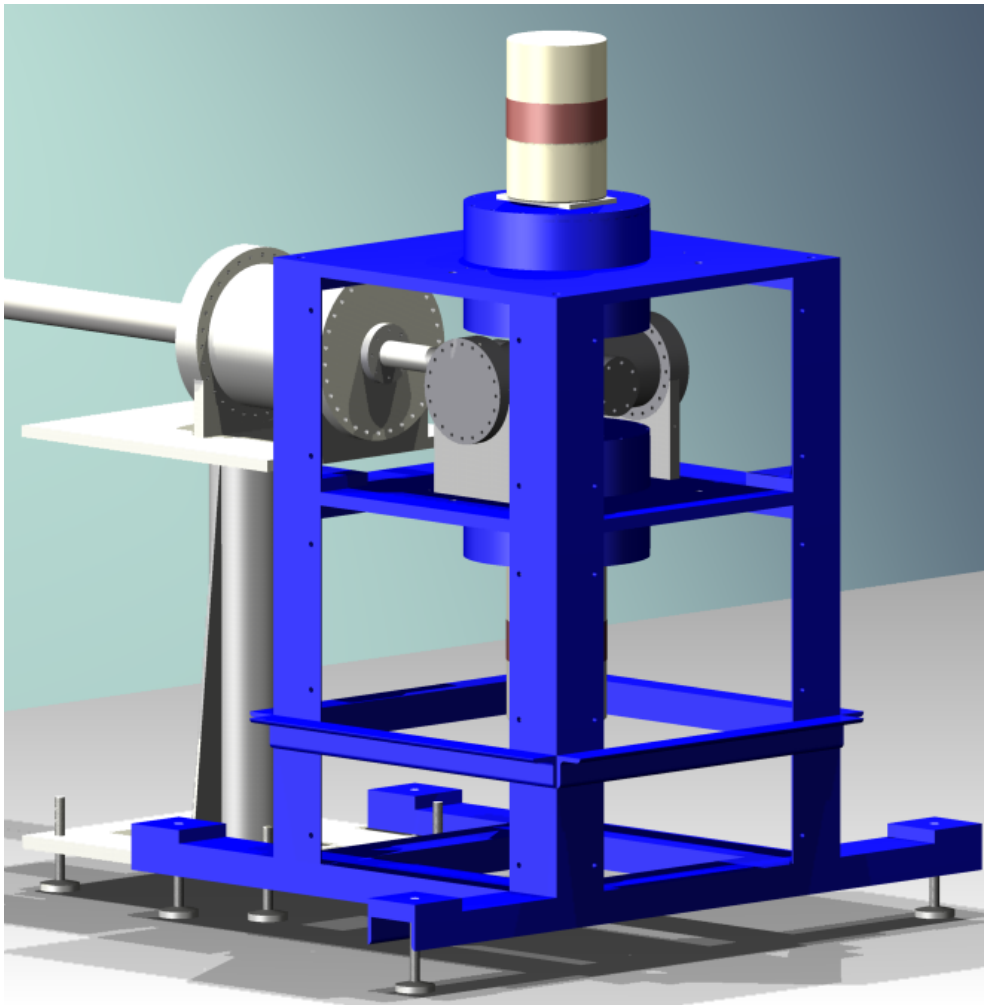


Figure 5.2: A rendering of the Alpha-Gamma vacuum can, surrounding support frame, and the neutron flux monitor.

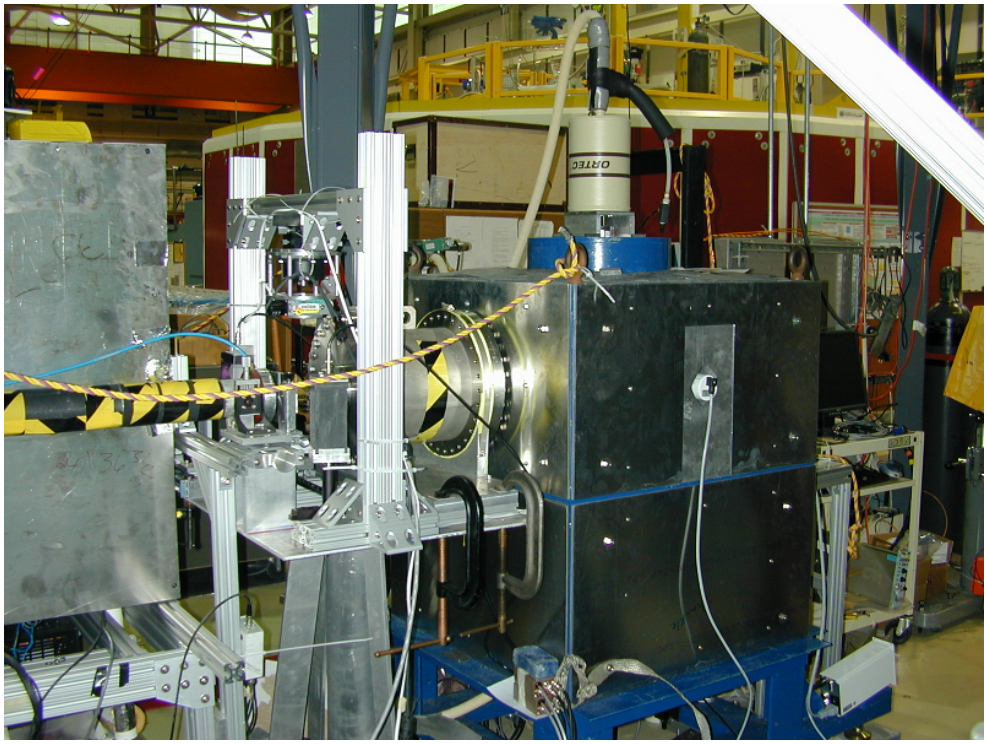


Figure 5.3: A photograph of the Alpha-Gamma device connected to the neutron flux monitor. The wavelength measuring frame is just upstream of the flux monitor.

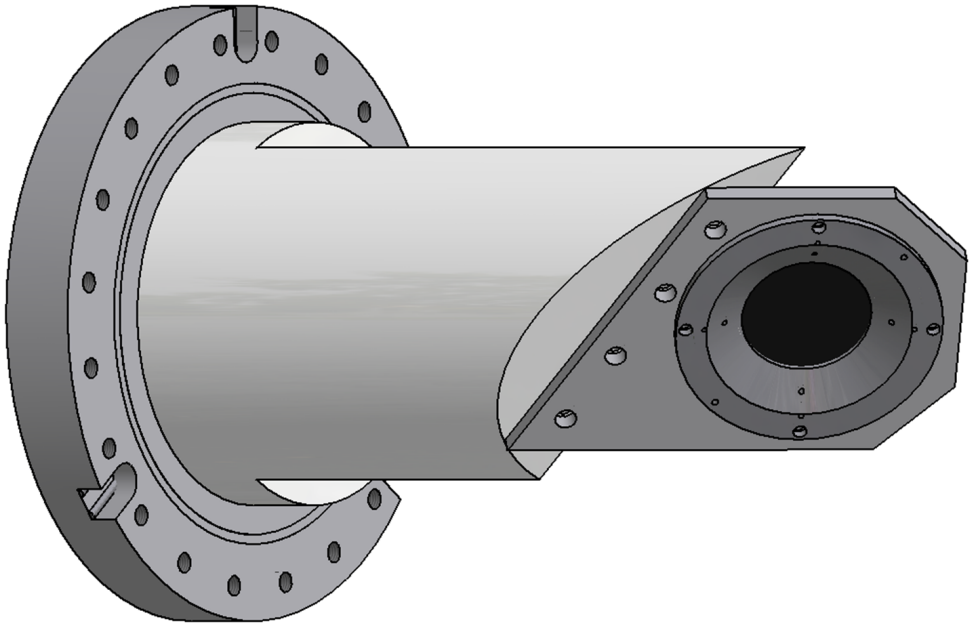


Figure 5.4: The target foil holder used in the Alpha-Gamma device. Three kinematic features on the flange mate with the vacuum can flange.

place by vacuum pressure. The foil loading side flange on the Alpha-Gamma vacuum can has three hardened steel ball bearings equispaced on its circumference. The loader flange has parallel rods made of hardened steel which make contact with their respective ball bearing at exactly two places (figure 5.4). This constrains the flange to move along the line defined by the parallel rods. Since there are three mating points on the flange, motion along any one line is forbidden by the other two and the positioning established by the mount is unique.

The reliability of the kinematic mount has been tested in two ways. A wire crosshair was placed at the foil location, and the downstream flange of the vacuum can was replaced by a vacuum compatible glass window. The can was pumped out to position the crosshair. The position of the crosshair was determined by observation with a theodolite, giving us the horizontal and vertical angles. The process was repeated several times, and the measured angles were steady to within an arcsecond at a distance of roughly 2.5 m, corresponding to a repositioning precision of ~ 10 μm. The positioning was also tested implicitly in the stability of our alpha source counting (section 5.4).

It is worth noting that the original kinematic flange used in the prior version of this experiment had very different kinematic features. The old flange made use of a cone (rotational constraint), a V-groove (linear constrant), and a flat (planar constraint). In our testing, we found this flange to be far worse at repositioning. It was later determined that this was due long term damage to the kinematic features. The entire flange is made of 303 stainless steel, which is far softer than the hardened steel ball bearings. The air pressure holding the flange in place was strong enough for the ball bearings to dig into the kinematic features, forming indentations and ruining the constraining properties. The current kinematic flange uses hardened steel rods for this reason, and to-date no damage has been detected.

Another critical feature for proper foil repositioning is choice of O-ring. The O-ring groove cut into the vacuum can flange can accomodate a range of O-ring sizes. If the largest size is used, the maximum compression of the O-ring by the two flanges is

insufficient to fully engage the kinematic mount. A custom O-ring of slightly smaller diameter was made, which was thick enough to maintain a vacuum seal, but thin enough to allow the kinematic mount to engage.

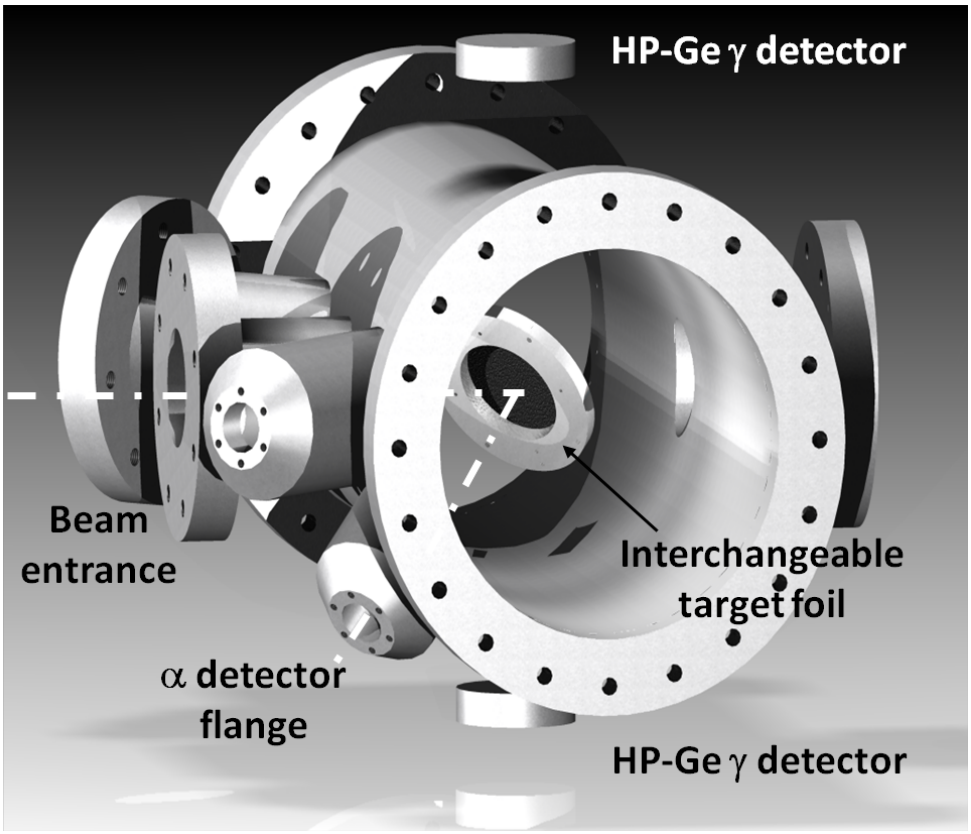


Figure 5.5: A rendering of the Alpha-Gamma vacuum can.

Figure 5.5 shows the main features of the Alpha-Gamma vacuum can. The PIPS detector is attached to a stem, which screws into a vacuum feedthrough. A small viton gasket makes the seal. A second feedthrough can support a second PIPS detector in the optimal geometry for operating the Alpha-Gamma device in coincidence mode. This mode of operation was not used in this project (see equation 3.10), so the feedthrough was closed off with a stainless steel blank flange.

The vacuum can end flanges rest in two aluminum cradles and are held by steel band fasteners. The cradles bolt into a large steel frame, which is designed to provide structural stability and to support the shielding necessary to protect the apparatus

from neutron and gamma-related backgrounds. Approximately half a ton of lead bricks fill the empty space surrounding the vacuum chamber. Eight composite panels made of borated rubber sheets (Boroflex) captured between thin aluminum sheet metal are bolted to the outside of the steel frame. The individual panels can be removed which provides ease-of-access, necessitated by the frequency of target changes and maintainance on the bottom gamma detector. The gamma detectors are mounted to the top and bottom sections of the frame, with their cryostats inserted into a lead sheath. Thin copper sheets line the lead sheaths and shield the detectors from low-energy gammas from the lead.

Vertical alignment of the can is done by adjusting the height of the four threaded feet that support the Alpha-Gamma frame. Coarse horizontal alignment is accomplished by movement of the frame with a pallet jack. Fine horizontal alignment is performed by loosening the band fasteners and carefully translating the can. Simultaneous vertical alignment of the foil and the upstream and downstream windows is done by rotating the can while the band fasteners are loose.

The charged particle spectroscopy needed to perform the calibration dictates a certain level of vacuum quality in our apparatus. PIPS detectors at bias cannot operate in the 10^{-3} - 10^{-2} torr range. At these pressures, a PIPS detector will suffer from voltage breakdown on the surface, which can cause irreparable damage. This is not a very stringent pressure requirement - a typical roughing pump-backed turbomolecular pump achieves presures in the 10^{-4} torr range in several minutes in small vacuum cans. The south and north side flanges as well as the downstream exit flange have viton O-ring seals. The more permanent connections (the connecting bellows between the Alpha-Gamma device and the neutron flux monitor and the seals on the neutron flux monitor) are conflat. These connections have knife edges, designed for use with copper gaskets. Two full-range vacuum gauges and a dry turbomolecular pump connect to the vacuum can via KF40 connectors. Vacuum grease is kept to a minimum. The grease can become an aerosol under vacuum and

potentially deposit onto the PIPS detectors or target surfaces, leading to a hard-to-quantify loss mechanism for charged particle detection. Small amounts of Apiezon M (1.7×10^{-9} torr vapor pressure) are used to patch scratches in the kinematic mount flange. Pressures of 1×10^{-5} torr are typical in the apparatus. The complete experimental layout is outlined in figure 5.6.

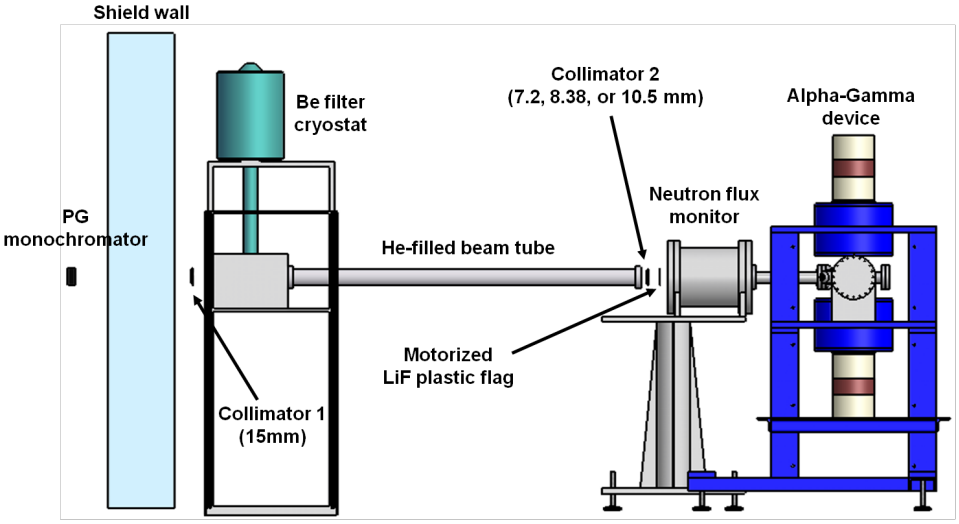


Figure 5.6: A side-view of the experiment layout.

5.2 Device Electronics

This experiment makes use of two types of diode detectors. Charged particle detection is performed with PIPS detectors. PIPS detectors offer low noise, excellent resolution, and a minimal dead layer, making them a good choice for an absolute counting experiment. Gamma-ray detection is performed with high-purity germanium (HPGe) detectors. Essentially all detectors used in this experiment follow the block diagram shown in figure 5.7. The impulse from the detector goes into a preamplifier (Canberra 2005BT for the PIPS, an internal preamp for the HPGe detectors). The preamplifier output is split, with one output going directly to an XIA Pixie-4 multi-channel analyzer (MCA) and the other going to a spectroscopy amplifier (Ortec for the HPGe, Tennelec for the PIPS). The amplifier signal is read into single channel analyzers

(SCA) for pulse-height discrimination (Ortec 550, 550A, and 551). Pulses meeting the necessary thresholds send TTL pulses from the SCA to the appropriate channel in a CAMAC hex counter.

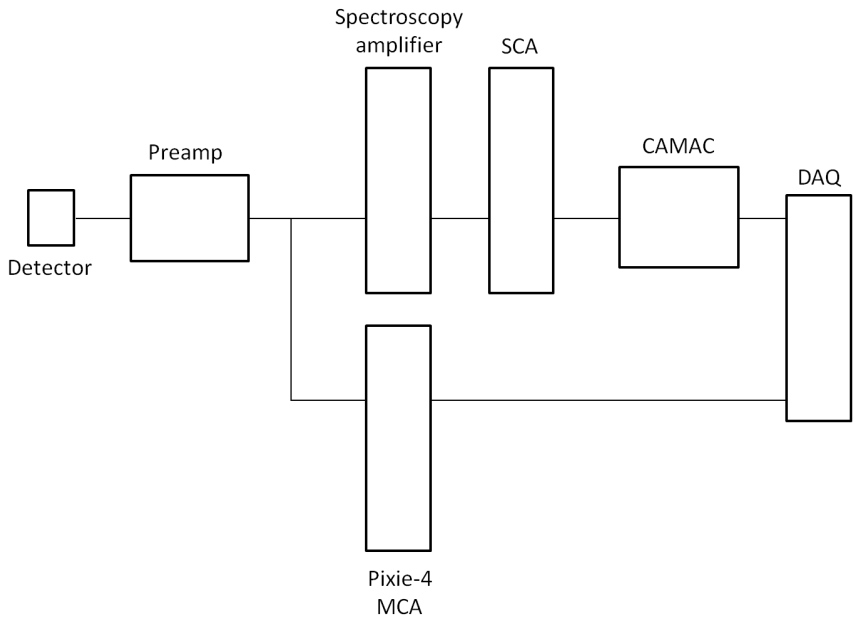


Figure 5.7: Block diagram of a detector's counting and spectroscopy electronics.

The highest signal rates in the experiment approached 400 s^{-1}. Dead times in the MCA system are large ($\sim$ 20 μs) and depend on the signal rate in the other channels. To avoid large and potentially difficult to calculate corrections for signal loss, a faster (2 μs dead time) SCA-based counting system was used for our data. The MCA is run in parallel as a diagnostic tool. Noise problems are most easily spotted in the change in spectral quality.

The $\sim 20 - 100$ mV preamplifier tail pulses are converted to $\sim$ 1 V gaussian pulses by a spectroscopy amplifier. An SCA operating in "normal" mode has two independent thresholds (lower and upper level). The gaussian pulse is read in and the SCA puts out a TTL pulse on the lower or upper level output as the signal rises over the respective threshold (figure 5.8). The threshold does not become "live" again until the signal falls below the threshold value. Peak summing is accomplished by

setting the lower and upper thresholds around a signal peak. The peak sum will be given by the difference between the lower and upper thresholds.

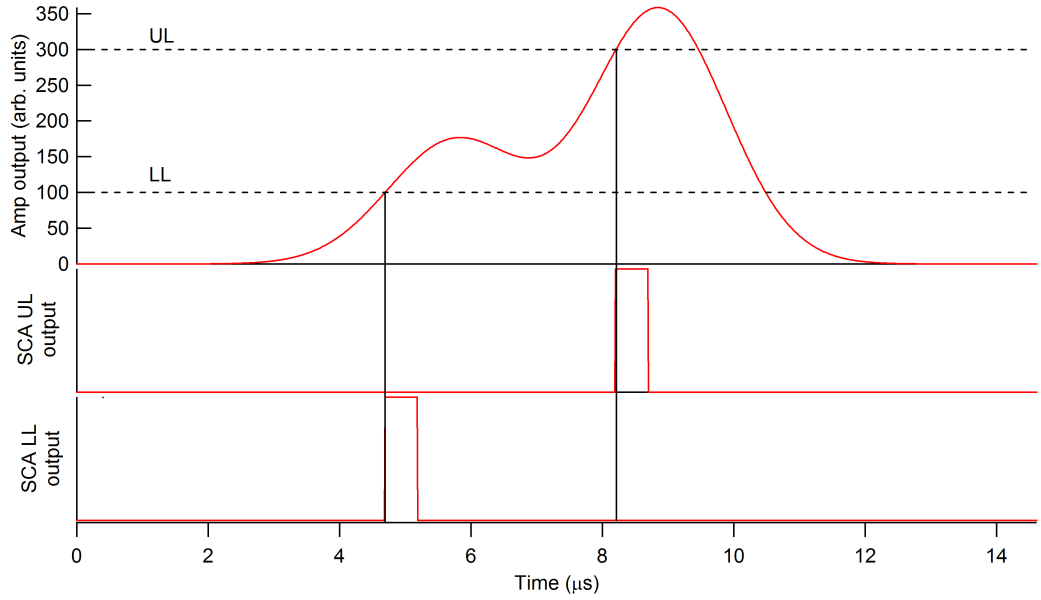


Figure 5.8: Cartoon of SCA operation.

The thresholds are set with a ten-turn potentiometer with a nominal range of 0 - 10 V. For an appropriate signal, it is possible to set thresholds based on signal peak voltages, but for a continuum spectrum like the gamma spectrum, it is difficult to decide what voltage to use. Instead, we use a Tracor-Northern portable MCA, which can take a shaped gaussian pulse as an input. A spectrum of the signal is acquired, and threshold channels are decided. The signal source is turned off (source removed, or beam turned off) and a tail pulser connected to the preamp test input is used to generate a sharp peak at the desired channel. The SCA threshold is adjusted until the count rate from that threshold is equal to half the input pulser rate. Since the pulser appears as a gaussian on the MCA, the threshold will have been tuned to be at the peak center.

A block diagram of the apparatus electronics is shown in figure 5.9. The data acquisition (DAQ) system is an in-house LabWindows program called "CC32DAQ" written by Scott Dewey. The primary operation the DAQ performs is communicating

via GPIB controller with a CAMAC crate. The program reads out 15 hex scalars every computer clock minute. The time between readouts can vary due to processor load, so we track a CAMAC millisecond timer with one of the hex scalar counters for finer timing information. The DAQ also communicates with a digital multimeter (DMM) via GPIB to monitor either the temperature of the berylium filter or the bias shutdown signal on a gamma detector. An Input Gate/Output Register (IGOR) module in the CAMAC crate is used to control the modulation of our upstream lithium flag, monitor the NG6 shutter status, and monitor the liquid nitrogen fill system.

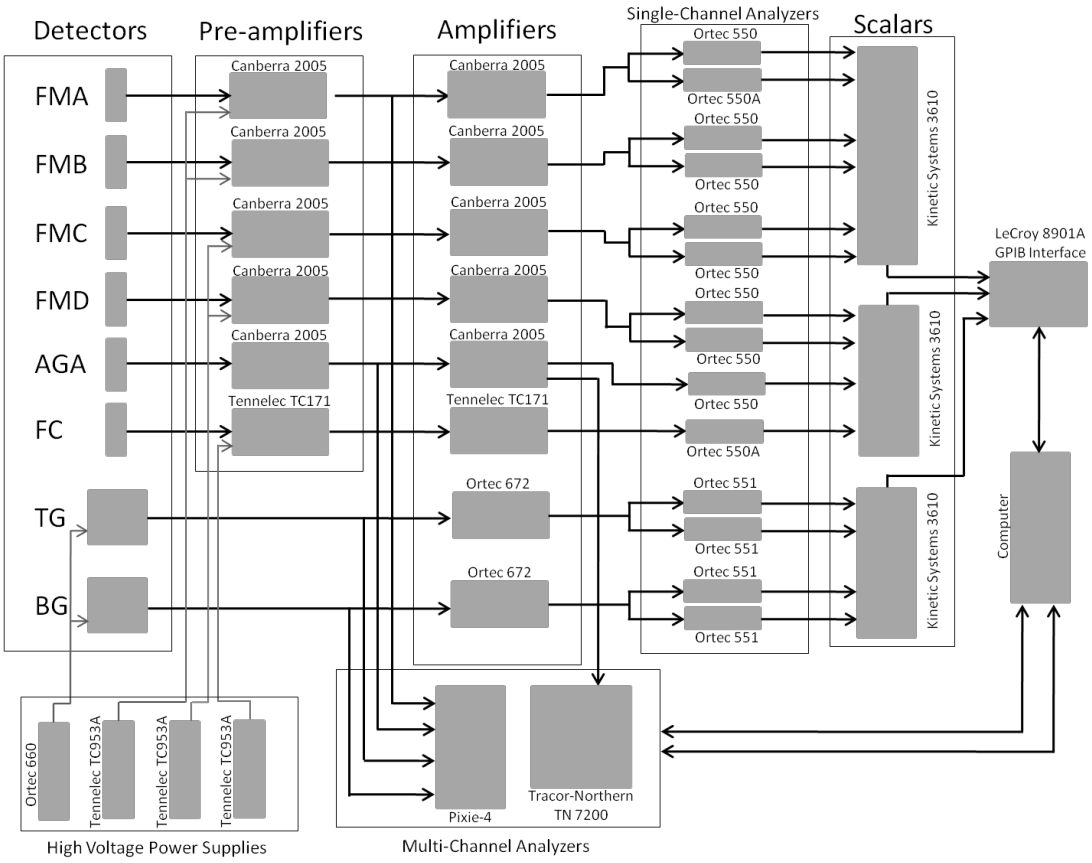


Figure 5.9: Alpha-Gamma device electronics diagram. FMA - FMD are the four neutron flux monitor PIPS detectors, AGA is the Alpha-Gamma PIPS detector, FC is an upstream fission chamber and TG and BG are the top and bottom HPGe detectors.

In addition to the scalar counting, four signals (the two gamma detectors, the Alpha-Gamma PIPS detector, and channel A of the flux monitor) were read in by a Pixie-4 module, a digital waveform acquisition card. Each channel is digitized by a 14-bit 75MHz analog-to-digital converter (ADC). The Pixie-4 card can store the waveforms for offline analysis, or the onboard pulse shape analysis can be used. It is capable of recording detailed coincidence events and storing traces. The PXI crate that houses the Pixie-4 card can be operated from the vendor-supplied Igor program as a standalone unit when an onboard computer is installed. Remote operation from a PC is performed with a PCI card and a communication card in the PXI crate. The module is then controlled with the same Igor program or user-generated code or commands. A four-channel MCA mode provides four spectra at up to 32K channel resolution. While all operating modes have this histogramming feature, the dedicated MCA mode sacrifices extra features to reduce overhead.

The calls available to outside programs were sufficient to permit synchronous operation with CC32DAQ. One minute, 16K spectra are taken alongside each minute data point and are buffered in memory. CC32DAQ offers an "SCA mode" for these spectra, which sums up a user-defined region for each minute spectrum and records their counts. At the end of every shutter cycle (typically 15 minutes of beam on data followed by 5 minutes of beam off), a beam on and beam off spectrum are wrote to a file. The DAQ keeps a summation beam on and beam off spectrum on display for quick diagnostics.

A second, vendor-supplied acquisition program reads in temperature data from three thermocouples placed around the apparatus. The PIPS detectors and, to a lesser extent, the HPGe detectors are sensitive to changes in ambient temperature. The guide hall has no temperature stabilization beyond normal heating and air conditioning. In addition to diurnal variations, work on the guide hall expansion exposed the small sections of the hall to the outside, making it more susceptible to changes in temperature. Gain shifts as large as 1 % were seen in the PIPS detectors

for temperature swings of ∼4°C, but the SCA windows were sufficiently wide that these shifts had no impact on our counting.

The original intent of the Alpha-Gamma device was to operate as an alpha-gamma coincidence device. Because of small anisotropies in the coincidence rate, two gamma detectors were necessary. Because of the low coincidence rate on NG6m, we operate in a transfer calibration mode, where having two gamma detectors is unnecessary, but convenient. The top detector is subject to several important gamma scattering corrections, and verification of the flux monitor efficiency with both detectors gives us greater confidence, and the ability to use both detectors for better statistical uncertainty.

HPGe detectors cannot be operated at room temperature because of prohibitively large leakage currents. The detectors are kept at 77 K by use of liquid nitrogen. An automated fill system transfers LN2 from a 125 L supply dewar to the 1.2 L reservoir dewars on the gamma detectors. The detectors were specced for 24 hours holding times with 16 hours recommended between fills. We found that the holding time decreased as a function of time since last vacuum annealing and decided to opt for more conservative intervals anywhere between four to eight hours. Most of the calibration data was taken with five hour intervals between fills.

The gamma detectors have an operating bias voltage of several kilovolts. For our calibration data, the top detector operated at 3300 V and the bottom detector operated at 4000 V. A dual channel high-voltage power supply designed specifically for use with HPGe detectors was used. A warming germanium detector that is kept at bias will be irreparably damaged, so the power supply reads in a bias shutdown signal from the detector. The bias shutdown signal changes state before the detector reaches unsafe temperatures, and the power supply drops the appropriate channel to 0 V. If the bias shutdown is discovered quickly, a fill will usually cool the detector back down below threshold. If the shutdown is not discovered for several hours, it is important to allow the detector warm up completely. So-called "short cycling" of the detector occurs when the cryostat temperature is high enough to allow the molecular

sieve to release the vacuum contaminants it had collected. If a fill occurs, the detector will become the coldest element in the cryostat, and it will act as a cryopump for the contaminants. This manifests as a degradation in peak resolution. A day of warmup is recommended if the bias shutdown is not addressed immediately. Each of the gamma detectors has an SCA dedicated to conting the ^{10}B peak and one for counting a customizable region of the spectrum (either the four highest energy lines of a ^{133}Ba source or a pulser).

The thin ^{10}B target gamma spectrum is shown in figure 5.10. Prompt gamma lines from Si activation can be seen, as well as small amounts of background gammas from ambient sources (Ra, K, etc.). The 478 keV gamma from capture on ^{10}B is very broad due to a Doppler shift caused by the relativistic energy of the ejected ^{7}Li nucleus. The signal peak is still clearly resolved from the electron-positron annihilation peak present at 511 keV, but is only an order of magnitude resolved from background gammas. The thick ^{10}B target gamma spectrum is shown in figure 5.11. The 478 keV peak is significantly higher rate and is thus better resolved from the background. Still, the background is significant and proper gamma counting is the principle challenge faced in this experiment.

The Alpha-Gamma charged particle detector is a 900mm^2 PIPS that views the Alpha-Gamma target face-on from roughly 75mm away. The detector is housed in an brass aperture case with a precision 1 inch circular mask. The illuminated area has essentially unit efficiency. The Alpha-Gamma PIPS detector runs at 100V and uses one SCA to count both alpha peaks. The detector is also used to measure the ^{10}B(n,α)^{7}Li charged particle spectrum. Figure 5.13 demonstrates the outstanding resolution of the two alpha peaks from the surrounding thermal noise. In principle, the ^{7}Li peaks could be counted as well but the peaks fall on the noise tail. Additionally, the α signal has the highest rate of all the signals in the thin target mode, so increasing its rate by accepting an additional peak has little use.

The background in the Alpha-Gamma PIPS detector is sufficiently low that it is unnecessary to periodically measure it. However, the gamma background is only an

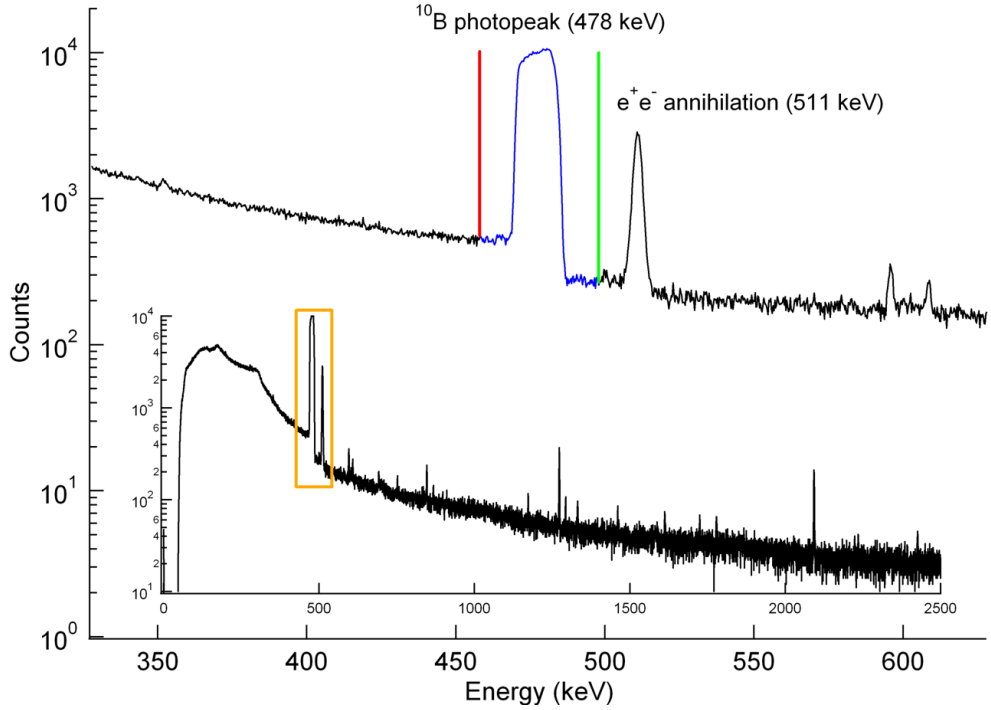


Figure 5.10: Gamma-ray spectrum from the thin ^{10}B target

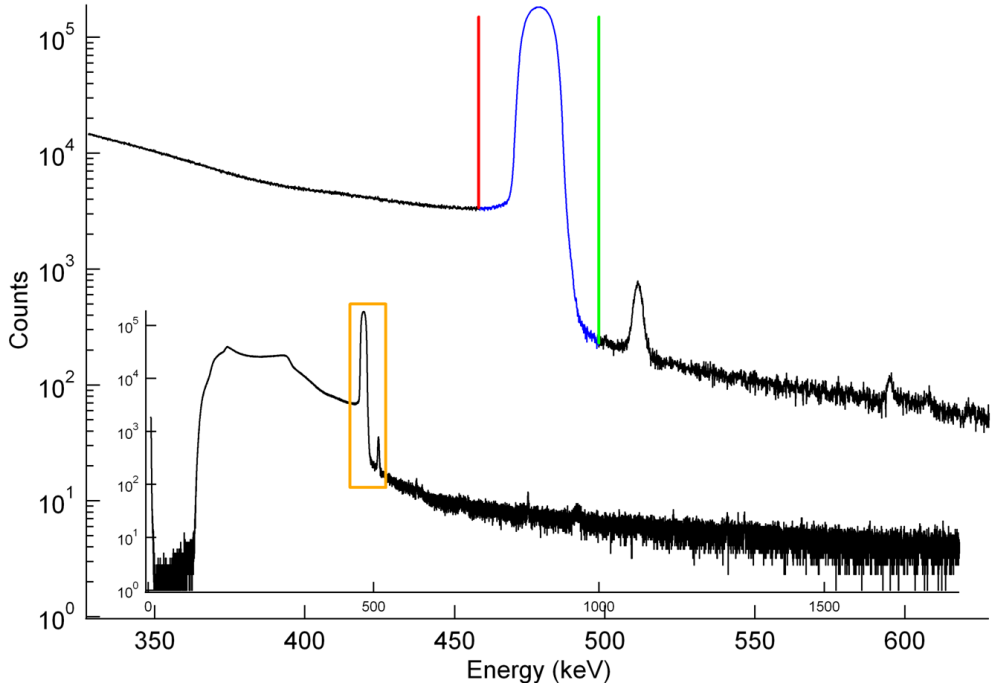


Figure 5.11: Gamma-ray spectrum from the thick ^{10}B target

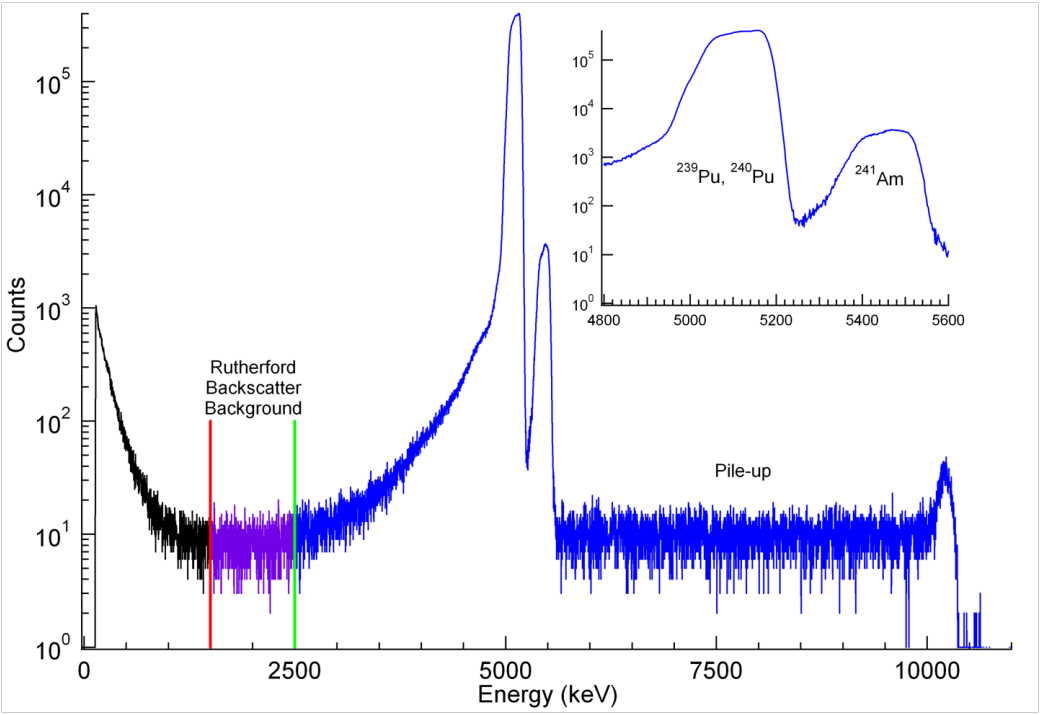


Figure 5.12: Charged particle spectrum from the ^{239}Pu source.

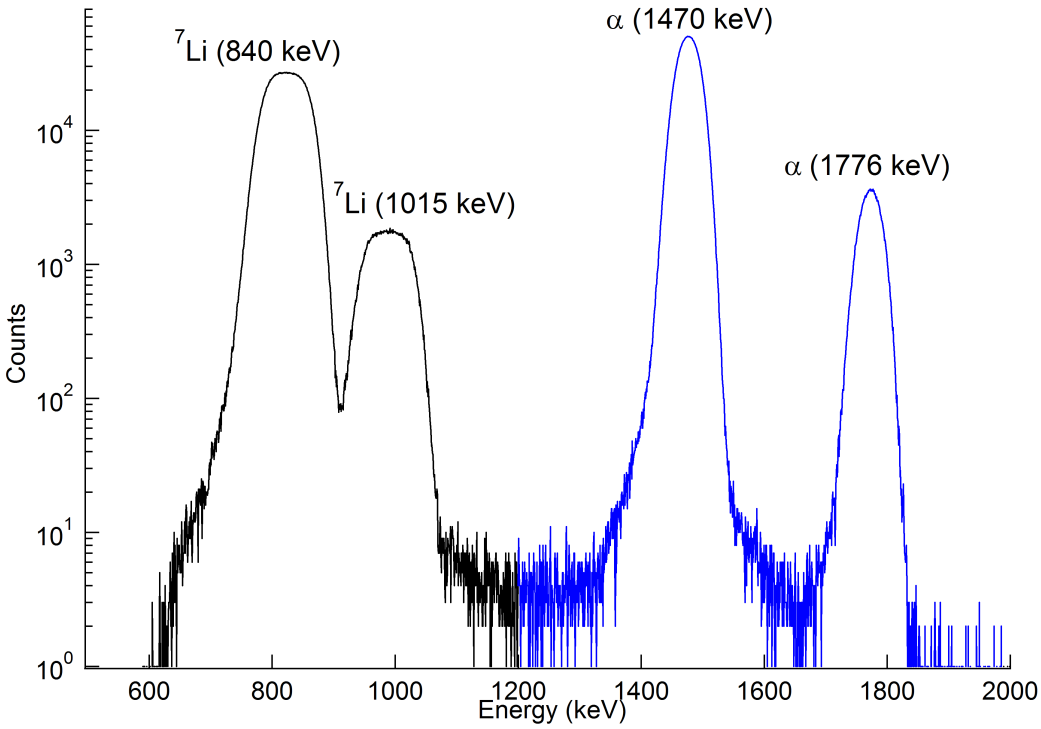


Figure 5.13: Charged particle spectrum from the thin ^{10}B target.

order of magnitude removed from the gamma signal in the thin target operating mode. Because the gamma counting is essential for both ^{10}B targets, all of our data (aside from the ^{239}Pu source measurements) includes periodic, dedicated measurements of the beam-off background. A motorized, thick ($\sim$ 0.5 cm) ^{6}Li-loaded plastic flag is used to modulate the beam in a 15 minute on, 5 minute off cycle. The critical ratios in the calibration (alpha counts to gamma counts with the thin target and thick target gamma counts to flux monitor counts) are determined for each 20 minute cycle and statistically combined for each run to determine the average ratio.

5.3 Plutonium Source Calibration

The calibration of the Alpha-Gamma device begins with the determination of the absolute activity of a long-lived alpha source. 49Si-3-3 is a ^{239}Pu source that was prepared as part of Plutonium batch 455A at Oak Ridge National Laboratory. A $\sim$10μg/cm^2 layer of ^{239}Pu was evaporated onto a single-crystal Si wafer held in a stainless steel mount. The spot diameter is roughly 3mm. The source has nine prominent alpha lines: three from ^{239}Pu, three from ^{240}Pu, and three from ^{241}Am (see Table 5.1). The small amounts of ^{241}Am comes from β-decay of the ^{241}Pu in the source. Qualitative comparison of the Pu and Am peak heights in spectra taken by Richardson and spectra acquired for this work suggest the isotopic composition of the source is stable.

Alpha emission from the source is isotropic, so it is sufficient to measure the source rate with a stack of known solid angle. A schematic of the source counting stack is seen in figure 5.14. The stack is defined by two pieces - a spacer and an aperture. The accuracy of this method has been verified through an interlaboratory comparison of the measured activity of actinide samples [Gilliam et al., 1999]. This method has been used to calibrate 49Si-3-3 on several occasions. Unique to our calibration of the source was the use of two different stack heights. The two counting geometries (Ω_{38} and Ω_{76}) are composed of identical parts aside from their threaded spacers, which

Table 5.1: Isotopic composition of batch 455A Plutonium [Richardson, 1993].

Isotope	Fraction	Half-life (y)	Energy (keV)	Rel. Intensity
^{239}Pu	99.1%	24110(30)	α_1: 5156.59(14)	73.3(8)%
			α_2: 5144.3(8)	15.1(8)%
			α_3: 5105.5(8)	11.5(8)%
^{240}Pu	0.888%	6563(7)	α_1: 5168.17(15)	72.8(1)%
			α_2: 5123.68(23)	27.1(1)%
			α_3: 5021.23(15)	0.0852(13)%
^{241}Pu	0.014%	14.35(10)	$\beta \rightarrow ^{241}$Am	99.998%
^{241}Am	N.A.	432.2(7)	α_1: 5485.56(12)	84.5(1)%
			α_2: 5442.80(13)	13.0(6)%
			α_3: 5388.23(13)	1.6(2)%

measure 38.294 ± 0.007 mm and 76.383 ± 0.007 mm respectively. Starting from the base of the stack, the relevant pieces are:

- Acrylic spacer - provides electrical isolation
- α source in foil holder sitting on a brass stand
- Large brass alignment cover
- Threaded spacer
- Precision aperture (Cu-Cu-1)
- Small brass alignment cover

The stack height was measured in two ways: by measuring the individual pieces and by measuring the entire stack. The measurement of the entire stack reported a height 9 μm taller than by addition of the piece heights. This was interpreted as gaps in the stacking. Since the combined stack cannot be shorter than the added total of the individual pieces, 4.5 μm is added to the height as determined by the individual pieces and 4.5 μm is declared the stacking uncertainty. This uncertainty is not a correlated uncertainty between Ω_{38} and Ω_{76}, as the amount of slop in the stack will vary with re-assembly, which occurred every time the threaded spacers were switched.

Cu-Cu-1, a copper-coated copper precision aperture, defines the space visible to the detector. Its diameter is 25.6725 ± 0.0030 mm. The defining edge is thin, minimizing alpha reflection. Solid angles for the two stacks were calculated by computer (corrected for spot size). The results (in units of 4π) are $\Omega_{38} = 0.016011$ ± 0.042 % and $\Omega_{76} = 0.0052857$ ± 0.031 %. Note that the aperture uncertainty is a correlated uncertainty, and contributes 0.023 % to the above uncertainties. The data from the two configurations was statistically combined (see appendix B) to determine the absolute activity of the source. The final result was $R_{Pu}^{4\pi} = 23545.2 \pm 7.0$ s^{-1}.

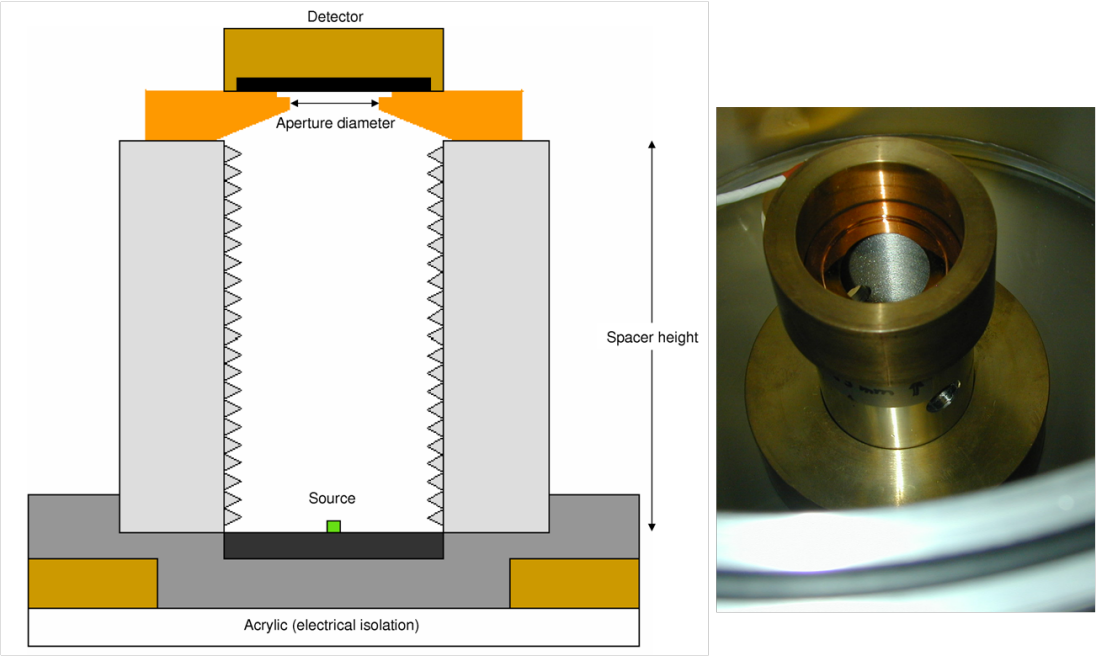


Figure 5.14: ^{239}Pu low-solid angle counting stack.

5.4 Internal Calibration of the Alpha-Gamma Device

The calibrated alpha source is used to measure the solid angle subtended by the PIPS detector in the Alpha-Gamma device. The source is loaded into the Alpha-Gamma foil holder and counted for approximately a day. Several weeks were dedicated to

repeated measurements of the source activity to assess the stability. A plot of the measurements is found in figure 5.15. The observed count rate is 168.43(2) s^{-1} after correction for dead time (see section 6.1), giving the source-determined solid angle of the alpha detector $\Omega = 0.007153(2)$ in units of 4π.

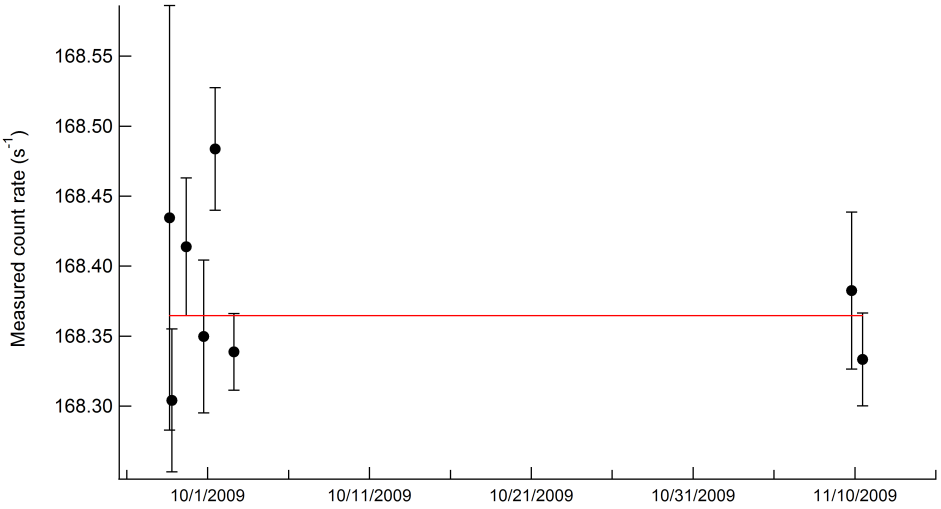


Figure 5.15: Activity of 49Si-3-3 measured with the Alpha-Gamma PIPS detector.

With the PIPS detector solid angle known, the next step is to use the thin ^{10}B foil to transfer the calibration to the gamma detectors. All the flux monitor efficiency measurements were performed using a 25 μg/cm^2 foil. There are two ratios of interest. The ratio of alpha counts over gamma counts (so-called α/γ) transfers the calibration of the alpha detector to the gamma detectors. The ratio alpha counts to flux monitor counts (so-called α/FM) provides a good check on the stability of the charged particle counting. The flux monitor foil did not move once the calibration began, so the ratio gives information about the positioning and size of the beam spot on the ^{10}B foil. The only discernable changes in α/FM have been in instances where the PIPS detector was changed (the foil-detector distance was shortened), and when collimation changes occurred. By increasing the size of the downstream collimator, the beam spot increases in size, and the average solid angle to the the detector decreases.

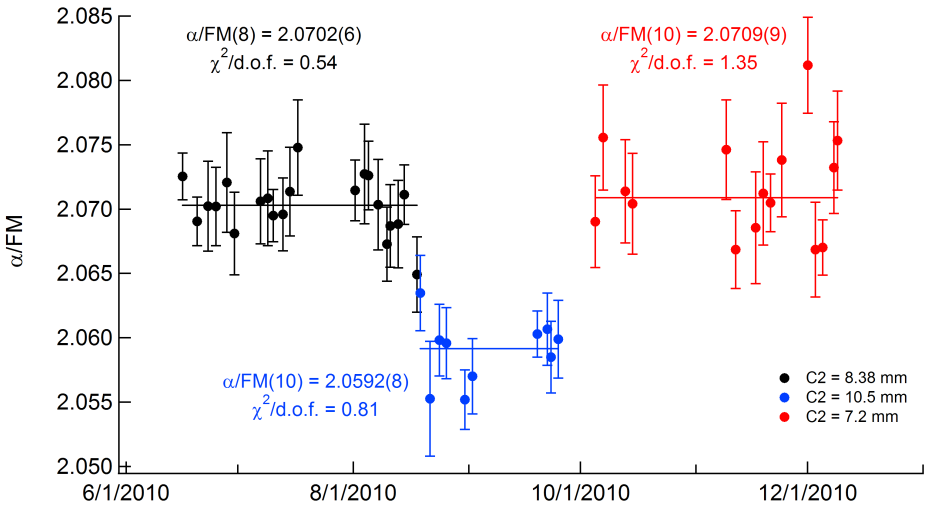


Figure 5.16: A plot of α/FM for our calibration runs.

A typical measurement of α/γ is shown in figure 5.17. The alpha rate was $\sim$ 25 s^{-1} and the gamma rate in each detector was $\sim$ 7 s^{-1}. Because of long-term gamma drifts, performing a statistical average of the entire set of measurements is meaningless. The method used to deal with these drifts is addressed in section 5.6.

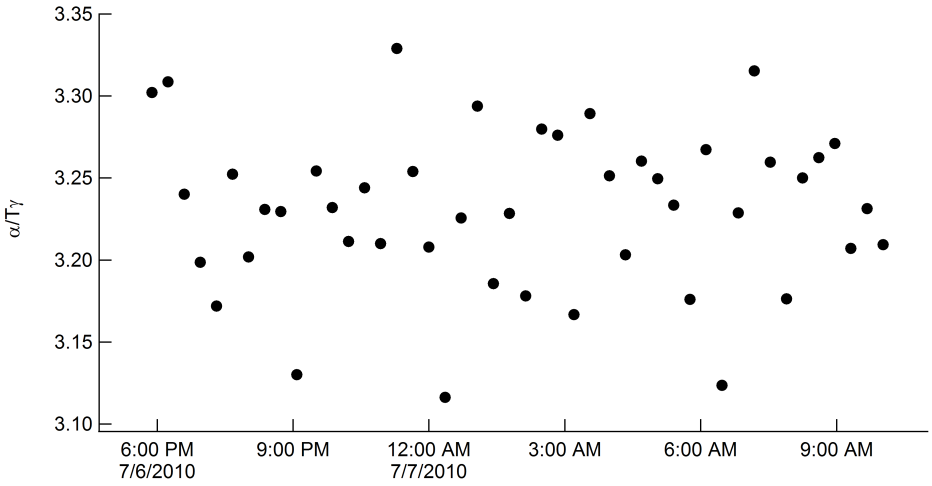


Figure 5.17: A typical measurement of α/Tγ from our calibration runs.

5.5 Calibration of the Neutron Flux Monitor

With the gamma detector efficiency-per-neutron established, the enriched $^{10}B_4C$ foil is loaded into the Alpha-Gamma. The relevant ratio here is gamma counts over flux monitor counts (γ/FM). Gamma rates in each detector are around 300 s^{-1} and the total flux monitor rate is about 6 s^{-1}. A typical measurement of γ/FM is shown in figure 5.18.

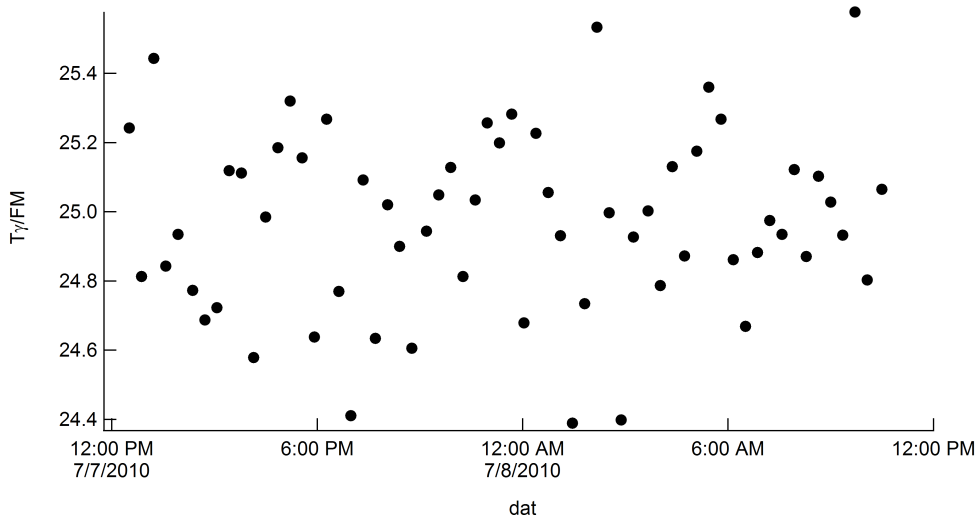


Figure 5.18: A typical measurement of Tγ/FM from our calibration runs.

Assuming stable gamma counting, a statistical average of all α/γ and γ/FM measurements could be used to make one high-precision measurement of the flux monitor efficiency. Figure 5.19 shows a common fit to α/γ and γ/FM data for the bottom detector over the period of a month. A $\sim$ -0.07 %/day linear drift can be seen. Thus, a statistical average of the entire data set will not arrive at the correct efficiency.

5.6 Accounting for Gamma Rate Drifts

The long-term linear gamma rate drift present in the apparatus was not due to gain shifts or resolution changes, but instead a change in the intrinsic efficiency of the

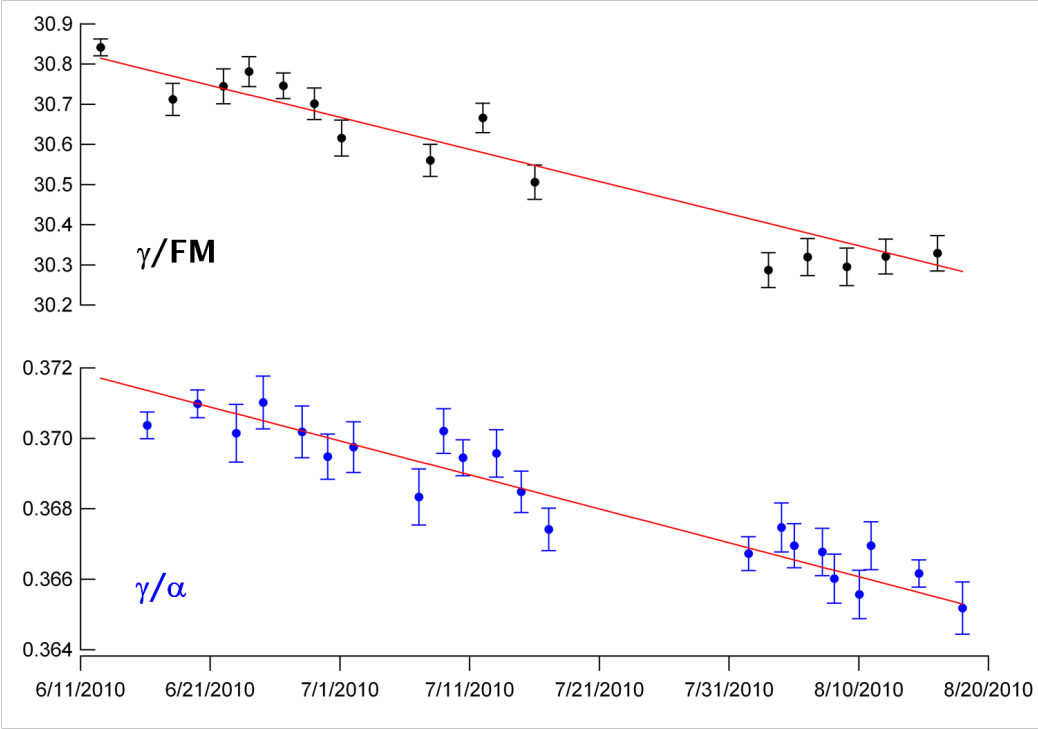


Figure 5.19: Data showing the long-term gamma rate drift in the bottom gamma detector due to drift in detector efficiency.

detector by an undetermined mechanism. The efficiency of the gamma detector must be stable enough that the calibration performed with the thin ^{10}B foil is valid while the thick ^{10}B foil is being used to calibrate the neutron flux monitor. With drifts on the order of 0.07 %/day, it is clear that the problem requires correction. This was accomplished by performing triplets of rapid measurements of the two critical ratios to correct for the drift. The triplets are made up of one day measurements of the two targets and use a thin-thick-thin pattern. The two thin target measurements are fit to a line and the α/γ value is determined at the midpoint of the thick run. The flux monitor efficiency is then determined from the extrapolated α/γ value and the γ/FM value. The data from the triplet method is found in chapter 7.

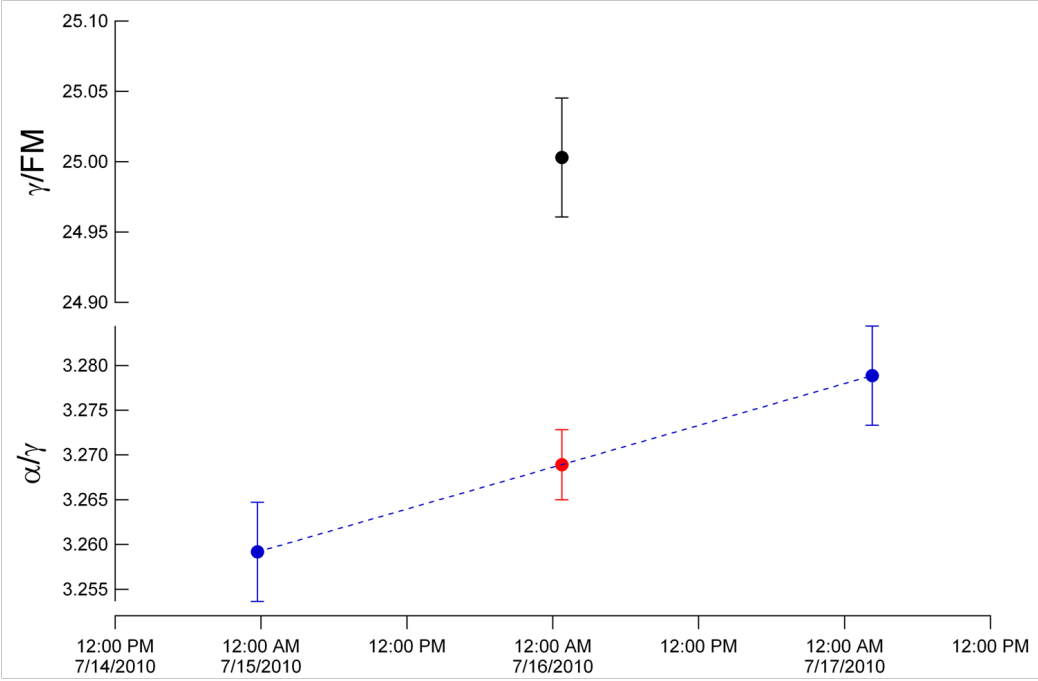


Figure 5.20: An example of the triplet correction method on data from the top gamma detector.

Chapter 6

Assessment of Systematic Effects

There are a number of systematic effects that contribute to the final value for the neutron flux monitor efficiency. Corrections to the overall efficiency are typically 0.1 - 1.0 % and are present in each step of the experiment. This chapter describes the anciliary experiments performed to assess the systematic effects. Apart from the α source systematics, each effect is expressed as a multiplicative correction to the efficiency of the neutron flux monitor. Note that ϵ_0 corresponds to the efficiency of the flux monitor used in [Nico et al., 2005b] and ϵ_0^{AG} corresponds to the efficiency of the flux monitor as measured in this work.

6.1 Corrections to the Plutonium Source

Calibration of the ^{239}Pu source is done in a straightforward counting experiment, but three systematic effects at the 0.01 % level emerge and must be measured to accurately determine the absolute disintegration rate of the source. The measured alpha counting rate in the counting stack PIPS detector must be divided by the detector solid angle to determine the absolute disintegration rate. Accurate metrology of the counting stack is the lynchpin of the entire Alpha-Gamma experiment. Uncertainty in the stack height is determined by measuring the assembled stack height and measuring the height of the individual pieces. The assembled stack is 9 μm taller than the sum of

the component heights, which is interpreted as a height uncertainty of $4.5 \pm 4.5 \mu$m in the assembled stack. As an additional check on the stack solid angle assessment procedure, the calibration was performed at two stack heights. The determined absolute activities from the two stack heights agree to 0.02 %. A description of the statistical combination of these results is found in appendix B.

Calibration and use of the ^{239}Pu source involve counting rates of $\sim$ 100 Hz. At these rates, dead times on the order of 0.01 % are present for typical SCA counting systems. The approximate dead time for our counting system will be given by the FWHM of the average signal amplifier output ($\sim 1.7 \mu$s) plus the time the SCA spends issuing a TTL pulse (0.5 μs). A definitive measurement is better. The measurement made use of the "two source" method, in which two measured rates are compared to the ratio of solid angles in the two setups. For this measurement, one source was used at two different stack heights.

In the non-paralyzable model of dead time, the true count rate (T) can be expressed as a function of the observed count rate (O) and the dead time (τ).

$$T = \frac{O}{1 - O \cdot \tau} \tag{6.1}$$

By either altering the solid angle or the source rate, a second observed rate and true rate can be found. The ratio of these equations yields:

$$\frac{T_1}{T_2} = \frac{O_1}{O_2} \left(\frac{1 - O_2 \cdot \tau}{1 - O_1 \cdot \tau} \right) \tag{6.2}$$

The ratio of true rates is just the ratio of solid angles, which have been measured. Therefore, one can solve for the dead time:

$$\tau = \frac{(U - 1)}{(O_1 \cdot U - O_2)} \tag{6.3}$$

where

$$U = \frac{T_1 \cdot O_2}{T_2 \cdot O_1} \tag{6.4}$$

Error, while essentially negligible for this measurement, was calculated by variation of the three independent parameters (O_1, O_2, and $\frac{T_1}{T_2}$) that determine the dead time. By varying these parameters by their standard deviation, we obtain a good estimate of $\frac{\mathrm{d}\tau}{\mathrm{d}O_1}$, $\frac{\mathrm{d}\tau}{\mathrm{d}O_2}$, and $\frac{\mathrm{d}\tau}{\mathrm{d}\left(\frac{T_1}{T_2}\right)}$. These quantities are then added in quadrature to estimate $\mathrm{d}\tau$:

$$\mathrm{d}\tau = \sqrt{\left(\frac{\mathrm{d}\tau}{\mathrm{d}O_1}\right)^2 + \left(\frac{\mathrm{d}\tau}{\mathrm{d}O_2}\right)^2 + \left(\frac{\mathrm{d}\tau}{\mathrm{d}\left(\frac{T_1}{T_2}\right)}\right)^2} \tag{6.5}$$

A high activity ^{240}Pu source (40-2-2) was used for this measurement. Because of the disintegration rate and the possibility of sputtering, a 30 μg polyimide film was used to prevent contamination of the threaded spacers and detector surface. The signal attenuation by the film is small [Gilliam et al., 2008], but irrelevant since the two source method only depends on the observed count rates. The dead time was determined to be 2.205(50) μs, which agrees very well with the pulse-width approximation (2.2 μs).

Emission of alphas is uniform over 4π, so backscattering off the Si backplate is possible, though infrequent. These alphas will be of energies from zero to the peak alpha energy. Examination of the MCA spectrum allows for the windows to be set in a region unoccupied by the noise tail and the forward-emitted alphas, leaving only the backscattered alphas (see 5.12). By taking the difference between the two SCA counters, we can assess the number of backscattered alphas per channel and extrapolate the number of backscattered alphas in the peak. Removal of backscattered alphas is a -0.04 % correction to the observed alpha count rate.

6.2 Corrections to Thin Target Data

A thin ($\sim 25\mu g/cm^2$) target of enriched ^{10}B is used to transfer the calibration of the alpha detector to the two gamma detectors in the Alpha-Gamma device. To accurately convert the observed $^{10}B(n,\alpha)$ reaction rate into the rate of total neutron capture events, an accurate measure of the solid angle is required. The alpha source determined solid angle is for a 3 mm uniform spot. The beam spot on the Alpha-Gamma target is elliptical and non-uniform, and the thin ^{10}B foil is not uniform in density. To correctly determine the solid angle for our beam spot, knowledge of the beam profile, deposit profile, and center-point solid angle are needed. The center-point solid angle can be calculated from the alpha source solid angle and the known detector aperture diameter. A program has been written to calculate the solid angle as determined by the alpha source for a given aperture diameter and detector-source distance. The aperture diameter is known (25.4 mm), and thus the detector-source distance can be determined. With the detector-source distance determined, the center-point solid angle can be calculated. The deposit areal density profile is given by:

$$\rho(x,y) = \bar{\rho}\frac{1-(1-0.995)\left(\frac{(x^2+y^2)^{1/2}}{19}\right)^2}{1-\frac{0.005}{2}} \tag{6.6}$$

where (x,y) is the position on the deposit (in mm) and $\bar{\rho}$ is the average areal density ($39.3\ \mu g/cm^2$) [Nico et al., 2005b]. The beam profile is measured with the dysprosium foil irradiation beam image technique.

The images were processed using the Igor software package. First, the "hole" on the image from the center hole in the dysprosium foil is plugged, then the background noise is removed, and finally the total PSL value of the region of interest is normalized to 1. At this point, each pixel of the image corresponds to a physical (x,y) position on the dysprosium foil. The image value from each pixel $I(x,y)$ is multiplied by $\Omega(x,y)$ (known from alpha-source determination of solid angle) and $\rho(x,y)$ (known from foil preparation work), and the sum over the region of interest gives the average solid

Table 6.1: Alpha-Gamma α-detector solid angle (Ω) for the three beam sizes used in the calibration.

Collimation configuration	Number of images	Ω (fraction of 4π)	ϵ_0^{AG} correction
15/7	2	0.0071099(4)	0.99276(6)
15/8	3	0.007042(1)	0.9896(2)
15/10	3	0.007016(5)	0.9848(7)

angle:

$$\bar{\Omega} = \int\int I(x,y)\Omega(x,y)\rho(x,y)dxdy \tag{6.7}$$

The uncertainty is determined by performing multiple beam images and using the average Ω. We estimate the uncertainty to be the standard deviation of the measured solid angles divided by the square root of the number of images taken. The results for each collimation are found in table 6.1.

The remaining systematic effects in the thin ^{10}B target are gamma-ray counting effects. The silicon backing on the thin target causes gamma-ray production by neutron absorption and gamma-ray attenuation as the ^{10}B capture gammas travel to the top gamma detector. Only $\sim$1 % of neutrons that impinge on the thin target will be absorbed by ^{10}B. A small fraction of the remaining neutrons will interact with the Si backing wafer and several capture gamma-rays are produced. These lines are of higher energy ($\geq$1.5 MeV) than the 478 keV boron capture gamma but can Compton scatter in the germanium crystal and incompletely deposit their energy. This background is not removed by measuring the thin target gamma background with the upstream ^{6}Li flag blocking the beam. Instead, the Si gamma background in the 478 keV signal region is determined by long runs with a Si blank target instead of the usual thin target. This background is a function of incident neutron flux, so the measured gamma rate must be divided by neutron flux. Because a silicon blank is used as the Alpha-Gamma target, the only choice for neutron flux assessment is the neutron flux monitor. Thus, the relevant experimental quantity is γ/FM which depends on C2 and gamma detector efficiency. A number of measurements of the

Table 6.2: Silicon γ as a fraction of the total measured 478 keV signal for each running configuration.

Detector - collimation	Si γ fraction ($\times 10^{-2}$)	ϵ_0^{AG} correction
T-7	1.1715(9)	0.988284(9)
T-8	1.1995(6)	0.988005(6)
T-10	1.2044(5)	0.987956(5)
B-7	1.3235(18)	0.986765(18)
B-8	1.2145(7)	0.987851(7)
B-10	1.2450(7)	0.987550(7)

silicon gamma-ray background were performed over the course of the calibration data. The correction for each set of data is shown in table 6.2.

In addition to neutron interaction in the Si substrate, gamma interactions also occur. ^{10}B capture gamma rays originate from the front face of the target, and must travel through the 0.4 mm silicon backing to reach the top gamma detector. A simple calculation using XCOM cross sections [Berger et al., 2010] and a beam simulation to determine average gamma path length in the material shows that approximately 1 % of the gamma rays scatter in the Si backing. A measurement is needed to determine the corrections to sufficient precision. In this measurement, the gamma rate in the top detector is measured with some number of Si backings behind the target foil. The measurement is performed at several different numbers of backing wafers, and the gamma attenuation per unit length in silicon is determined. The thicker thick target was used for this measurement to accumulate the necessary statistics in reasonable time. Measurements were performed with 0, 3, and 5 silicon foils. The slope is determined from a fit to a line, establishing the gamma attenuation per unit length. The results are shown in figure 6.1. To correct for this effect, a multiplicative correction factor of 1.01267(24) is applied to all flux monitor efficiencies from the top detector data.

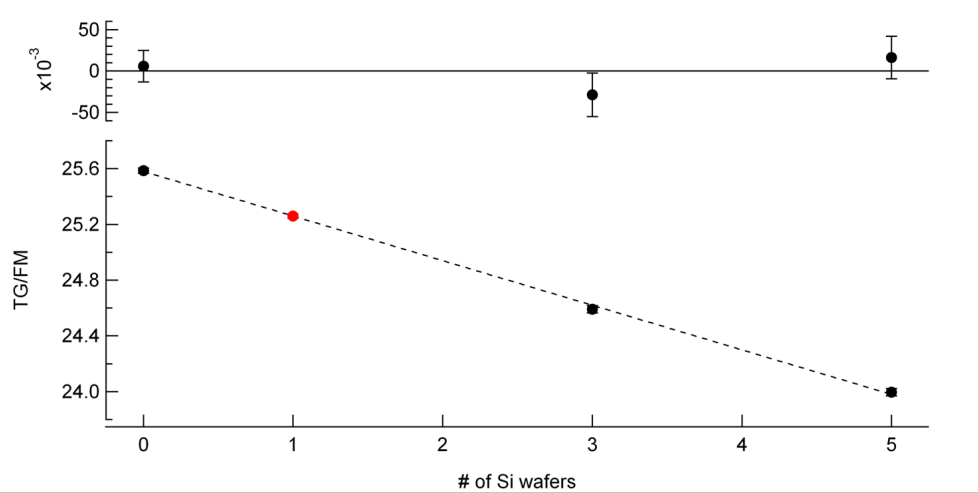


Figure 6.1: A plot of the ratio Tγ/FM versus number of silicon wafers stacked behind the ^{10}B target. The data is fit to a line to extract the slope. The residuals are shown in the upper plot.

6.3 Corrections to Thick Target Data

A thin (0.32 mm), self-supporting target of highly enriched boron carbide ($^{10}B_4C$, 98 % enrichment) is sufficiently thick to stop a beam of cold neutrons (ignoring small scattering corrections (see equation 6.8), better than 0.9999 absorption). For the calibration to be correct, it is necessary to determine scattering and reaction channels that do not result in the absoption of neutrons by ^{10}B. Gamma losses not common to both the thin and thick targets must also be corrected for.

Neutron scattering from the thick target can take place in three ways: coherent scattering from crystalline regions, scattering from surface features, and incoherent scattering. Boron carbide is a ceramic and is likely polycrystalline, so Bragg scattering from the material is possible though the amount of neutrons lost to the effect is likely to be very small. This can be assessed by powder diffraction techniques. Scattering from the thicker thick target was measured on the SPINS apparatus. One Bragg peak consistent with the (101) reflection was measured (figure 6.2). The scattered fraction into this peak is approximately 2×10^{-7}, making the effect completely negligible for our calibration.

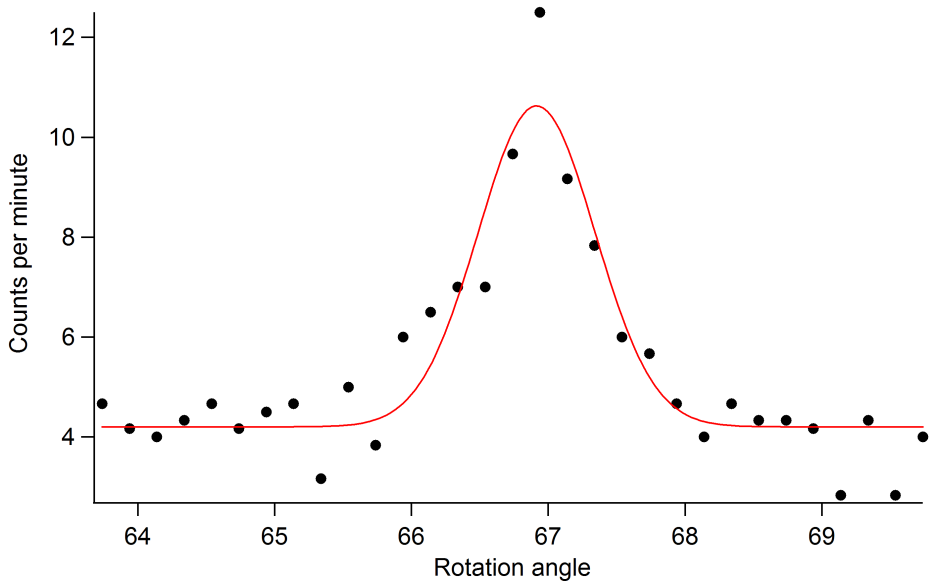


Figure 6.2: A measurement of the (101) reflection in the boron carbide target.

Surface scattering and incoherent scattering were critical issues for the solid target radiometer. A $\sim 2\pi$ backscatter detector was developed to determine the amount of scattering in the ^{6}LiPb and ^{6}LiMg targets. The apparatus consisted of a target holder and a cylindrical sheet of dysprosium with a small center hole. A tightly collimated beam passes through the hole in the dysprosium foil and strikes the target. Backscattered neutrons will absorb on the dysprosium foil, and the resulting image can be compared to a direct image of the beam to determine the scattered fraction.

A technique similar to the one employed by Chowdhuri was used to attempt to image the backscatter. The 50 mm Dy disc was placed near the alpha detector in the Alpha-Gamma device and the thinner thick target was loaded into the foil holder. The beam was turned on for an hour, and Dy was exposed to the Fuji plate for 15 minutes. No counts are seen inside the foil region after background subtraction.

Richardson approached this problem in another way in the first run of the Alpha-Gamma device. A target stack made of the thin and thick targets is loaded into the Alpha-Gamma device such that the beam is incident on the thin target first. Most of the beam passes through the thin target and interacts with the thick target.

Backscattered neutrons can pass through the thin foil and be absorbed (with varying probability depending on the path length through the boron).

This technique was used in this run of the Alpha-Gamma device. A pair of ~ 100 μg/cm^2 ^{10}B foils are used in the flux monitor and Alpha-Gamma device in order to significantly increase the observed count rate. Despite the increased thickness of the foils, they are still largely transparent to neutrons and thus appropriate for this measurement. The relevant ratio is α counts with the alpha detector in the Alpha-Gamma device to α counts with the flux monitor (α/FM). A run is performed without the thick target backing the Alpha-Gamma ^{10}B foil, and then in the second run the thick target is placed behind the Alpha-Gamma ^{10}B foil. A count rate enhancement of $(-4 \pm 6) \times 10^{-4}$ is observed. Given the magnitude of the uncertainty and the fact that the enhancement should be positive, this is interpreted as a null result. This agrees with the conclusions reached for the BN target in the Richardson experiment. Limited run time was available for accumulation of statistics, and the effect may warrant a more serious study in the future.

The incoherent scattering from the thick target is calculable. As seen in table 6.3, absorption and scattering from ^{11}B, ^{12}C, and ^{13}C are negligible. Only the ^{10}B incoherent cross section of 3.1 barns is important for the calculation. For $\sim$ 5Å neutrons, the absorption cross section is 10580(25) barns. To first order, half of the scattered neutrons will still absorb in the target. Thus, the probability of neutron loss due to scattering is given by:

$$\frac{1}{2}\frac{\sigma_{inc}}{\sigma_{abs}} \approx 1.4 \times 10^{-4} \pm 3.3 \times 10^{-7} \tag{6.8}$$

This gives an ϵ_0^{AG} correction of 0.9998582(3).

While the thick target stops virtually all neutrons that impinge upon it, there is a distribution of extinction lengths (figure 6.3). This leads to an average distance a capture gamma ray must travel in the material to reach one of the two gamma detectors. The figure demonstrates that this average distance for the bottom detector

Table 6.3: Incoherent scattering and absorption cross sections for isotopes of boron and carbon.

Isotope	Relative concentration	σ_{inc} (b)	σ_{abs} (b)
^{10}B	0.784	3	10580(25)
^{11}B	0.016	0.21	0.015
^{12}C	0.198	0	0.00974
^{13}C	0.0022	0.034	0.00378

is small but is considerable for the top detector. Our geometry does not permit us to measure the attenuation to the bottom detector, but a measurement of the gamma attenuation to the top detector is fairly straightforward. The target used in the Richardson version of Alpha-Gamma was a natural boron nitride (BN) target. Because there was only one target, it was not possible to do a direct measurement of the gamma attenuation, and instead XCOM was used. From this, an upper scattering limit of $\sim 5\,\%$ was determined. In preparation for the next version of the experiment, two targets of enriched boron carbide were obtained. These new targets offered advantages over the natural BN target. The targets were roughly 5 times thinner and thus have significantly smaller gamma attenuation corrections. Having two targets of different thicknesses permitted measurements of the gamma rate in the top detector as a function of thick target thickness. A fit to these three measurements (thinner target, thicker target, thinner + thicker target) determines the gamma attenuation per unit length in the target (figure 6.4)

A simple ray-tracing beamline simulation was developed to simulate the beam spot on the Alpha-Gamma target. For the thick target, code was added to determine the neutron penetration into the target. This allowed for calculation of the average distance a gamma ray had to travel in the target material to reach the top or bottom detector. From the experimentally determined attenuation for the top detector and the simulated gamma distance in the material for the top and bottom detectors, the attenuation to the bottom detector is determined. For our calibration data, the thinner thick target was used. The results are found in table 6.4.

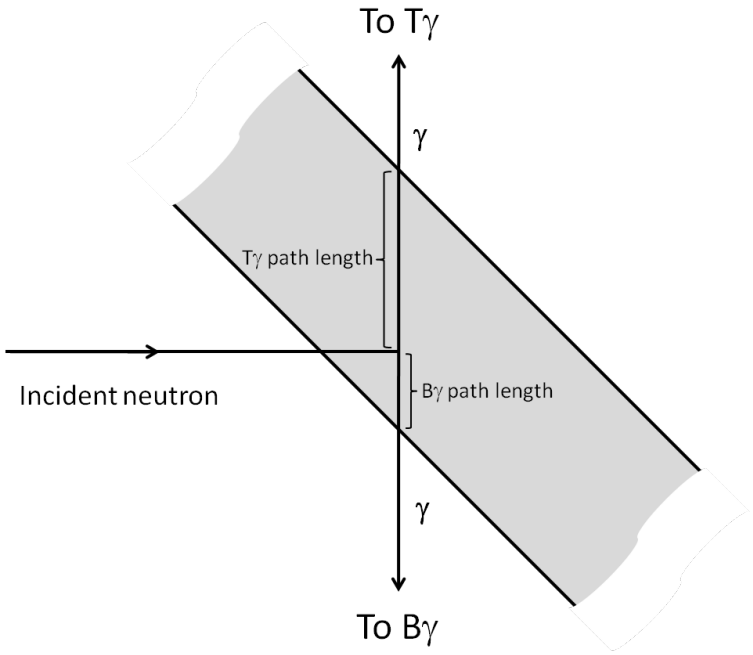


Figure 6.3: An illustration the different path lengths through the thick target. The travel distance through the target to the bottom detector is greatly exaggerated.

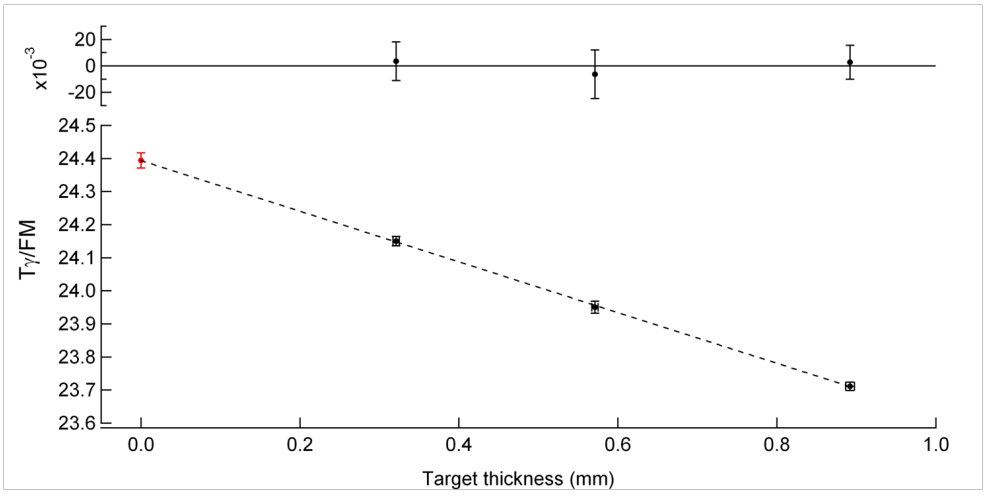


Figure 6.4: A plot of Tγ/FM for three thicknesses of B_4C (0.321 mm, 0.571 mm, and 0.892 mm). The data is fit to a line to extract the slope. The residuals are shown in the upper plot.

Table 6.4: Lost 478 keV γ due to scattering in B_4C target.

Gamma Detector	% scattered	ϵ_0^{AG} correction
Top	1.0111(45)	0.9900(4)
Bottom	0.06885(3)	0.99932(3)

The narrow collimation requirements of the experiment as well as the inherently low flux of the monochromatic beam kept signal rates at levels where dead time corrections are minimal. The only beam-related dead time correction is that of the thick target gamma signal. The signal in the 478 keV region is not particularly high ($\sim$300 s^{-1}), but one must consider the entire detected gamma rate of $\sim$ 1000 s^{-1}, which is high enough to cause $\sim$ 1 % signal loss. The pulser method is used to determine the detector dead time (more specifically, the correction for the thick target data). A precision 25 s^{-1} fixed-interval pulser is fed into the test input of both gamma detectors. The pulser peak location is chosen to be in a region of very low background. SCA windows are placed the same number of channels away from the edge of the pulser peak as they are around the boron photopeak. This distance is important - events that just barely pile-up could merely shift inside the peak region and still be counted. It is then a simple matter of taking the counts in the pulser peak region, subtracting the background, and comparing that to the known 25 s^{-1} rate of the pulser. The dead time is significant in all configurations - from 0.4 % for the 7.2 mm TG data, to 1.3 % for the 10.5 mm BG data. The rate is roughly ten times higher than that of the ^{239}Pu source, and the amplifier dead time is about three times larger. A summmary of the results is found in table 6.5.

6.4 Corrections to the Flux Monitor Data

The beam used to calibrate the neutron flux monitor is different from the beam used in the lifetime experiment in two ways: beam wavelength distribution and beam spot size. The neutron flux monitor efficiency is typically stated for thermal neutrons. To

Table 6.5: Gamma detector dead time corrections for the thick target with each collimation scheme.

Detector - C2	ϵ_0^{AG} correction
T-7	0.99533(3)
T-8	0.99339(2)
T-10	0.99006(4)
B-7	0.99441(10)
B-8	0.99201(7)
B-10	0.98800(11)

Table 6.6: Flux monitor solid angle corrections for the three calibration configurations.

Collimation	$\bar{\Omega}$ (units of 4π)	ϵ_0^{AG} correction
15/7	0.00420477	1.00043(16)
15/8	0.00420394	1.00062(10)
15/10	0.00420336	1.00076(20)

compare our measured flux monitor efficiency to the calculated efficiency, a correction factor of $\frac{\lambda_0}{\lambda} = 1.798/4.9605$ is applied, where λ_0 is the thermal neutron wavelength and λ is the measured wavelength of NG6m.

The beam spot incident on the neutron flux monitor is dependent on the upstream collimation choice. The neutron flux monitor efficiency stated in the lifetime paper is the center point efficiency, so a solid angle correction for the difference in solid angle between an extended beam spot and an infinitely narrow beam must be made. The design of the detector is such that the solid angle to points on the foil falls off very slowly about the center (figure 6.5), but small corrections between the three beam sizes used must be made. The dysprosium beam imaging technique is used again here. Beam images of the three collimations are shown in figure 6.6, and the average solid angle ($\bar{\Omega}$) is found using equation 6.7. The average solid angles and the corrections to the flux monitor efficiency are found in table 6.6.

It was anticipated that neutron scattering and absorption in the substrate for the neutron flux monitor foil would affect the observed rate in the monitor as well as

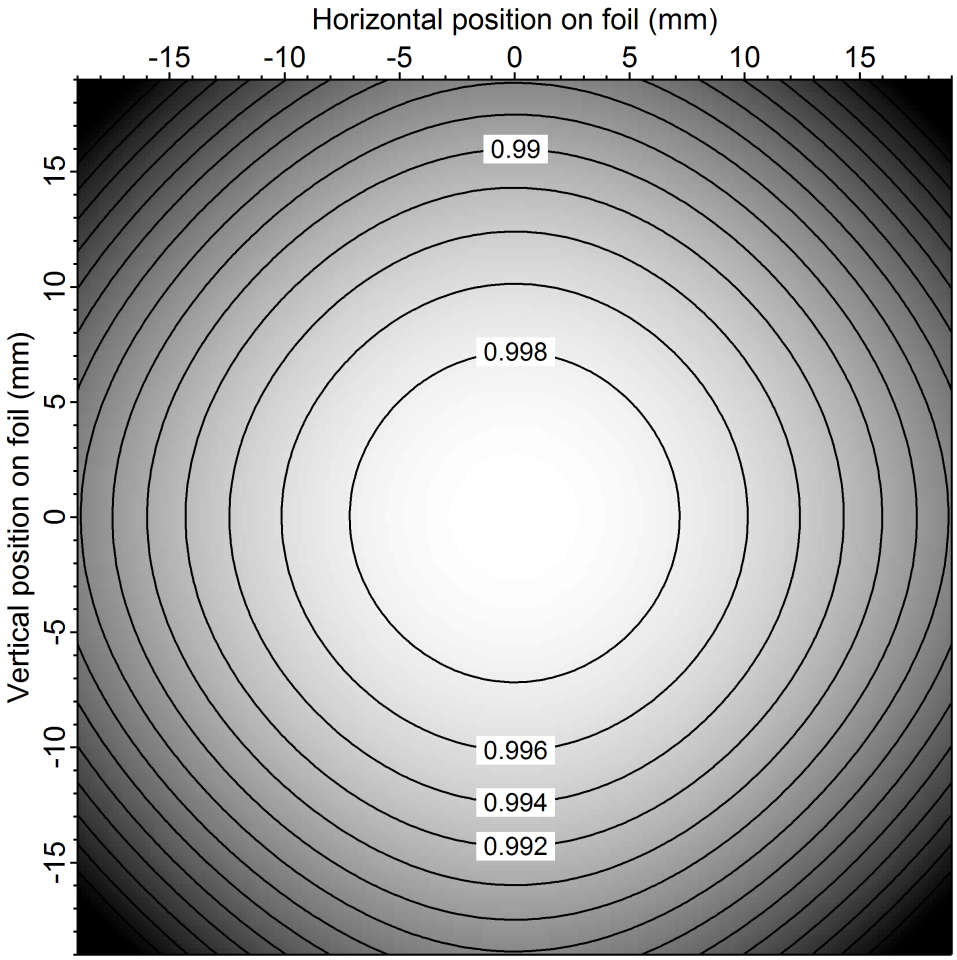
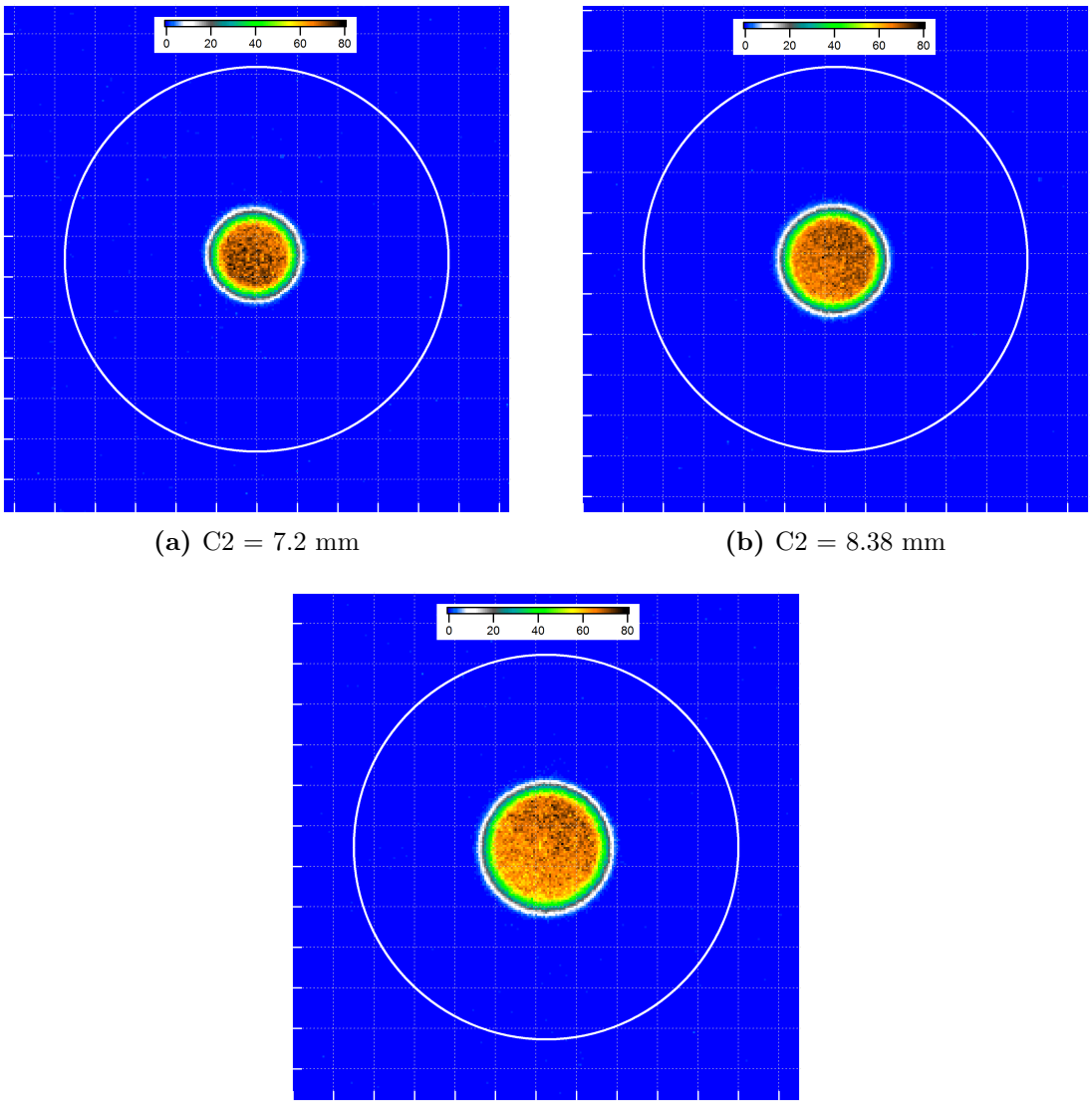


Figure 6.5: Solid angle as a function of position on the flux monitor foil



(a) C2 = 7.2 mm

(b) C2 = 8.38 mm

(c) C2 = 10.5 mm

Figure 6.6: Beam images at the flux monitor foil location with C1 = 15 mm and C2 = 7.2, 8.38, and 10.5 mm. The grid spacing is 4 mm. The white circle corresponds to the edge of the active area of the ^{6}Li foil.

alter the downstream flux. Perfect-crystal silicon wafer substrates are used in order to minimize neutron scattering in the substrate. Measurements of this scattering were performed for deposits of different subtrates (gold, aluminum, steel, silicon) and in all cases, the scattering was considerable [Scott et al., 1995]. This was something of a surprise for silicon, as the bulk scattering should be limited to Bragg scattering. A plausible explanation is that the scattering is occuring at the surfaces of the wafer, where neutrons may scatter from defects or damage. Only the evaporation surface of the wafer is mirror-polished, making it the most likely scattering candidate. Measuring this scattering probability and the resulting effects on the measured neutron flux were critical for the neutron lifetime experiment. As illustrated in figure 6.7, the neutron lifetime experiment and the Alpha-Gamma experiment orient the neutron flux monitor in opposite directions. While the two orientations depend on the same scattering parameters, they behave differently. A new measurement of the effect was desirable.

In the neutron lifetime experiment configuration, the neutron flux monitor was oriented such that the neutron beam struck the Si backing of the ^{6}Li foil first. This configuration has neutron scattering from the Si backing before the neutrons are absorbed by ^{6}Li. Backscattered neutrons go undetected, and some fraction of forward scattered neutrons will pass through the target. These scattered neutrons will pass through the ^{6}Li deposit at non-zero angles with respect to normal incidence. The path length will be increased by an average factor of f, which increases the probability of absorption for these neutrons. To correct for these effects, a measurement of the probability of scatter in silicon (ϵ_{Si}) is made. The neutron loss due to interaction in silicon (η_{Si}) is given by:

$$\eta_{Si} = \epsilon_{abs} + \left(\frac{1}{2}\right)\epsilon_{Si} \tag{6.9}$$

where ϵ_{abs} is the probability of absorption in silicon. The relative enhancement of forward scattered neutrons leads to a small increase in the detected rate. The observed

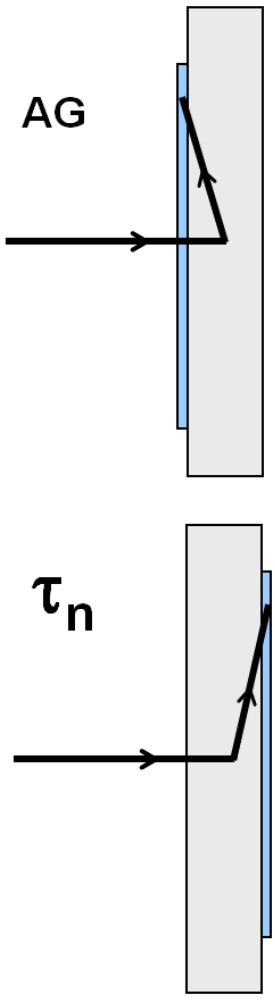


Figure 6.7: An illustration of how neutron scattering affects the two orientations of the neutron flux monitor target foil

flux monitor rate R_{obs} compared to the true rate R is given by:

$$\frac{R_{\text{obs}}}{R} = 1 - \eta_{Si} + f\frac{\epsilon_{Si}}{2} \tag{6.10}$$

The enhancement was determined as part of the campaign to produce and characterize the ^{6}Li and ^{10}B foils for the lifetime experiment. This ancillary experiment was performed at the IRMM with a beam of neutrons from the thermal column of a graphite-moderated reactor. The deposit faced the beam, and the reaction rate was measured as a function of additional backing silicon wafers behind the target foil. Neutrons pass through the ^{6}Li deposit and can backscatter off the silicon substrate and potentially interact with the ^{6}Li. This leads to an observed count rate that is higher than the true count rate and a loss of neutrons downstream. The known geometry allows for a calculation of $f(i)$ (where i is the number of wafers, $i = 1$ corresponds to the deposit foil alone) for each wafer configuration, which is then used along with the observed rate ($R(i)$) to determine ϵ_{Si} from the following equation:

$$R(i) = a\left(1 + \frac{f(i)}{2} i\epsilon_{Si}\right) \tag{6.11}$$

where a is fit parameter. This data is found in figure 6.8, and a result of $\epsilon_{Si} = (5.7 \pm 1.4) \times 10^{-4}$ is found. This ϵ_{Si} value is also used to correct for upstream scattering in additional silicon foils in the lifetime experiment.

The neutron flux monitor calibration setup mirrors the IRMM setup. In normal operation, the ratio of the observed flux monitor rate to the true rate is given by:

$$\frac{R_{\text{FM}}}{R} = 1 + f\frac{\epsilon_{Si}}{2} \tag{6.12}$$

and the downstream rate R_{AG} ratio to the true rate is:

$$\frac{R_{\text{AG}}}{R} = 1 - (\epsilon_{Si} + \epsilon_{abs}) \tag{6.13}$$

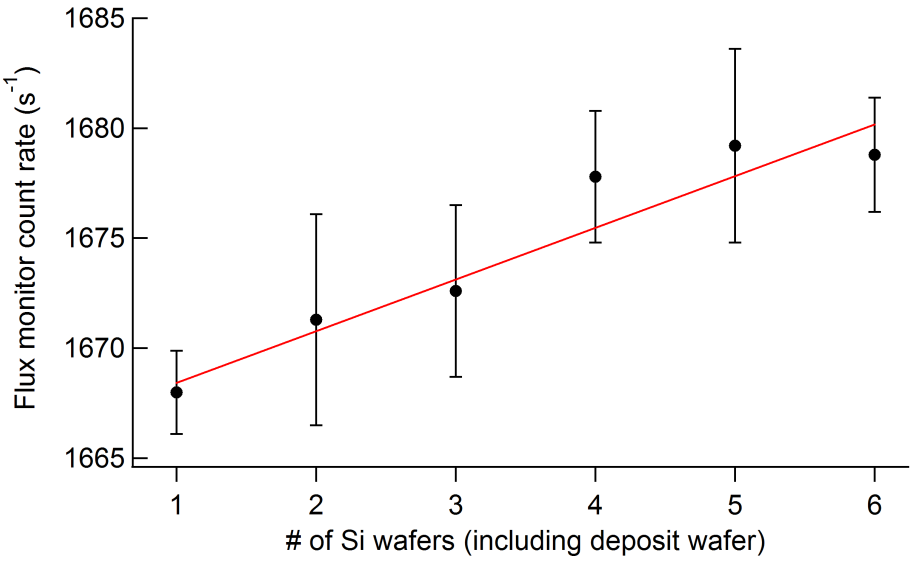


Figure 6.8: The measured enhancement from forward scattered neutrons in the IRMM experiment [Scott et al., 1995].

Because the effect was anticipated to be very small, the high mass ^{10}B foils used in our B_4C scattering measurement are used here. The ^{10}B cross section is roughly four times larger, and the measured effect is (to first order) only dependent on the substrate, which is identical to that of the lifetime target. Silicon foils are then stacked behind the flux monitor target and the ratio of alpha rate in the flux monitor to Alpha-Gamma device is measured. From equations 6.11 and 6.13 we can express this ratio:

$$\frac{R_{\mathrm{AG}}}{R}(i) = a\frac{1-(\epsilon_{Si}+\epsilon_{abs})i}{\left(1+\frac{f(i)}{2}i\epsilon_{Si}\right)} \tag{6.14}$$

The neutron absorption term is well known ($\epsilon_{abs} = 0.009$) and $f(i)$ is calculated from the known geometry of the setup. A fit to the data shown in figure 6.9 yields $\epsilon_{Si} = (9.2 \pm 1.8) \times 10^{-5}$. This corresponds to a $(2.2 \pm 0.4) \times 10^{-4}$ enhancement in the flux monitor rate and a total neutron attenuation of $\epsilon_{Si} + \epsilon_{abs} = (1.0 \pm 0.2) \times 10^{-4}$. The results from our measurements are found in table 6.7.

The two experiments arrive at contradictory conclusions - ϵ_{Si} is measured to be roughly five times larger in the IRMM measurements, leading to an enhancement term

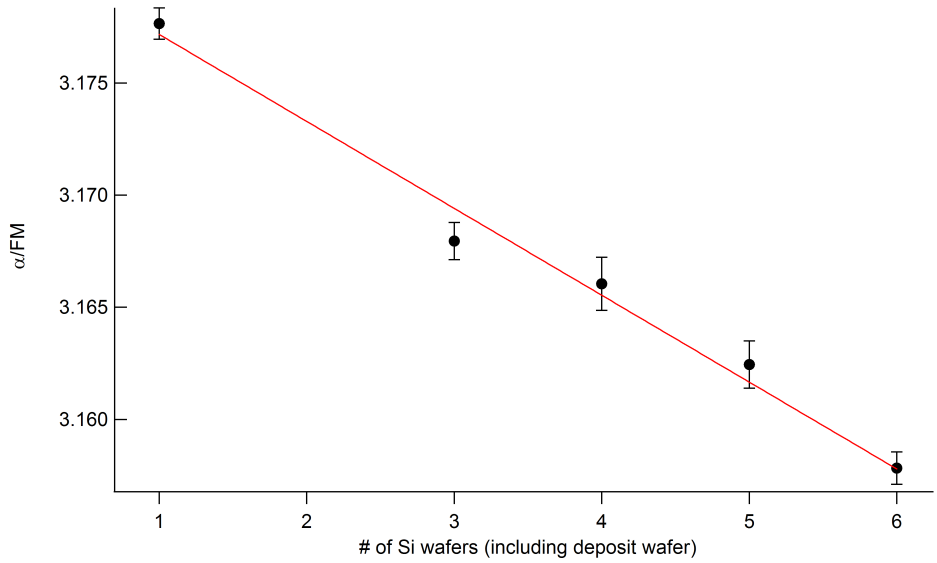


Figure 6.9: A fit of α/FM to equation 6.13 is used to determine ϵ_{Si} from the data.

Table 6.7: A summary of the corrections from neutron backscattering in the flux monitor target.

Effect	ϵ_0^{AG} correction
Neutron absorption and scattering in silicon substrate	0.99900(2)
Flux monitor signal enhancement from neutron backscatter	0.99978(4)

five times larger. It is believed that this discrepancy is coming from the differences in the beams used to measure the effect. Surface defects could lead to polycrystalline regions on the surface of the substrate. The Bragg reflection off these defects would be beam dependent. A polychromatic beam (such as the thermal beam used at the IRMM) would have more of its neutrons satisfy the Bragg condition than a monochromatic beam. Ultimately, this correction must come from measurements of the enhancement factor on the beam in which the calibration is taking place. Thus, despite the discrepancy, we are confident that our measured ϵ_{Si} is correct.

The final correction to the flux monitor data is to correct the observed response of the detector to an idealized form used in the lifetime experiment. The quoted flux monitor efficiency in the lifetime experiment is the thermal neutron efficiency of an infinitely thin foil of average areal density $\bar{\rho} = 39.300(98)$ μg/cm^2. This target will

absorb a fraction η_i of an infinitely narrow monochromatic thermal neutron beam:

$$\eta_i = \frac{N_A}{A}\rho(0,0)\sigma_0 \tag{6.15}$$

where $\rho(0,0)$ is found from equation 6.6:

$$\rho(0,0) = \bar{\rho}\frac{1}{1-\frac{0.005}{2}} \approx 39.398(98)\mu\text{g/cm}^2 \tag{6.16}$$

The true response η_t of the foil is given by

$$\eta_t = 1 - e^{-(\frac{N_A}{A}\rho(0,0)\sigma_0)} \tag{6.17}$$

To correct for this self-shielding effect, the efficiency (which has been corrected to the efficiency for an infinitely thin beam of thermal neutrons) is multiplied by the ratio of the two responses:

$$\frac{\eta_i}{\eta_t} = 1.005116(6) \tag{6.18}$$

Chapter 7

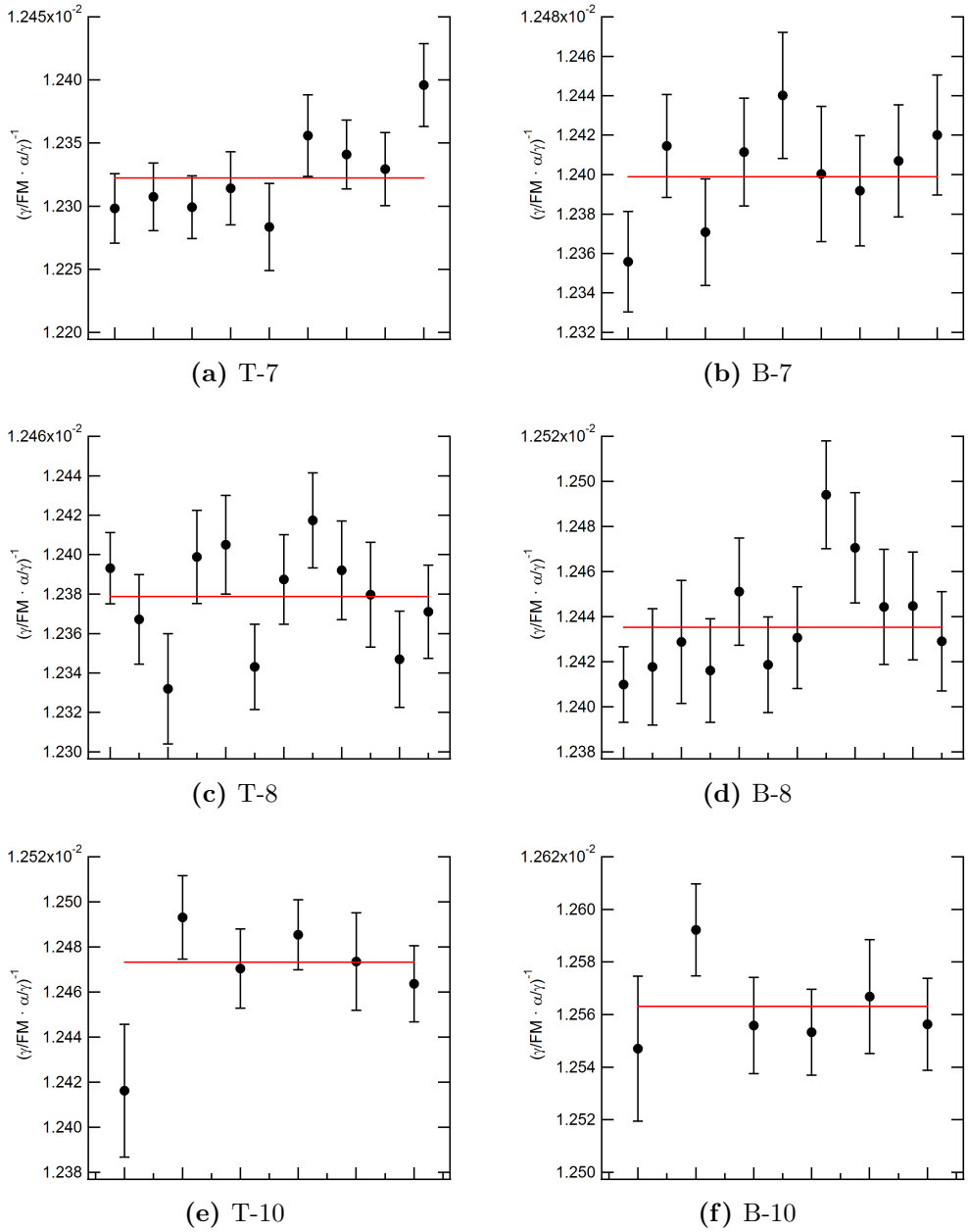
Results

Approximately 4 reactor cycles (152 days) of calibration data were taken using three different downstream collimators. By applying the corrections listed in chapter 6, six values of ϵ_0^{AG} (three collimators, two detectors) are established. A statistical combination of these efficiencies determines the final result.

7.1 Neutron Flux Monitor Efficiency Result

The data used for the neutron flux monitor calibration was taken from June 2010 to December 2010. The statistical accumulation was broken up into three data sets based on downstream collimator. As shown in chapter 6, using several beam sizes allows us to investigate solid angle and dead time effects. Table 7.1 shows the run schedule. Twelve calibrations were performed with the 8.38 mm C2, six with the 10.5 mm C2, and nine with the 7.2 mm C2. The intention was to perform the bulk of our statistical accumulation with the optimal collimation choice (8.38 mm), achieve similar statistical precision with the large collimator (the higher rate gave us higher statistical precision per run, hence the shorter run period), and spend the remainder of the budgeted reactor time for statistical accumulation on a smaller collimator.

The kernel of each efficiency measurement (and the part that can be statistically combined) is the quantity $(\gamma/FM \cdot \alpha/\gamma)^{-1}$. Figure 7.1 shows this data for each



(a) T-7 **(b)** B-7

(c) T-8 **(d)** B-8

(e) T-10 **(f)** B-10

Figure 7.1: Plots of the results of the analysis for $\frac{1}{\gamma \mathrm{FM}} \frac{1}{\alpha/\gamma}$ for the six detector-collimation configurations.

Table 7.1: Run schedule for statistical accumulation.

Timeframe	C1 / C2 configuration	Number of runs
6/12/2010 - 8/18/2010	15/8	12
8/19/2010 - 10/3/2010	15/10	6
10/4/2010 - 12/15/2010	15/7	9

Table 7.2: $\frac{1}{\gamma/\mathrm{FM}}\frac{1}{\alpha/\gamma}$ values for each detector-collimation pair.

Detector - collimation	$\frac{1}{\gamma/\mathrm{FM}}\frac{1}{\alpha/\gamma}$	χ^2/dof
T-7	0.012323(11)	0.66
T-8	0.012379(7)	1.20
T-10	0.012483(9)	1.25
B-7	0.012399(9)	0.98
B-8	0.012435(7)	1.20
B-10	0.012563(8)	0.80

collimation with the top and bottom gamma detectors. The red lines are weighted constant fits to each data set. The results are presented numerically in table 7.2 along with and the χ^2 per degree of freedom. To determine the efficiency ϵ_0^{AG} from each of the six sets of data, $(\gamma/FM \cdot \alpha/\gamma)^{-1}$ is multiplied by the Alpha-Gamma alpha detector solid angle Ω_α, the ratio of thermal neutron wavelength to beam wavelength $\frac{\lambda_0}{\lambda}$, and the eleven corrections listed in tables 7.3:

$$\epsilon_0^{\mathrm{AG}} = \left(\frac{1}{\gamma/\mathrm{FM}}\frac{1}{\alpha/\gamma}\right)\Omega_\alpha\frac{\lambda_0}{\lambda}\prod_{j=1}^{11}c_j \tag{7.1}$$

The efficiencies and statistical uncertainties for each of the six configurations are shown in table 7.4. A weighted constant fit to the six efficiences (shown in figure 7.2) is used to determine the final efficiency. From the fit, we have $\epsilon_0^{\mathrm{AG}} = 3.1116(9) \times 10^{-5}$ (statistical uncertainly only) with a $\chi^2 = 0.71$ per degree of freedom. This 2.7×10^{-4} statistical uncertainty must be combined in quadrature with the uncertainties associated with Ω_α, $\frac{\lambda_0}{\lambda}$, and the c_j corrections. Each uncertainty was generated by allowing the associated correction to vary by its uncertainty with a gaussian-weighted

randomizer. Each throw of the uncertainty creates a new set of six ϵ_0^{AG} values, which are then fit to a constant, with weighting provided by the statistical uncertainty on each point. By repeating the process many times, the uncertainty can be extracted from the standard deviation in the final ϵ_0^{AG} values. The full uncertainty budget for the experiment is shown in table 7.5. The total uncertainty of the neutron flux monitor efficiency is 5.2×10^{-4}, giving us a final value of $\epsilon_0^{\mathrm{AG}} = 3.1116(16) \times 10^{-5}$.

Table 7.3: Table of corrections for ϵ_0^{AG} data.

Correction	T-7	T-8	T-10	B-7	B-8	B-10
Si γ production	0.98828(1)	0.98800(1)	0.98796(1)	0.98676(1)	0.98785(1)	0.98755(1)
Si γ attenuation	1.01267(24)	1.01267(24)	1.01267(24)	1	1	1
B_4C γ attenuation	0.9900(4)	0.9900(4)	0.9900(4)	0.99932(5)	0.99932(5)	0.99932(5)
Dead time	0.99533(3)	0.99339(2)	0.99006(4)	0.99441(10)	0.99201(7)	0.98800(11)
AG α Ω	0.99272(6)	0.9895(2)	0.9847(7)	0.99272(6)	0.9895(2)	0.9847(7)
Surface scatter from B_4C	0.9998582(3)	0.9998582(3)	0.9998582(3)	0.9998582(3)	0.9998582(3)	0.9998582(3)
n absorption by ^{6}Li	0.989836(12)	0.989836(12)	0.989836(12)	0.989836(12)	0.989836(12)	0.989836(12)
FM enh. from n backscatter	0.99978(4)	0.99978(4)	0.99978(4)	0.99978(4)	0.99978(4)	0.99978(4)
n loss in FM foil substrate	0.99900(2)	0.99900(2)	0.99900(2)	0.99900(2)	0.99900(2)	0.99900(2)
FM $\alpha + \mathrm{t}$ Ω	1.00043(16)	1.00062(10)	1.00076(20)	1.00043(16)	1.00062(10)	1.00076(20)
Self-shielding of ^{6}Li deposit	1.005116(6)	1.005116(6)	1.005116(6)	1.005116(6)	1.005116(6)	1.005116(6)

Table 7.4: ϵ_0^{AG} values for each collimation.

Detector - C2	ϵ_0^{AG} $(\times 10^{-5})$
T-7	3.1126(27)
T-8	3.1104(19)
T-10	3.1111(24)
B-7	3.1141(24)
B-8	3.1097(18)
B-10	3.1133(19)

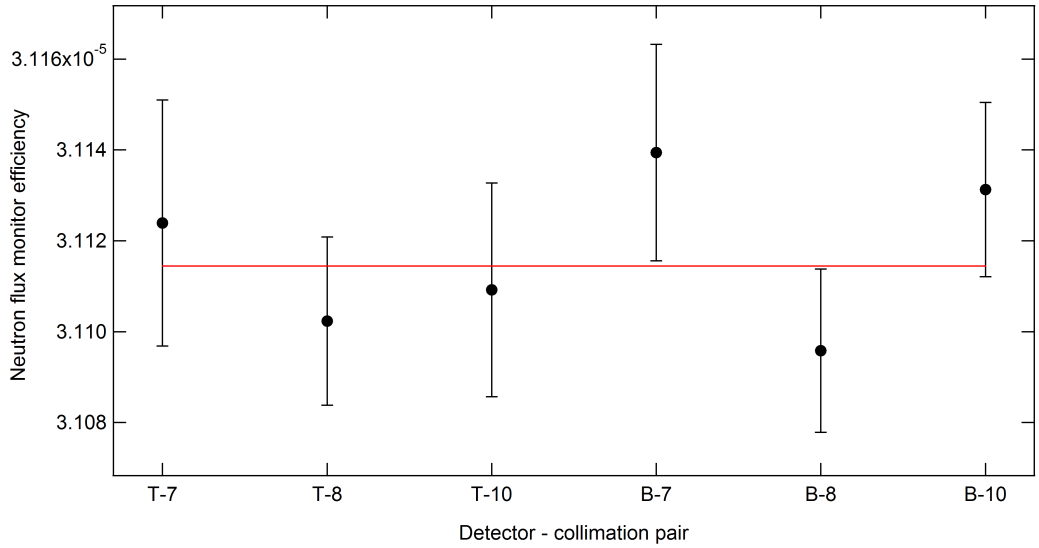


Figure 7.2: A plot of ϵ_0^{AG} for each collimation-detector pair. Only statistical uncertainty is shown. The red line is a weighted constant fit to the data.

Table 7.5: Final uncertainties from the Alpha-Gamma experiment listed largest to smallest.

Source of correction	Uncertainty (fractional)
α-source determined solid angle in Alpha-Gamma device	3.2×10^{-4}
Gamma-ray attenuation by thick target	2.0×10^{-4}
Alpha Gamma beam spot solid angle to alpha detector	1.7×10^{-4}
Gamma-ray attenuation by the thin target	1.1×10^{-4}
Neutron beam wavelength	9.7×10^{-5}
Neutron flux monitor beam spot solid angle	6.3×10^{-5}
Flux monitor enhancement from neutron backscatter	4.0×10^{-5}
Gamma detector dead time	3.1×10^{-5}
Neutron loss in FM foil substrate	1.8×10^{-5}
Neutron absorption by ^{6}Li	1.2×10^{-5}
Self-shielding of ^{6}Li deposit	6.0×10^{-6}
Gamma-ray signal from absorption in thin target substrate	3.5×10^{-6}
Surface scatter from B_4C	3.3×10^{-7}
Neutron counting statistics	2.7×10^{-4}
Total	5.2×10^{-4}

Chapter 8

Conclusion

This dissertation describes the first successful absolute calibration of a neutron flux monitor used in the NIST in-beam neutron lifetime measurement. The final result is $\epsilon_0^{\mathrm{AG}} = 3.1116(16) \times 10^{-5}$, a measurement with 0.052 % relative uncertainty. In this chapter, the future of the Alpha-Gamma device is discussed, and the possibility of re-evaluating the lifetime value and measuring the ^{6}Li thermal neutron cross section is considered.

8.1 The Future of the Alpha-Gamma Device

By achieving a 0.052 % calibration of the neutron flux monitor, the Alpha-Gamma device has exceeded its design goal. It is conceivable that the largest sources of uncertainty could be reduced further. The three largest sources of uncertainty are the gamma-ray attenuation in B_4C, the α-source determined solid angle for the Alpha-Gamma alpha detector, and beam image determination of the Alpha-Gamma alpha detector solid angle.

The limiting factor in the determination of the gamma-ray attenuation in B_4C was the ability to measure the thickness of the targets. The thickness was determined by several caliper measurements around the outer edge of each target. Significant improvements should be expected by moving to more advanced metrology techniques.

The NIST group has purchased a metrology microscope that can be used to better determine the thickness.

Metrology is also central to a better determination of the α-source determined solid angle. The limiting factor is the uncertainty in the solid angle of the counting stack used to calibrate the α-source. The stack height and aperture diameter have comparable uncertainties, so both must be reduced. The aperture is known to be slightly eccentric, and in the next source calibration it will likely be switched out for an aperture of similar craftsmanship but with a more circular shape. Again, the metrology microscope will play an important role. It was acquired after the last α-source calibration, and will certainly be used in the next campaign.

It is difficult to imagine substantially improving the beam image solid angle technique. Extra care can be taken to prepare the images in a dark environment, which reduces background and improves uniformity. Image blooming might be addressed by performing mulitple exposures for different times on one plate and extrapolating to zero exposure time. The "galaxy" effect is inherent to the technique. The most likely avenue for improving this measurement is simply to do more of them. The uncertainty on this measurement is largely driven by the determination of the C2 = 10.5 mm solid angle, which had a large uncertainty due to a large point spread in the results. Only two to three images were taken for each beam configuration, and adding to that total would likely have the largest impact on the overall uncertainty.

The Alpha-Gamma device will see further use even if no improvements to the uncertainty are made. Ideally, the Alpha-Gamma device will run in parallel with a re-run of the lifetime experiment (section 8.2. It also introduces an additional systematic check by allowing the lifetime measurement to be performed with a variety of ^{6}Li (and perhaps ^{10}B) foils. Two flux monitor rigs were constructed so that a flux monitor calibration with one foil can be taking place with the Alpha-Gamma device while the other flux monitor is in operation on the lifetime experiment.

The Alpha-Gamma device will, indirectly, be used to recalibrate NBS-1 - the national neutron standard [Gilliam et al., 2008]. NBS-1 is used as a comparison

standard for calibrating commercial neutron sources with the manganese sulfate bath technique [Adams, 2004]. As such, the uncertainty in the calibration of NBS-1 sets a lower limit for the uncertainty in any source calibrated at NIST. Absolute calibration of NBS-1 is sufficiently difficult that it has not been done for over forty years. The calibrated neutron flux monitor combined with a monochromatic beam functions as a calibrated neutron source. The beam can then be used to determine the absolute efficiency of a manganese bath The calibrated bath can then be used to re-calibrate NBS-1.

8.2 Prospects for Re-evaluating the Neutron Lifetime and ^{6}Li Cross Section

It is interesting to compare the measured flux monitor efficiency ($\epsilon_0^{\mathrm{AG}} = 3.1116(16) \times 10^{-5}$) with the value used in the neutron lifetime experiment (ϵ_0). The flux monitor efficiency was calculated from the value for $\rho(0,0)$ found in equation 6.16, $\Omega(0,0) = 4.196(4) \times 10^{-3}$, and $\sigma_0 = 941.0(13)$ b:

$$\epsilon_0 = 2\frac{N_A}{A}\Omega(0,0)\rho(0,0)\sigma_0 = 3.1148(94) \times 10^{-5} \tag{8.1}$$

The calculated flux monitor efficiency agrees with the calibration result. While it is reassuring to see, it is insufficient evidence to simply substitute in the new efficiency to re-evaluate the lifetime value. It is possible that one or both of the measured quantities (Ω, ρ) have changed since the experiment ran and any correction to the lifetime must account for these changes. It has been decided by the collaboration that we will not publish a new lifetime value from this work until we have verified that any changes to Ω and ρ are tractable.

It is believed that the ^{6}Li foils are not degrading over time, but demonstrating it is very difficult to do. The activity of the ^{6}Li and ^{10}B foils have been compared to a beam monitor at the NCNR thermal column. These measurements were performed

Table 8.1: Information about additional ^{6}Li foils calibrated with the Alpha-Gamma device.

Foil name	Areal density (μg/cm^2)	Number of ϵ measurements
Li930118-H6	19.90	2
Li930119-H5	28.55	4

Table 8.2: Foil density-dependent correction values for Li930118-H6 and Li930119-H5.

Correction	Li930118-H6	Li930119-H5
n absorption by ^{6}Li	0.994851(9)	0.99258(1)
Self-shielding of ^{6}Li deposit	1.002583(5)	1.003725(5)

twice several years apart to check for long-term material loss. The results suggest that some ^{10}B foils suffered $\sim 1\,\%$ material loss, but no statistically significant loss occurred in the ^{6}Li foils [Lamaze, 2010].

Another approach to check foil stability is to calibrate additional ^{6}Li deposits. The NIST group owns two lighter ^{6}Li deposits from the same evaporation campaign. The foil names, areal densities, and number of measurements performed are found in table 8.1. Foil Li930119-H5 was used extensively in the testing of the final two radiometer experiments. Foil Li930118-H6 was used in early testing with the Alpha-Gamma device. Approximately 3 weeks of reactor time were spent measuring the efficiency of these two foils. The same corrections used in table 7.3 apply here as well, except for those related to the foil mass (listed in table 8.2). The efficiency results are shown alongside the calculated values in table 8.3. The agreement between the measured and calculated efficiencies is suggestive but is not conclusive. The three foils have experienced similar environments over the last eighteen years, so it is possible that all three foils are degrading in proportion to one another. It is likely that one of the foils will need to be destructively analyzed by IDMS to make a definitive statement on this issue. Alternatively, a new foil of well-measured mass could be used to calibrate the masses of the NIST targets by reaction rate comparison.

Table 8.3: Efficiency results for Li930118-H6 and Li930119-H5.

Foil name	Measured efficiency ($\times 10^{-5}$)	Calculated efficiency ($\times 10^{-5}$)
Li930118-H6	1.5722(28)	1.5770(48)
Li930119-H5	2.2663(32)	2.2630(69)

The detector solid angle must also be assessed. The solid angle used in the experiment was from a contacting metrology measurement in 1998. Subsequent measurements were performed with the α-source method. A new campaign of α-source and contact metrology measurements is necessary. If the solid angle has changed, it is important to establish when the change occurred. Even if any potential solid angle change is tractable, the possibility of foil degradation limits our ability to establish a lifetime result using the new efficiency. However, it is clear that the foil mass could not have increased after fabrication. This allows us to say with certainty that the measured efficiency establishes a lower limit on what the efficiency of the detector could have been during the lifetime experiment. A lower limit on the efficiency provides an upper limit on the neutron lifetime. Further investigation into the foil mass and solid angle issues is necessary before such a limit can be produced.

If ^{6}Li and ^{10}B foils of known mass can be obtained or the existing foils can be re-measured, it opens up the possiblity to measure the two cross sections to unprecedented precision [Nico et al., 2008]. This is of considerable value to the nuclear data and reactor dosimetry communities. The ^{6}Li(n,t) and ^{10}B(n,α) thermal neutron cross sections are standard cross sections used to normalize other measured cross sections to absolute values. It is essential that they are accurate. Provided that a well-prepared foil could be fabricated, the technique can be applied to any element with reaction products that can be measured with PIPS detectors.

While an improved result from the 2000 run of the lifetime experiment would be of significant value, a re-run of the experiment with the newly calibrated flux monitor is ultimate goal [Dewey et al., 2009]. The success of the calibration removes the largest barrier to completing a $\sim$ 1 s measurement. A projected uncertainty

budget is found in table 8.4. The neutron flux monitor efficiency now contributes an uncertainty of 0.5 s to the neutron lifetime. The next two largest sources of uncertainty in the previous lifetime were lost protons due to the neutron beam halo and magnetic field nonlinearity issues when the experiment was run with at the largest proton trap size. Both effects can be eliminated. The issue of neutron beam halo has been addressed in experiments making use of the same proton detection system by simply using a larger surface barrier detector [Nico et al., 2006]. The issue of trap nonlinearity is addressed by operating the proton trap at nine electrodes instead of ten. A proton counting statistical uncertainty of 0.5 s can be achieved in reasonable running time [Nico, 2011]. The net effect of these efforts would be a 1.3 s measurement of the neutron lifetime. Such a measurement would be competitive with the most precise UCN lifetime experiments and improve the state of the art in beam lifetime experiments by nearly a factor of three. A re-run of the beam lifetime experiment (with the improvements made in this dissertation) has been identified as a high-priority experiment in fundamental neutron physics by the Nuclear Science Advisory Committee [Kumar, 2011]. It is hoped that the lifetime experiment will run again at NIST in the near future.

Table 8.4: Projected uncertainty budget for a new run of the beam lifetime experiment.

Source of correction	Uncertainty (s)
Neutron flux monitor efficiency	0.5
Absorption of neutrons by ^{6}Li	0.8
Neutron beam profile and detector solid angle	0.1
Neutron beam profile and ^{6}Li deposit shape	0.1
Absorption of neutrons by Si substrate	0.1
Scattering of neutrons by Si substrate	0.5
Proton backscatter calculation	0.4
Neutron counting dead time	0.1
Proton counting statistics	0.5
Neutron counting statistics	0.1
Total	1.3

Bibliography

Bibliography

Adams, J. M. (2004). Present and future trends for neutron source calibrations at the National Institute of Standards and Technology. *Nuclear Instruments & Methods in Physics Research, Section B*, 213:218–222. 128

Alfimenkov, V. P., Nesvizhevsky, V. V., Serebrov, A. P., Strelkov, A. V., Taldaev, R. R., Kharitonov, A. G., and Shevtsov, V. N. (1992). *ZETF*, 102:740. 10, 146

Arzumanov, S., Bondarenko, L. N., Chernyavsky, S., Drexel, W., Fomin, A., Geltenbort, P., Morozov, V. I., Panin, Y. N., Pendlebury, J. M., and Schreckenbach, K. (2000). Neutron life time value measured by storing ultracold neutrons with detection of inelastically scattered neutrons. *Physics Letters B*, 483:15–22. 146

Berger, M. J., Hubbell, J. H., Seltzer, S. M., Chang, J., Coursey, J. S., Sukumar, R., Zucker, D. S., and Olsen, K. (2010). XCOM: Photon Cross Section Database (version 1.5). Available online at http://physics.nist.gov/xcom. 103

Bondarenko, L. N., Kurguzov, V. V., Prokofiev, Y. A., Rogov, E. V., and Spivak, P. E. (1978). Measurement of the neutron half-life. *JETP Letters*, 28:303–307. 7, 146

Byrne, J., Dawber, P. G., Habeck, C. G., Smidt, S. J., Spain, J. A., and Williams, A. P. (1996). A revised value for the neutron lifetime measured using a Penning trap. *Europhys. Lett.*, 33:187–192. 11, 146

Cappelletti, R. L., Glinka, C. J., Krueger, S., Lindstrom, R. A., Lynn, J. W., Prask, H. J., Prince, E., Rush, J. J., Rowe, J. M., Satija, S. K., Toby, B. H., Tsai, A., and Udovic, T. J. (2001). Material Research With Neutrons at NIST. *J. Res. Natl. Inst. Stand. Technol.*, 106:187–230. 41

Carlson, A. D. and Bhat, M. R. (1982). 1982 ENDF/B-V Cross Section Measurement Standards. Technical report, Brookhaven National Laboratory Report BNL-NCS-51619. xv, 26

Carlson, A. D. et al. (2009). 2009 International Evaluation of Neutron Cross Section Standards. *Nucl. Data Sheets*, 110:3215–3324. xv, 25, 26

Carlson, A. D., Poentiz, W. P., Hale, G. M., Peelle, R. W., Doddler, D. C., Fu, C. Y., and Mannhart, W. (1993). The ENDF/B-VI Neutron Cross Section Measurement Standards. *NIST Interagency Report*, 5177. xv, 18, 22, 26

Chadwick, J. (1932). The Existence of a Neutron. *Proc. R. Soc. Lond A*, 136:692–708. 1

Chadwick, J. and Goldhaber, M. (1934). A Nuclear Photo-effect: Disintegration of the Diplon by γ-Rays. *Nature*, 134:237–238. 1

Chadwick, J. and Goldhaber, M. (1935). The Nuclear Photoelectric Effect. *Proc. R. Soc. Lond A*, 151:479–493. 1, 6

Chowdhuri, Z. (2000). *Absolute Neutron Measurements in Neutron Decay*. PhD thesis, Indiana University. xiii, xv, 19, 29, 31

Chowdhuri, Z., Hansen, G. L., Jane, V., Keith, C. D., Lozowski, W. M., Snow, W. M., Dewey, M. S., Gilliam, D. M., Greene, G. L., Nico, J. S., and Thompson, A. K. (2003). A cryogenic radiometer for absolute neutron rate measurement. *Review of Scientific Instruments*, 74:4280–4293. 28, 31

Christensen, C. J., Nielsen, A., Bahnsen, A., Brown, W. K., and Rustad, B. M. (1972). Free-Neutron Beta-Decay Half-Life. *Physical Review D*, 5:1628–1940. 7, 146

D'Angelo, N. (1959). Cloud-Chamber Measurement of the Half-Life of the Neutron. *Physical Review*, 114:285–292. 146

Deruytter, A. J. and Pelfer, P. (1967). Precise determination of the branching ratio and Q-value of the ^{10}B(n,α)^{7}Li reaction and of the Q-value of the ^{6}Li(n,α)^{3}H. *Journal of Nuclear Energy*, 21:833–845. 32

Dewey, M. S., Coakley, K. J., Gilliam, D. M., Greene, G. L., Laptev, A. B., Nico, J. S., Snow, W. M., Wietfeldt, F. E., and Yue, A. T. (2009). Prospects for a new cold neutron beam measurement of the neutron lifetime. *Nuclear Instruments & Methods in Physics Research, Section A*, 611:189–192. 130

Dewey, M. S., Gilliam, D. M., Nico, J. S., Wietfeldt, F. E., Fei, X., Snow, W. M., Greene, G. L., Pauwels, J., Eykens, R., Lamberty, A., and VanGestel, J. (2003). Measurement of the Neutron Lifetime Using a Proton Trap. *Physical Review Letters*, 91:152302. 15

Dimeo, R. M. (2009). NCNR: A National User Facility. Presented at the 2nd International Symposium on Material Test Reactors, Idaho Falls, ID, September 28, 2009. xvi, 44

Ehzov, V. F., Andreev, A. Z., Ban, G., Bazarov, B. A., Geltenbort, P., Hartman, F. J., Glushkov, A. G., Groshev, M. G., Knyazkov, V. A., Kovrizhnykh, N. A., Naviliat-Cuncic, O., Krygin, G. B., Mueller, A., Paul, S., Picker, R., Rayabov, V. L., Serebrov, A., and Zimmer, O. (2009). Magnetic storage of UCN for a measurement of the neutron lifetime. *Nuclear Instruments & Methods in Physics Research, Section A*, 611:167–170. 10, 12

Eidelman, S. et al. (2004). Review of Particle Physics. *Physics Letters B*, 592:1+. 12

Ezhov, V. (2009). Neutron lifetime measuring using magnetic trap. Presented at the Seventh International Workshop on Cold and Ultracold Neutrons, St. Petersburg Russia, June 10, 2009. xiv, 12, 145

Fermi, E. (1934). Versuch einer Therorie der β-Strahlen I. *Z. Phys. A*, 88:161–177. 2

Fermi, E., Amaldi, E., D'Agostino, O., Rasetti, F., and Segre, E. (1934). Artificial Radioactivity Produced by Neutron Bombardment. *Proc. R. Soc. Lond A*, 146:483–500. 7

Gamow, G. and Teller, E. (1936). Selection Rules for the β-Disintegration. *Physical Review*, 49:895–899. 2

Gilliam, D. M., Denecke, B., Eykens, R., Pauwels, J., Robouch, P., Hodge, P., Hutchinson, J. M. R., and Nico, J. S. (1999). Characterization of actinide targets by low solid-angle alpha particle counting. *Nuclear Instruments & Methods in Physics Research, Section A*, 438:124–130. 90

Gilliam, D. M., Greene, G. L., and Lamaze, G. P. (1989). Absolute neutron counting based on B-10 alpha-gamma coincidence methods. *Nuclear Instruments & Methods in Physics Research, Section A*, 284:220–222. 32

Gilliam, D. M. and Lamaze, G. P. (1986). The Investigation of Fundamental Interactions with Cold Neutrons. NBS SP711, G. L. Greene, editor. 25

Gilliam, D. M., Yue, A. T., and Dewey, M. S. (2008). The use of polyimide foils to prevent contamination from self-sputtering of ^{252}Cf deposits in high-accuracy fission counting. *Nuclear Instruments & Methods in Physics Research, Section A*, 590:181–184. 100, 127

Golub, R., Richardson, D. J., and Lamoreaux, S. K. (1991). *Ultra-Cold Neutrons*. Adam Hilger. 10

Hansen, G. L. (2004). *A Radiometric Measurement of Neutron Flux in a Liquid ^{3}He Target*. PhD thesis, Indiana University. 32

Hardy, J. C., Neilson, R. G., Nelson, J. M., Iacob, V. E., Sanchez-Vega, M., and Helmer, R. G. (2002). Precise efficiency calibration of an HPGe detector: source measurements and Monte Carlo calculations with sub-percent precision. *Applied Radiation and Isotopes*, 56:65–69. 34

Hardy, J. C. and Towner, I. S. (2009). Superallowed $0^+ \longrightarrow 0^+$ nuclear beta decays: A new survey with precision tests of the conserved vector current hypothesis and the standard model. *Physical Review C*, 79:055502. 4

Jackson, J. D., Treiman, S. B., and Jr, H. W. W. (1957). Possible Tests of Time Reversal Invariance in Beta Decay. *Physical Review*, 106:517–521. 3

Kossakowski, R., Grivot, P., Liaud, P., Schreckenbach, K., and Azuelos, G. (1989). Neutron Lifetime Measurement with a Helium-Filled Time Projection Chamber. *Nuclear Physics A*, 503:473–500. 146

Kosvintsev, Y. Y., Kushnir, Y. A., Morozov, V. I., and Terekhov, G. I. (1980). The use of ultracold neutrons for measurement of the neutron lifetime. *JETP Letters*, 31:257–261. 146

Kosvintsev, Y. Y., Morozov, V. I., and Terekhov, G. I. (1986). Measurement of neutron lifetime through storage of ultracold neutrons. *JETP Letters*, 44:444–446. 146

Kumar, K. S. (2011). Neutron Subcommittee Interim Report. Presented at the Nuclear Science Advisory Committee meeting, June 30, 2011. 131

Lamaze, G. P. (2010). Private communication. 18, 129

Lamaze, G. P., Gilliam, D. M., and Williams, A. P. (1988). Prompt gamma as a fluence rate monitor in neutron beam experiments. *Journal of Radioanalytical and Nuclear Chemistry, Articles*, 123:551–559. xiii, 19, 38

Last, J., Arnold, M., Döhner, J., Dubbers, D., and Freedman, S. J. (1988). Pulsed-Beam Neutron-Lifetime Measurement. *Physical Review Letters*, 60:995–998. 146

Lopez, R. E. and Turner, M. S. (1999). Precision prediction for the big-bang abundance of primodrial ^{4}He. *Physical Review D*, 59. 5

Mampe, W., Ageron, P., Bates, C., Pendlebury, J. M., and Steyerl, A. (1989). Neutron Lifetime Measured with Stored Ultracold Neutrons. *Physical Review Letters*, 63:593–596. 10, 146

Mampe, W., Bondarenko, L. N., Morozov, V. I., and Panin, Y. N. (1993). Measuring neutron lifetime by storing ultracold neutrons and detecting inelastically scattered neutrons. *JETP Letters*, 57:77–81. 10, 146

Materne, S., Picker, R., Altarev, I., Angerer, H., Franke, B., Gutsmiedl, E., Hartmann, F. J., Müller, A. R., Paul, S., and Stoepler, R. (2009). PENeLOPE - on the way towards a new neutron lifetime experiment with magnetic storage of ultra-cold neutrons and proton extraction. *Nuclear Instruments & Methods in Physics Research, Section A*, 611:176–180. 10

Mohr, P. J., Taylor, B. N., and Newell, D. B. (2006). CODATA recommended values of the fundamental physical constants: 2006. *Reviews of Modern Physics*, 80:633–730. 71

Morozov, V. I. (1989). Neutron Lifetime Determination by Ultracold Neutron Storage. *Nuclear Instruments & Methods in Physics Research, Section A*, 284:108–110. 146

Mumm, H. P. (2005). Rebuild of the NG6 end station. Unpublished note. xvi, 46

Nakamura, K. et al. (2010). 2011 partial update for the 2012 edition. *J. Phys. G*, 37:075021. 4, 12

Nico, J. S. (2011). Apparatus improvements and experimental strategy. Presented at the Beam Lifetime Collaboration Meeting, April 29, 2011. 131

Nico, J. S., Arif, M., Dewey, M. S., Gentile, T. R., Gilliam, D. M., Huffman, P. R., Jacobson, D. L., and Thompson, A. K. (2005a). The Fundamental Neutron Physics Facilities at NIST. *J. Res. Natl. Inst. Stand. Technol.*, 110:137–144. 45

Nico, J. S., Dewey, M. S., Gentile, T. R., Mumm, H. P., Thompson, A. K., Fisher, B. M., Kremsky, I., Wietfeldt, F. E., Chupp, T. E., Cooper, R. L., Beise, E. J., Kiriluk, K. G., Byrne, J., and Coakley, K. J. (2006). Observation of the radiative decay mode of the free neutron. *Nature*, 444:1059–1062. 131

Nico, J. S., Dewey, M. S., Gilliam, D. M., Greene, G. L., Laptev, A. B., and Yue, A. T. (2008). Measuring ^{6}Li(n,t) and ^{10}B(n,α) Cross Sections using the NIST Alpha-Gamma Device. In *Proceedings, 13th ASTM-EWGRD Reactor Dosimetry Symoposium*. 130

Nico, J. S., Dewey, M. S., Gilliam, D. M., Wietfeldt, F. E., Fei, X., Snow, W. M., Greene, G. L., Pauwels, J., Eykens, R., Lamberty, A., VanGestel, J., and Scott, R. D. (2005b). Measurement of the neutron lifetime by counting trapped protons in a cold neutron beam. *Physical Review C*, 71:055502. ix, xiii, 11, 15, 26, 98, 101, 146

O'Shaughnessy, C. M., Golub, R., Schelhammer, K. W., Swank, C. M., Seo, P.-N., Huffman, P. R., Dzhosyuk, S. N., Mattoni, C. E. H., Yang, L., Doyle, J. M., Coakley, K. J., Thompson, A. K., Mumm, H. P., Lamoreaux, S. K., McKinsey, D. N., and Yang, G. (2009). Measuring the neutron lifetime using magnetically trapped neutrons. *Nuclear Instruments & Methods in Physics Research, Section A*, 611:171–175. 10

Paul, W., Anton, F., Paul, L., Paul, S., and Mampe, W. (1989). Measurement of the neutron lifetime in a magnetic storage ring. *Z. Phys. C*, 45:25–30. 9, 10, 145

Pauwels, J., Scott, R. D., Eykens, R., Robouch, P., Gestel, J. V., Verdonck, J., Gilliam, D. M., and Greene, G. L. (1995). Improvements in the preparation and areal characterization of 10B and 6LiF reference deposits. *Nuclear Instruments & Methods in Physics Research, Section A*, 362:104–111. xv, 17, 21, 22, 23, 24

Pearson, W. B. (1965). *Handbook of Lattice Spacings and Structures of Metals*. Pergamon. 30

Pichlmaier, A., Varlamov, V., Schreckenbach, K., and Geltenbort, P. (2010). Neutron lifetime measurement with the UCN trap-in-trap MAMBO II. *Physics Letters B*, 693:221–226. 12, 146

Richardson, J. M. (1993). *Accurate Determination of Thermal Neutron Flux: A Critical Step in the Measurement of the Neutron Lifetime*. PhD thesis, Harvard University. xiii, 30, 38, 91

Robson, J. M. (1951). The Radioactive Decay of the Neutron. *Physical Review*, 83:349–358. 7, 146

Rutherford, E. (1920). Nuclear Constitution of Atoms. *Proc. R. Soc. Lond A*, 97:374–400. 1

Scott, R. D., D'hondt, P., Eykens, R., Robouch, P., Reher, D. F. G., Sibbens, G., Pauwels, J., and Gilliam, D. M. (1995). The characterization of ^{10}B and ^{6}LiF reference deposits by measurement of neutron-induced charged particle reactions - a second campaign. *Nuclear Instruments & Methods in Physics Research, Section A*, 362:151–159. xix, 22, 113, 116

Serebrov, A. P. and Fomin, A. K. (2010). Neutron lifetime from a new evaluation of ultracold neutron storage experiments. *Physical Review C*, 82. 14

Serebrov, A. P., Varlamov, V., Kharitonov, A. G., Fomin, A., Pokotilovki, Y., Geltenbort, P., Butterworth, J., Krasnoschekova, I., Lasakov, M., Taldaev, R. R., Vassiljev, A., and Zherebstov, O. (2005). Measurement of the neutron lifetime using a gravitational trap and a low-temperature Fomblin coating. *Physics Letters B*, 605:72–78. 12, 146

Snell, A. H. and Miller, L. C. (1948). On the Radioactive Decay of the Neutron. *Physical Review*, 74:1217. 7

Snell, A. H., Pleasonton, F., and McCord, R. V. (1950). Radioactive Decay of the Neutron. *Physical Review*, 78:310–311. 7

Sosnovsky, A. N., Spivak, P. E., Prokoflev, Y. A., Kutikov, I. E., and Dobrinin, Y. P. (1959). Measurement of the Neutron Life-time. *Nuclear Physics*, 10:365–404. 7, 146

Spivak, P. E. (1988). *ZETF*, 94:1. 146

Spivak, P. E., Sosnovsky, A. N., Prokoflev, Y. A., and Sokolov, V. S. (1956). Investigation of Neutron Beta Decay. In *Proceedings of the International Conference on the Peaceful Uses of Atomic Energy*. 146

Stelts, M. L., Chrien, R. E., Goldhaber, M., and Kenny, M. J. (1979). Angular distributions of the ^{6}Li(n,t)^{4}He and ^{10}B(n,α)^{7}Li reactions at 2 and 24 keV. *Physical Review C*, 19:1159–1167. 32

Steyerl, A., Malik, S. S., Desai, A. M., and Kaufman, C. (2010). Surface roughness effect on ultracold neutron interaction with a wall and implications for computer simulations. *Physical Review C*, 81:055505. 10, 14

Wahba, M. (2002). On The Use of Beryllium as Thermal Neutron Filter. *Egypt J. Sol.*, 25. xvi, 59

Walstrom, P. L., Bowman, J. D., Penttila, S. I., Morris, C., and Saunders, A. (2009). A magneto-gravitational trap for absolute measurement of the ultra-cold neutron lifetime. *Nuclear Instruments & Methods in Physics Research, Section A*, 599:82–92. 10

Westcott, C. H. (1955). The specification of neutron flux and nuclear cross-sections in reactor calculations. *Journal of Nuclear Energy*, 2:59–75. 18

Wietfeldt, F. E. (2007). Measurement of the Neutron Lifetime Using a Proton Trap. Presented at the TRIUMF UCN Workshop, September 13, 2007. xv, 16

Wietfeldt, F. E. and Greene, G. L. (2011). The neutron lifetime. Accepted for publication in Reviews of Modern Physics. 145

Williams, R. E. (2007). The NIST Research Reactor and Cold Neutron Source. Presented at the NCNR Summer School on Methods and Applications of Neutron Spectroscopy, June 28, 2007. xv, 42, 43

Ziegler, J. F. (2008). Stopping Range of Ions in Matter. Computer code available at www.srim.org. 21, 37

Appendix

Appendix A

Summary of Neutron Lifetime Measurements

In this appendix, a summary of neutron lifetime measurements shown in figure 1.1 is presented. Experiments marked with a * are those used in the PDG 2004 average ($\tau_n = 885.7(8)$ s), and those marked with a † are used in the PDG 2011 average ($\tau_n = 881.5(15)$ s). See [Wietfeldt and Greene, 2011] for a current review of neutron lifetime experiments.

Table A.1: The results of the two magnetic trap neutron lifetime experiments. The result of [Ezhov, 2009] comes from conference presentations, but a final result has not been published.

Reference	Neutron lifetime (s)	Total uncertainty (s)
[Paul et al., 1989]	877	10
[Ezhov, 2009]	878.2	1.9 (stat.)

Table A.2: A compilation of published beam lifetime experiments.

Reference	Neutron lifetime (s)	Total uncertainty (s)
[Robson, 1951]	1110	220
[Spivak et al., 1956]	1040	130
[D'Angelo, 1959]	1100	160
[Sosnovsky et al., 1959]	1013	26
[Christensen et al., 1972]	918	14
[Bondarenko et al., 1978]	881	8
[Last et al., 1988]	876	21
[Spivak, 1988]*	891	9
[Kossakowski et al., 1989]	878	30
[Byrne et al., 1996]*†	889.2	4.8
[Nico et al., 2005b]*†	886.3	3.4

Table A.3: A compilation of published UCN bottle lifetime experiments.

Reference	Neutron lifetime (s)	Total uncertainty (s)
[Kosvintsev et al., 1980]	875	95
[Kosvintsev et al., 1986]	903	13
[Morozov, 1989]	893	20
[Mampe et al., 1989]*†	887.6	3.0
[Alfimenkov et al., 1992]*	888.4	3.3
[Mampe et al., 1993]*†	882.6	2.7
[Arzumanov et al., 2000]*†	885.4	0.98
[Serebrov et al., 2005]†	891	9
[Pichlmaier et al., 2010]†	878	30

Appendix B

Statistical Combination of Source Activity Measurements

Simple geometry counting stacks have been used at NIST to calibrate α sources for a number of years. In the Alpha-Gamma experiment, it was decided to measure the absolute activity of 49Si-3-3 with two spacer heights to give increased confidence in the metrology used to determine the stack solid angles.

B.1 Determining Source Activity for Each Stack

The SCA window for the ^{239}Pu α spectrum is seen in figure B.1. The window is placed around a flat region of the spectrum that corresponds to α particles that have undergone Rutherford backscattering off the Si substrate. The upper level is used to determine the signal rate, and the difference between the lower and upper level is used to assess the Rutherford backscattering background.

Let ϕ_L, ϕ_U, and ϕ_P be the channel numbers of the lower SCA level, the upper SCA level, and alpha peak, respectively. The number of Rutherford backscattered

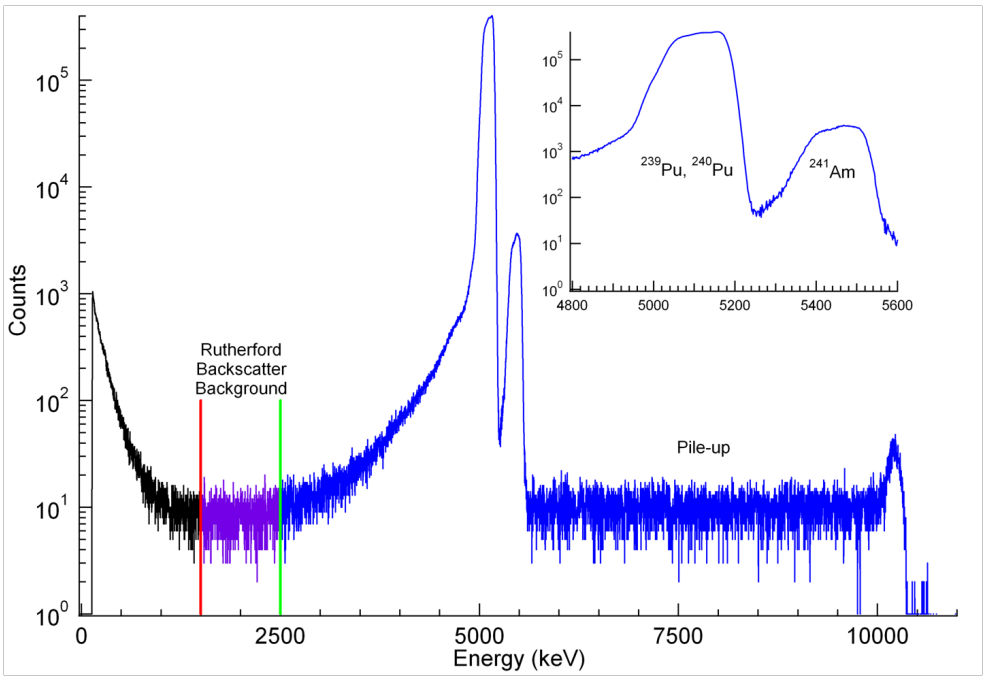


Figure B.1: SCA window for the charged particle spectrum from the ^{239}Pu source.

alphas in the alpha peak (C_{Ruth}) is:

$$C_{Ruth} = \left(\frac{\phi_P - \phi_U}{\phi_U - \phi_L}\right)(C_L^* - C_U^*) \tag{B.1}$$

giving us the corrected alpha count (X):

$$X = C_U^* - C_{Ruth} \tag{B.2}$$

The uncorrelated errors (δX_{unc}) associated with X are statistical (δX_{stat}) and stacking uncertainty in the solid angle ($\delta\Omega_{stack}$):

$$\delta X_{unc} = X\sqrt{\left(\frac{\delta X_{stat}}{X}\right)^2 + \left(\frac{\delta\Omega_{stack}}{\Omega}\right)^2} \tag{B.3}$$

This leads to the 4π alpha rate:

$$R^{4\pi} = \frac{X}{T \cdot \Omega} \tag{B.4}$$

and the uncorrelated error in the 4π alpha rate:

$$\delta R^{4\pi}_{unc} = \frac{\delta X_{unc}}{T \cdot \Omega} \tag{B.5}$$

B.2 Combining $R^{4\pi}_{38}$ and $R^{4\pi}_{76}$

Figures B.2 and B.3 show the activity measurements from the two configurations. Only statistical uncertainties are shown. A weighted constant fit to this data gives $R^{4\pi}_{38} = 23543.9(17)$ and $R^{4\pi}_{76} = 23545.6(17)$. Uncorrelated solid angle uncertainties from the stack heights are added in quadrature to give us $R^{4\pi}_{38} = 23543.9(84)$ and $R^{4\pi}_{76} = 23545.6(52)$ To combine the two 4π rates, a weighted average is performed:

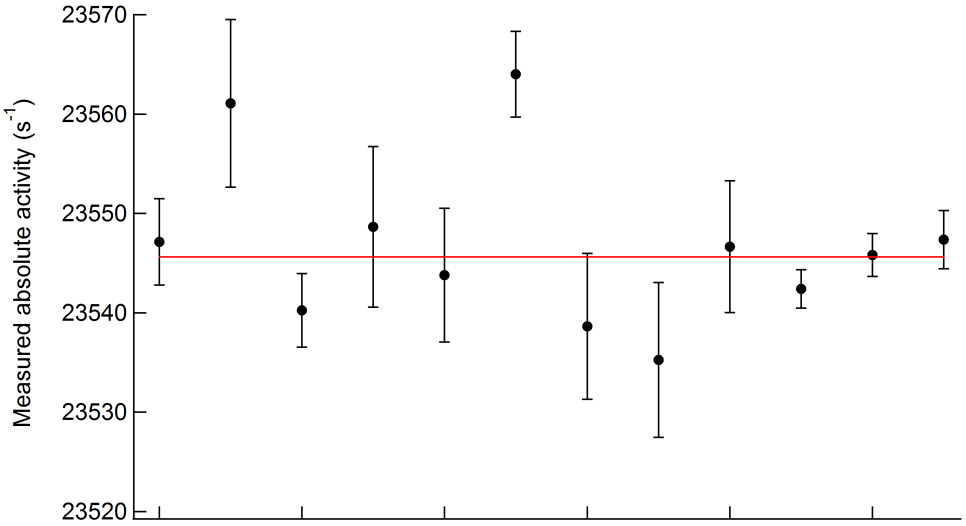


Figure B.2: Activity of 49Si-3-3 measured with the 76mm stack.

$$R^{4\pi}_{\alpha} = \frac{\left(\frac{R^{4\pi}_{76}}{\left(\delta R^{4\pi}_{76-unc}\right)^2} + \frac{R^{4\pi}_{38}}{\left(\delta R^{4\pi}_{38-unc}\right)^2}\right)}{\left(\frac{1}{\left(\delta R^{4\pi}_{76-unc}\right)^2} + \frac{1}{\left(\delta R^{4\pi}_{38-unc}\right)^2}\right)} \tag{B.6}$$

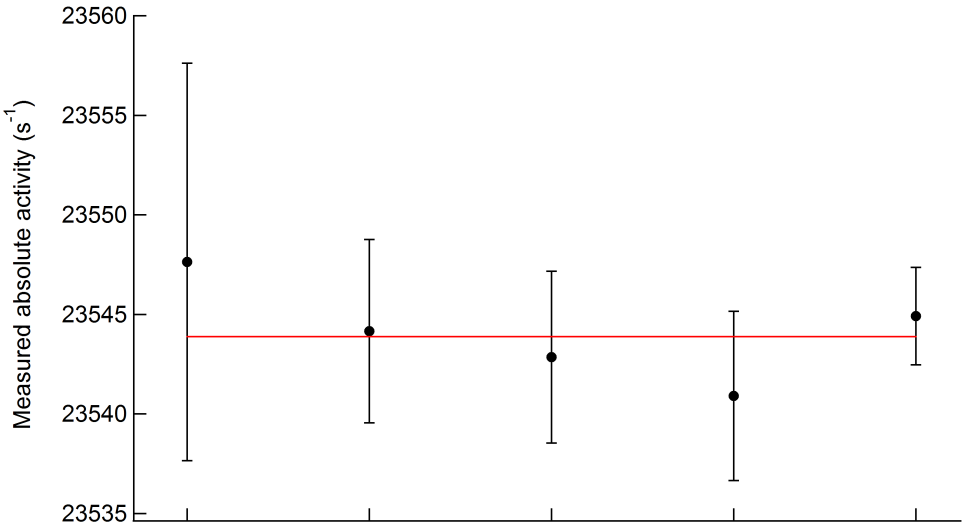


Figure B.3: Activity of 49Si-3-3 measured with the 38mm stack.

and the uncorrelated error is calculated:

$$\delta R^{4\pi}_{\alpha-unc} = \left(\frac{1}{\left(\delta R^{4\pi}_{76-unc}\right)^2} + \frac{1}{\left(\delta R^{4\pi}_{38-unc}\right)^2} \right)^{-\frac{1}{2}} \tag{B.7}$$

The correlated aperture error of 2.3×10^{-5} is then added in quadrature to the uncorrelated error, giving us the total error:

$$\delta R^{4\pi}_{\alpha} = R^{4\pi}_{\alpha} \sqrt{\left(\frac{\delta R^{4\pi}_{\alpha-unc}}{R^{4\pi}_{\alpha}} \right)^2 + \left(\frac{\Omega_{ap}}{\Omega} \right)^2} \tag{B.8}$$

and a final result of $R^{4\pi}_{Pu} = 23545.2(70)$. Absolute activity measurements of this source have been performed at NIST since 1992. These results can be compared directly to our result after correction for activity loss due to the half-life of ^{239}Pu. The measurements and a weighted constant fit are shown in figure B.4. Our result is approximately 0.03 % lower than the average of the old measurements. Still, this level of agreement over such a long period suggests that the source is very stable.

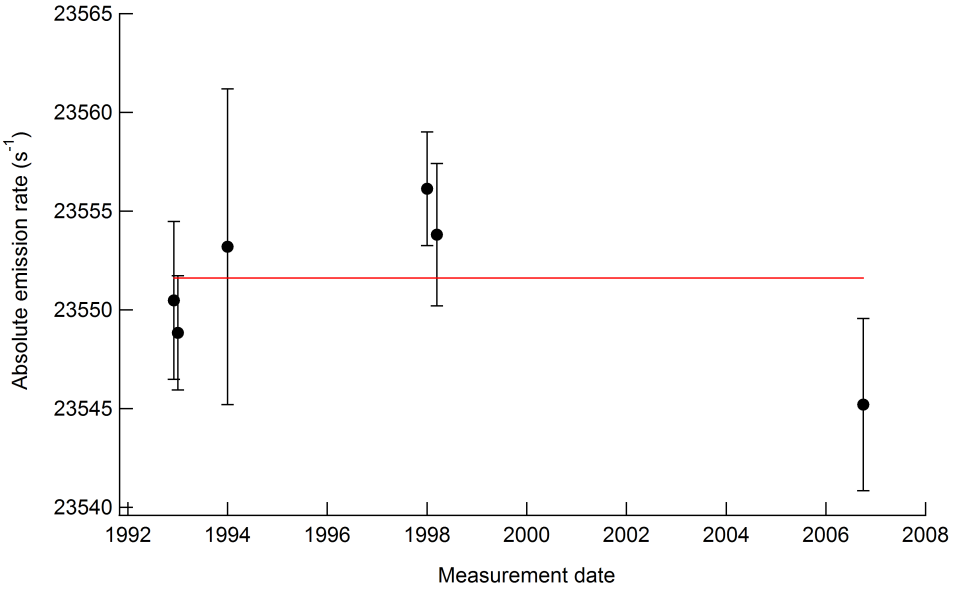


Figure B.4: Measurements of the activity of 49Si-3-3 from 1992 to 2006.

Vita

Andrew Tsung-Tse Yue was born in Cleveland, Ohio on October 18, 1982. He graduated from Brecksville-Broadview Heights High School in 2000. He enrolled at Hamilton College that fall and graduated in 2004 with a Bachelor of Arts in physics and mathematics. He enrolled at the University of Tennessee at Knoxville in the fall of 2004 and defended his thesis on August 4, 2011. He will graduate with his Ph. D. in physics in December 2011.